National Centre for Nuclear Research

Doctoral Thesis

Optimization and transient scenarios of the liquid eutectic metal fuel Dual Fluid Reactor

Tomasz Hanusek

A thesis submitted in fulfilment of the requirements
for the degree of Doctor of Physical Sciences
in the National Centre for Nuclear Research

Supervisor:
Prof. Dr. Rafael Macián-Juan
Auxiliary supervisor:
Dr. Zuzanna Marcinkowska

Acknowledgements

I want to thank my supervisor, Professor Rafael Macian-Juan, for his help during my PhD and his freedom with research work. Furthermore, I want to thank my auxiliary supervisor - Dr Zuzanna Marcinkowska, for the smooth collaboration, valuable comments and hints regarding my thesis.

I want to thank Prof. Mariusz Dąbrowski and Dr. Karol Kowal for running the "PhD4gen" project. It created an opportunity to prepare this thesis and to meet many valuable people on my path.

I want to thank Dr. Michał Spirzewski for the fruitful collaboration on different projects. Experience from these projects often inspired some parts of my thesis.

I want to thank all UZ3 people, which were kind and helpful in many areas.

I want to thank CIŚ cluster workers, especially Tobiasz Jarosiewicz, who was always willing to help with Serpent on the cluster.

I want to thank my whole family, especially my parents, for all their goodness, help, and the way they brought me up.

I want to thank my beloved wife - Zosia, for all the love, inspiration, motivation and faith in me.

Content

Figures list

Tables list

List of symbols

Letter	Definition
A	area
C	Delayed neutrons precursors concentration
h	Timestep size or heat transfer coefficient
k	Multiplication factor
n	Neutron density
t	Time

Letter	Definition
α	Temperature reactivity coefficient
β	Delayed neutron fraction
ρ	Reactivity
Λ	Mean Generation Time
λ	Decay constant
τ_c	Core transit time
τ_l	External primary loop transit time

Abstract

The Dual Fluid Reactor (DFR) is one of the many new circulating, liquid-fuel nuclear reactor concepts. It is a combination, a hybrid reactor between Molten Salt Reactor and Lead-cooled Fast Reactor. Compared to most Molten Salt Reactor projects, what is unique about the Dual Fluid Reactor is the reactor which also serves as a heat exchanger.

The Dual Fluid Reactor consists of 2 loops: fuel loop and coolant loop. Two options are proposed as fuel: uranium-chromium eutectic or uranium chloride salt - Cl_3. Therefore, two types of the Dual Fluid Reactor can be distinguished: metallic and salt. Type indicates what kind of fuel is used. Much research has been done on the salt version of the Dual Fluid Reactor. On the contrary, the metallic version is not well determined. In this thesis, only the metallic version is considered to fulfil the lack of this data.

However, performing computer simulations without validation or benchmark can be subject to considerable error. Therefore, it has been decided to model the Molten Salt Reactor Experiment (MSRE) first. It was one of the few ever working molten salt reactors. Moreover, it is very well documented.

It has been decided to use Serpent2 and TRACE codes to model the Molten Salt Reactor Experiment and Dual Fluid Reactor. However, the TRACE code is dedicated mainly to light-water reactors. Therefore, the TRACE code's source version has been modified to simulate MSRE fluids. Several transient scenarios for the MSRE have been performed in good agreement with the data from the Oak Ridge National Laboratory - institute, where the MSRE has been built and working for several years.

As for MSRE, the TRACE code has also been modified for DFR.

Then, several different calculations have been performed for the Dual Fluid Reactor: burnup calculations, proposed modified geometry and fuel composition to flatten the k_{∞}, introduction of control rods in the reflector zone, feeding the reactor during operation to avoid a subcritical state for the reactor, temperature reactivity coefficients calculations, coupling Serpent and TRACE to get a temperature and power distribution for steady-state conditions, proposed geometry for coolant and fuel loop, introduced several criteria to choose optimal working conditions and finally calculated several different transient scenarios.

Streszczenie

Reaktor dwupłynowy (DFR) jest jednym z wielu nowych koncepcji reaktora jądrowego, opartego na płynnym, krążącym w pętli paliwie. Reaktor jest kombinacją, hybrydą, reaktora opartego na stopionych solach (Molten Salt Reactor) oraz reaktora prędkiego chłodzonego ołowiem (Lead-cooled Fast Reactor). Co jest unikalne w koncepcji DFR, to fakt, że reaktor pełni także rolę wymiennika ciepła.

Reaktor dwupłynowy składa się z 2 pętli: paliwowej oraz pętli z chłodziwem. Jako paliwo proponowane są 2 opcje: eutektyk uran-chrom lub chlorek uranu - UCl_3. Zatem, dwie opcje reaktora dwupłynowego mogą zostać wyszczególnione: opcja metaliczna i opcja na stopionych solach. Dana opcje określa rodzaj zastosowanego paliwa. Wersja na stopionych solach została przebadana pod wieloma aspektami.. Z drugiej strony, reaktor z paliwem metalicznym, nie został przeanalizowany pod wieloma aspektami. Z tego powodu zdecydowano, aby w niniejszej pracy skupić się ściśle na metalicznej wersji DFR.

Jednakże symulacje komputerowe wykonywane bez żadnego rodzaju walidacji lub porównania z innymi symulacjami mogą być obarczone znacznymi błędami. Z tego powodu, zdecydowano, aby najpierw zamodelować eksperymentalny reaktor na stopionych solach (Molten Salt Reactor Experiment - MSRE). Był to jeden z niewielu kiedykolwiek działających reaktorów na stopionych solach. Ponadto, działanie tego reaktora jest bardzo dobrze udokumentowane.

Do zamodelowania MSRE, a później DFR zdecydowano się użyć kodu Serpent2 oraz kodu TRACE. Jednakże, kod TRACE jest dedykowany głównie dla reaktorów lekkowodnych. Z tego powodu, wersja źródłowa kodu TRACE została zmodyfikowana tak aby kod mógł pracować na solach użytych w MSRE. Kilka stanów przejściowych zostało wykonanych, a otrzymane wyniki dobrze pokrywały się z danymi zawartymi w raportach *Oak Ridge National Laboratory* - instytucie, w którym MSRE został zbudowany i działał przez kilka lat.

Podobnie jak dla MSRE, dla DFR także dokonano modyfikacji kodu TRACE. Następnie wykonano szereg następujących analiz: obliczenia wypaleniowe, modyfikacja geometrii oraz składu paliwa w celu spłaszczenia współczynnika mnożenia neutronów, zaproponowanie prętów sterujących w obszarze reflektora, dodawanie paliwa podczas pracy reaktora w celu uniknięcia podkrytyczności, obliczenie współczynników temperaturowych, sprzężenie kodu Serpent2 z kodem TRACE w celu otrzymania rozkładu mocy oraz temperatury w stanie ustalonym, zaproponowano geometrię dla pętli paliwowej oraz pętli chłodzącej, zaproponowano kilka kryteriów

dzięki którym wybrano optymalne parametry pracy układu, oraz dokonano obliczeń stanów przejściowych dla kilku różnych przypadków.

Chapter 1 Introduction

In this chapter, the importance of energy production from reliable and low-emission sources will be established. Molten salt reactor technology development will be presented in more detail from several proposed energy sources.

1.1 Energy production

In this section, energy production importance and different energy sources are presented.

1.1.1 Differences in energy consumption per capita

One of the most critical indicators of civilization development is energy consumption. Energy is crucial for many human needs, like transportation, construction, electricity, heat demands, etc. Fig. 1 presents the relationship between the Human Development Index (HDI) and primary energy consumption. The figure was created based on data from [1], [2]. It can be seen that high HDI is positively correlated with higher energy consumption. In all countries with a high HDI; above 0.9, energy consumption per capita is greater than 25 MWh per year. Therefore, high energy consumption is necessary for the country's increased development, but it is not sufficient. For example, Turkmenistan or Kuwait citizens consume significantly more energy than Italy or Ireland, but their HDI is still not as high as those mentioned European countries.

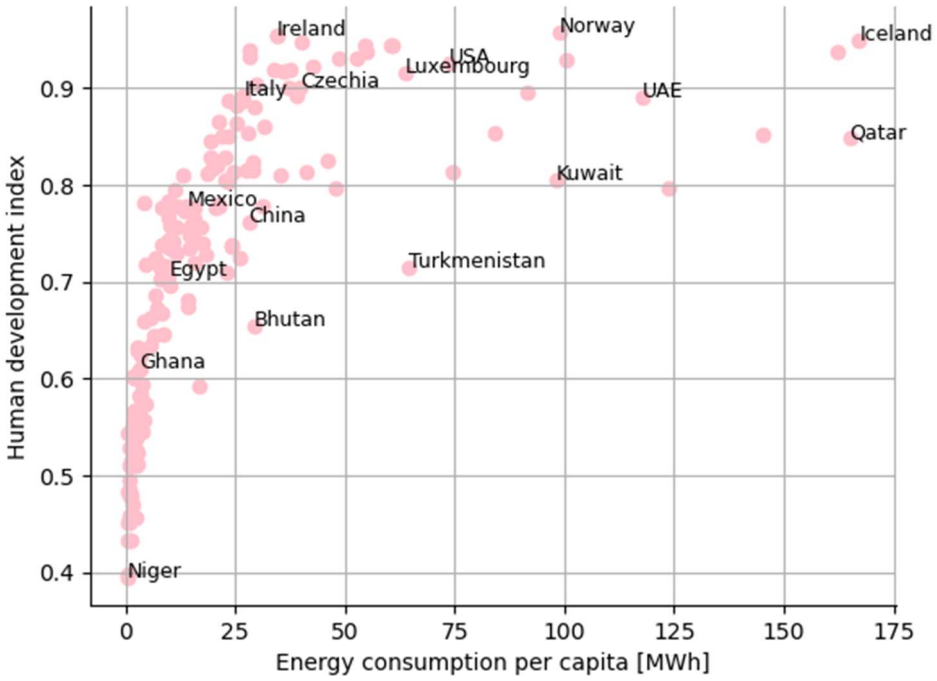

Fig. 1 Human index development in the function of energy consumption for 2019

There are many countries which are developing fast; therefore, their energy consumption will increase in the near future.

1.1.2 CO_2 issue and mortality by different energy sources

On the other hand, the primary energy source significantly impacts greenhouse gases, thus, global warming. In Fig. 2, CO_2 concentration and average global surface temperature are presented. The strong correlation between those two quantities is visible. Therefore, the primary energy source should be a worldwide high-priority issue to avoid increasing global temperature. Furthermore, different energy sources have other greenhouse emissions and different mortality rates. In Fig. 3, mortality rates for various electricity sources can be seen. In Fig. 4, equivalent CO_2 emission by different energy sources is presented.

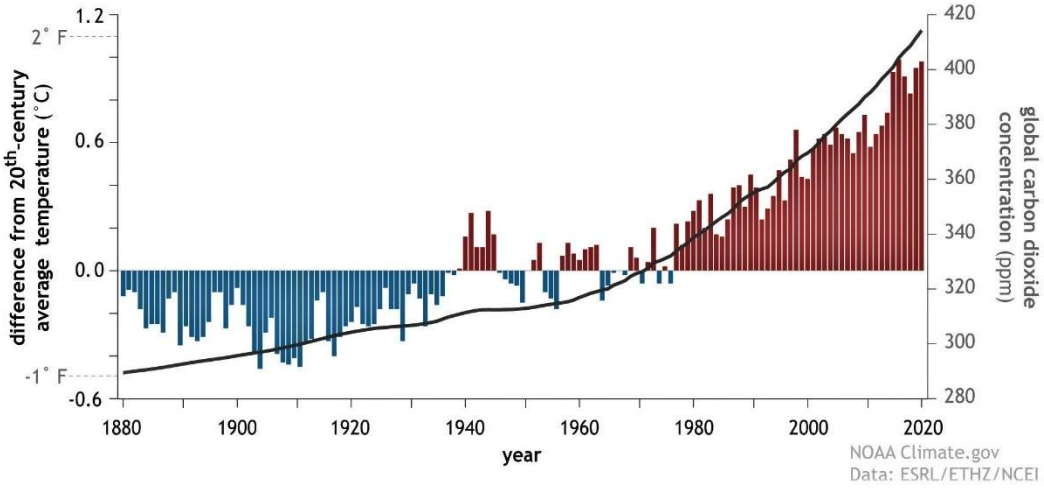

Fig. 2 Global atmospheric carbon dioxide concentration and surface temperature [3]

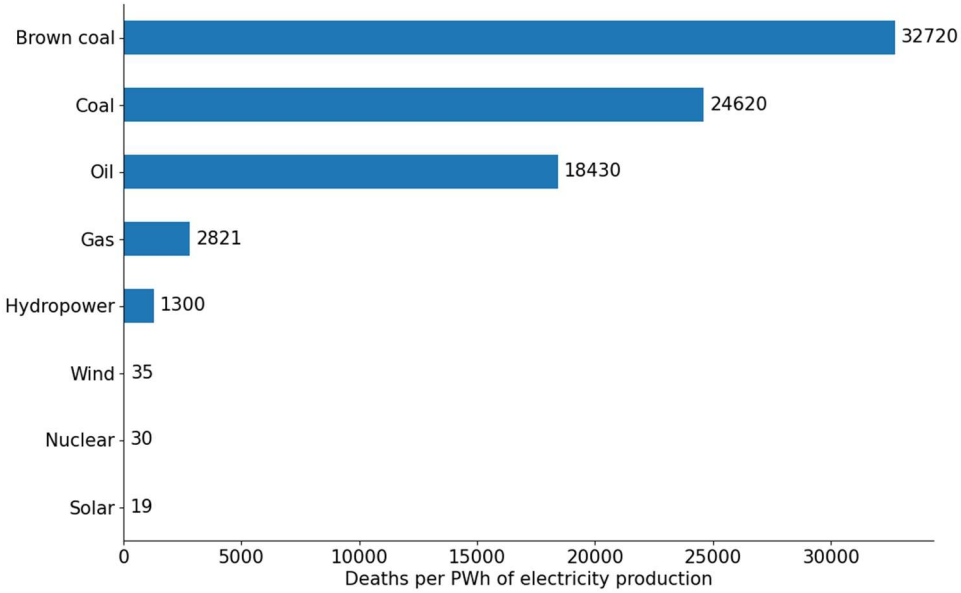

Fig. 3 Deaths per PWh for different electricity sources based on data from [3], [4]

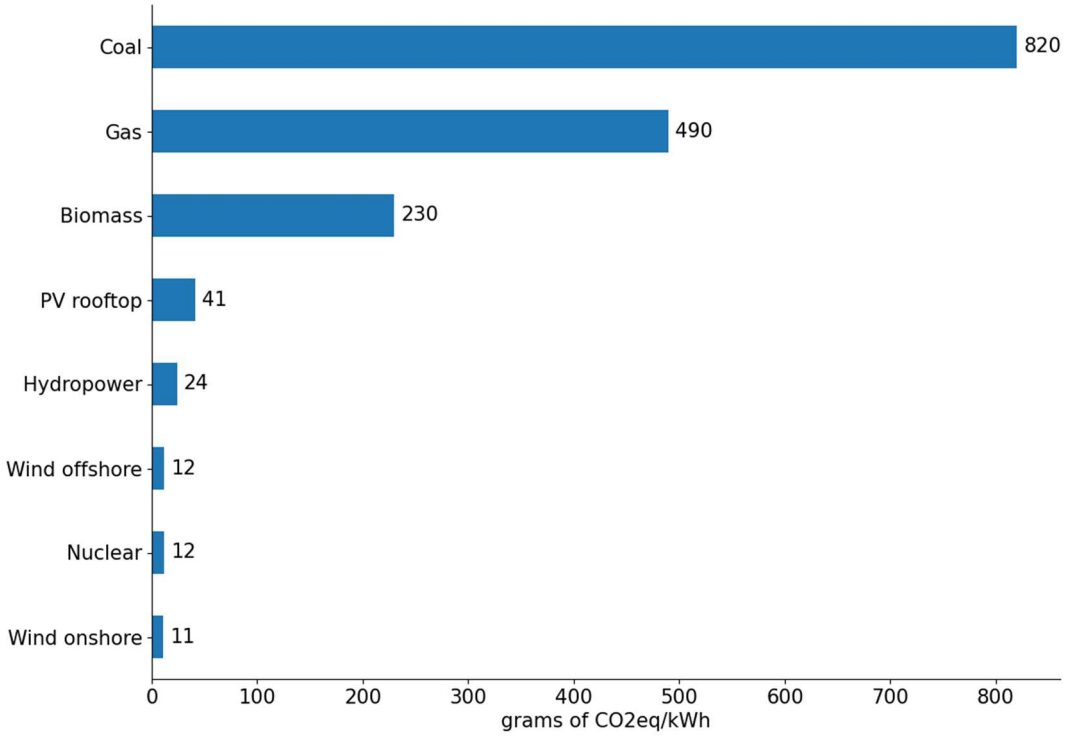

Fig. 4 Equivalent CO_2 emission by different energy sources [5]

Based on Fig. 3 and Fig. 4, it can be seen that the best energy sources from the point of view of mortality and greenhouse emission are: hydro, nuclear, PV and wind.

1.1.3 Generation IV reactors

From those energy sources, only hydro and nuclear can be treated as reliable. There is no reasonably cheap and proven energy storage technology for the industrial scale. Thus, reliable energy sources must produce a significant amount of energy. The only energy source mentioned above as reliable and low CO_2 emitters, which can directly produce heat, is nuclear energy. Heat is crucial for industrial applications (high-temperature heat) and district heating (low-temperature heat). Currently, heat for the industry is produced mainly by coal and gas. Therefore, there is a strong need to develop high-temperature nuclear reactors, especially for industrial applications.

GIF (Gen IV International Forum) proposed six technologies of nuclear reactors from IV generation as the most promising in terms of safety, economy, waste and non-proliferation [6]. All of the GIF reactors listed below are high-temperature reactors.

Those technologies are:

- GFR - Gas-cooled Fast reactor
- LFR - Lead-cooled Fast Reactor
- MSR - Molten Salt Reactor
- SCWR - Supercritical Water-cooled Reactor
- SFR - Sodium-cooled Fast Reactor
- VHTR - Very High-Temperature Reactor

Several years ago, a new nuclear reactor concept was established by a group of scientists associated with the Institute for Solid-State Nuclear Physics in Berlin. The name of the concept is DFR (Dual Fluid Reactor), and it can be treated as a kind of version of MSR. More information about molten salt reactors will be presented in the next sections.

Based on definition provided by IAEA (International Atomic Energy Agency), Molten Salt Reactor is any reactor in which molten salt has a substantial role in the reactor core (fuel, coolant, moderator) [7].

1.2 Historical MSR concepts

In this chapter, a short characterization of several MSRs has been established, in particular, two reactors which are well documented: Aircraft Reactor Experiment and Molten Salt Reactor Experiment.

1.2.1 Aircraft Reactor Experiment

The first MSR was critical in 1954. The reactor has been named: Aircraft Reactor Experiment (ARE) and is meant to be the aircraft's propulsion. The main parameters of the reactor can be found in Table 1 [8].

Table 1 Aircraft Reactor Experiment - main features. [8]

Quantity	Value	Unit
Power	2.5	MW
Neutron spectrum	Thermal	
Moderator	BeO	
Reflector	BeO	
Fuel composition	53.09% of NaF 40.73 % of ZrF_4 6.18 % of UF_4	mole
Coolant	Na-K	
Reflector coolant	Sodium	
Material structure	Inconel	
Uranium enrichment	93.4	%
Design lifetime	1500	hour
Total operation	100	MWh
Max. fuel temperature	1144	K
Max. coolant temperature	1089	K

The axial cross-section of the reactor is presented in Fig. 5.

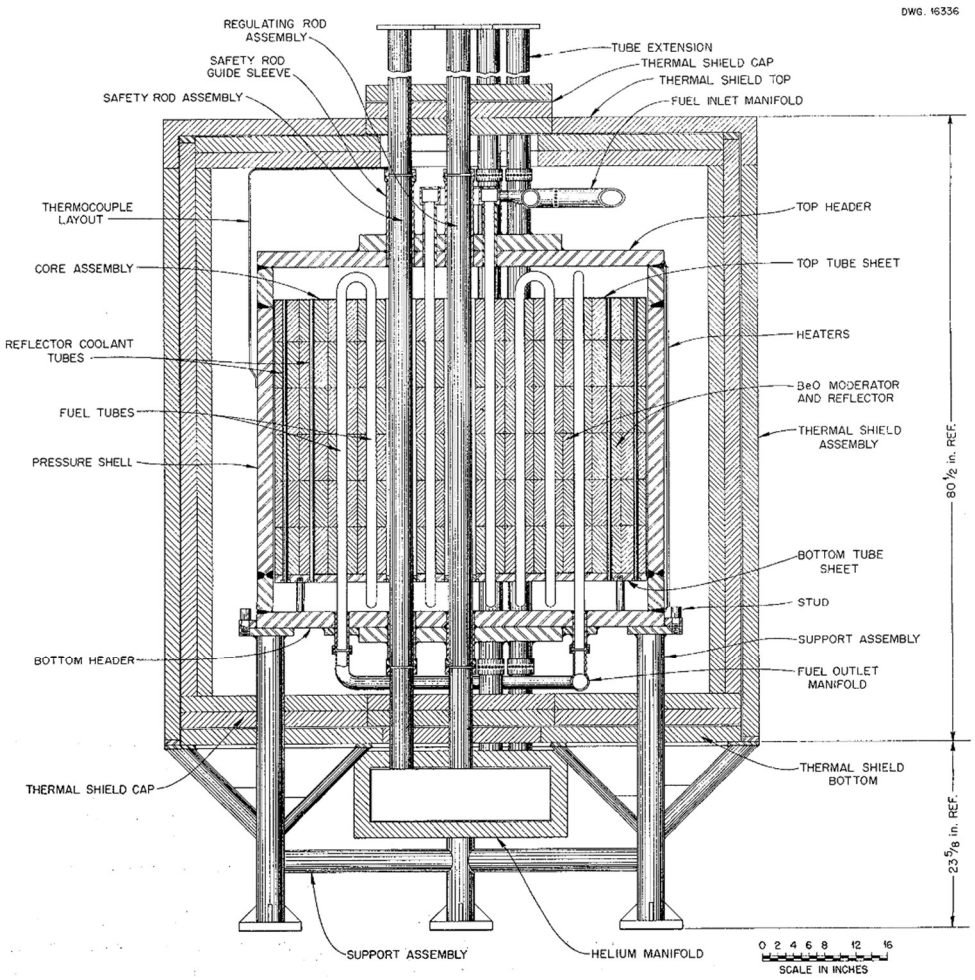

Fig. 5 Aircraft Reactor Experiment - axial cross-section [8]

ARE was the first ever built circulating, molten salt, liquid fuel nuclear reactor. Therefore, it was proof of the concept regarding fuel circulation and proposed many solutions for liquid fuel reactors, particularly molten salt reactors. For example, systems such as:

- Fuel tanks storage - to store fuel in subcritical tanks when the reactor was not working
- Coolant tanks storage - to store coolant in tanks when the reactor is not working
- Liquid fuel and coolant pumps - to force the flow of liquid fuel and liquid metal as coolant
- Off-gas system to extract fission gases from the fuel
- Fuel enrichment system to feed the reactor online during operation
- Heating system - which allows heats-up of all fuel and coolant loops elements to a specific temperature above the solidification point.

Many other systems specific to liquid fuel reactors have been established. But, except for those, the facility was equipped with many standard systems as every other nuclear reactor.

After conducting the Aircraft Reactor Experiment with satisfactory results, work on a higher-power reactor has started. Oak Ridge National Laboratory began to work on Aircraft Reactor Test. It was intended to be a 60 MW reactor with the same materials used for ARE but with modified geometry. However, the reactor never became critical, and further work was suspended in September 1957 [9].

Nevertheless, ORNL continued work on liquid fuel reactors, which resulted in constructing the Molten Salt Reactor Experiment, described in the next section.

1.2.2 Molten Salt Reactor Experiment

The Molten Salt Reactor Experiment (MSRE) is molten salt, liquid fuel nuclear reactor. It is also much better documented than ARE facility. The scheme of the main components of the MSRE is presented in Fig. 6 [10].

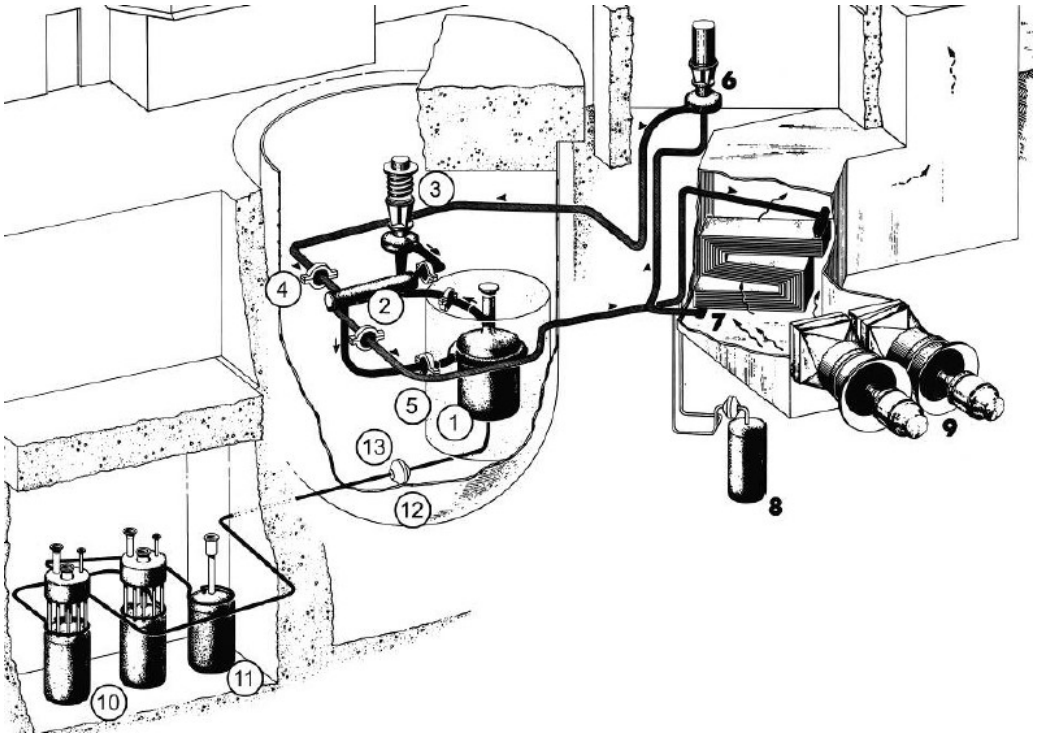

Fig. 6 Schematic of the MSRE main components [10]

The following numbers in Fig. 6, correspond to specific elements:

1 - reactor vessel, 2 - heat exchanger, 3 - fuel pump, 4 - freeze flange, 5, thermal shield, 6 - coolant pump, 7 - radiator, 8 - coolant drain tank,

9 - fans, 10 - fuel drain tanks, 11 - flush tank, 12 - containment vessel, 13 - freeze valve.

The main characteristic of the MSRE has been presented in Table 2.

Table 2 MSRE - main features.

Quantity	Value	Unit
Designed power [11]	10	MW
Nominal power [10]	7.4	MW
Moderator [11]	graphite	
Fuel salt [12]	LiF-BeF_2-ZrF_4-UF_4	
Coolant salt [12]	LiF-BeF_2	
Material structure [11]	INOR-8	
Heat exchanger type [11]	Shell-type	
Total operation [13]	549	EFPD
Max. fuel temperature [11]	936	K
Max. coolant temperature [11]	866	K

MSRE consists of 2 loops: fuel loop and coolant loop. Cooled fuel (about 908 K) goes from the heat exchanger to the reactor flow distribution part. It can be seen in Fig. 7. Then, fuel salt goes through the downcomer to the lower plenum. Here fuel is distributed into fuel channels. The reactor core consists of 1140 equivalent full-sized fuel channels. The detailed geometry of the fuel channel is established in Fig. 8. Fuel passing the reactor core is heated up to 936 K. Then, fuel goes to the upper plenum and the fuel outlet pipe. Finally, fuel salt goes to the primary pump and back to the heat exchanger.
In the heat exchanger, fuel is cooled down by coolant salt. Secondary salt is heated up from 825 K to about 866 K. Then, the coolant goes to the radiator, which is cooled by two massive fans. Cooled secondary salt is going to pump and re-enter the heat exchanger.
Radial reactor cross-section is presented in Fig. 9 [14]. In Fig. 9 graphite matrix and the fuel's channels can be seen. The reactor vessel was about 1.5 m in diameter and 2.4 m in height. Most of the reactor core volume was occupied by graphite: about 2 m^3, while fuel occupied about 0.57 m^3.

In the middle part of the reactor core, four circular channels were made. Three of them are placed by control rods, and one remaining is for material irradiation tests. In Fig. 10, the control rods and the material testing channel are presented in more detail.

Control rods were used during start-up, shutdown and power control operations. The material testing channel irradiated reactor structure materials samples: INOR-8, also called Hastelloy-N and graphite.

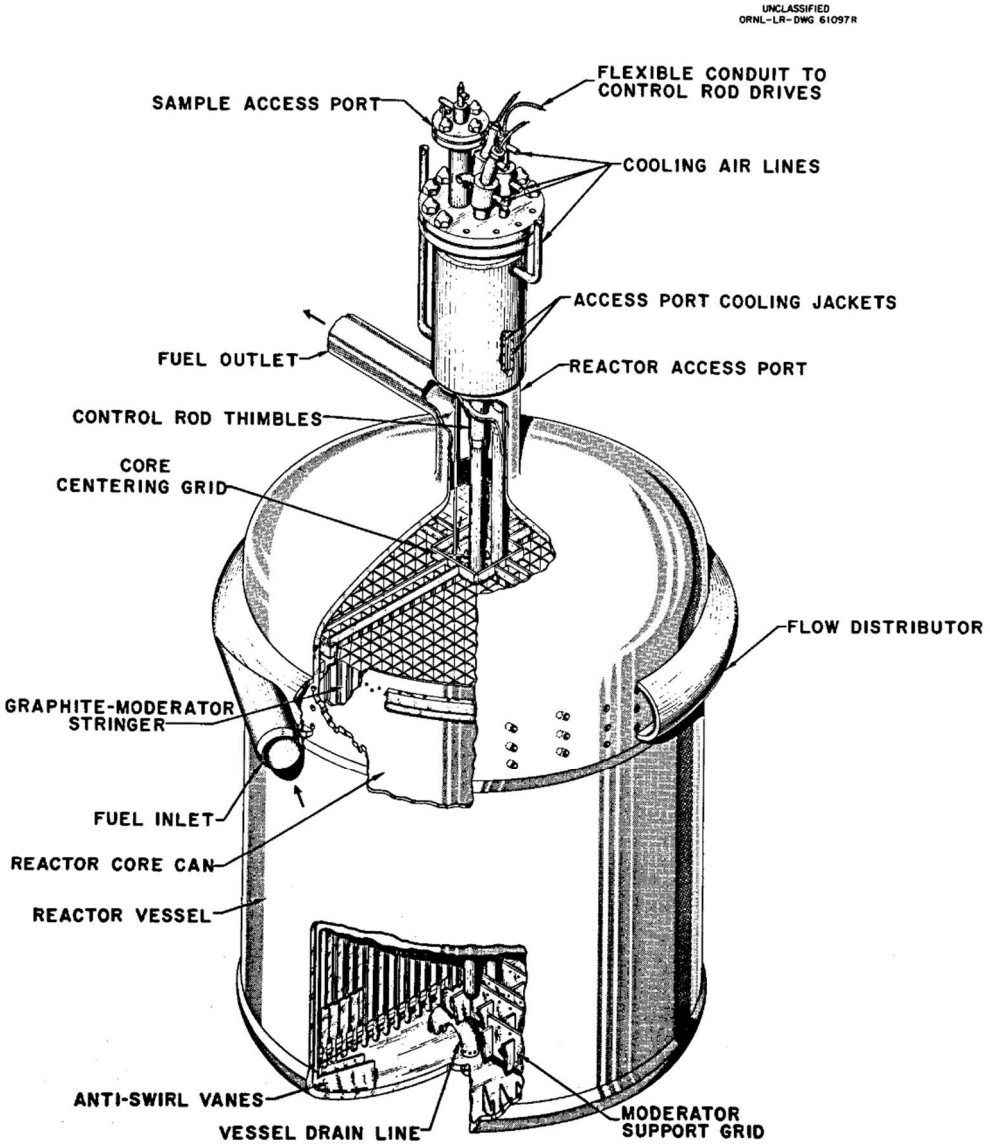

Fig. 7 MSRE schematic view [11]

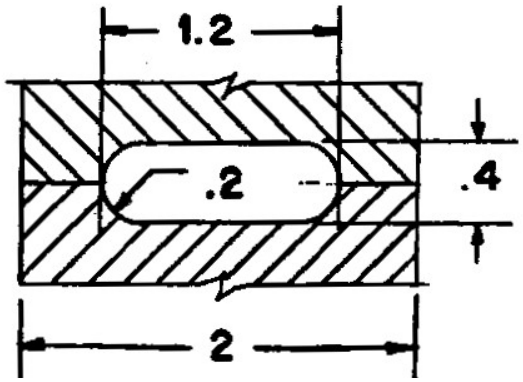

Fig. 8 Single fuel channel - dimensioned in inches [11]

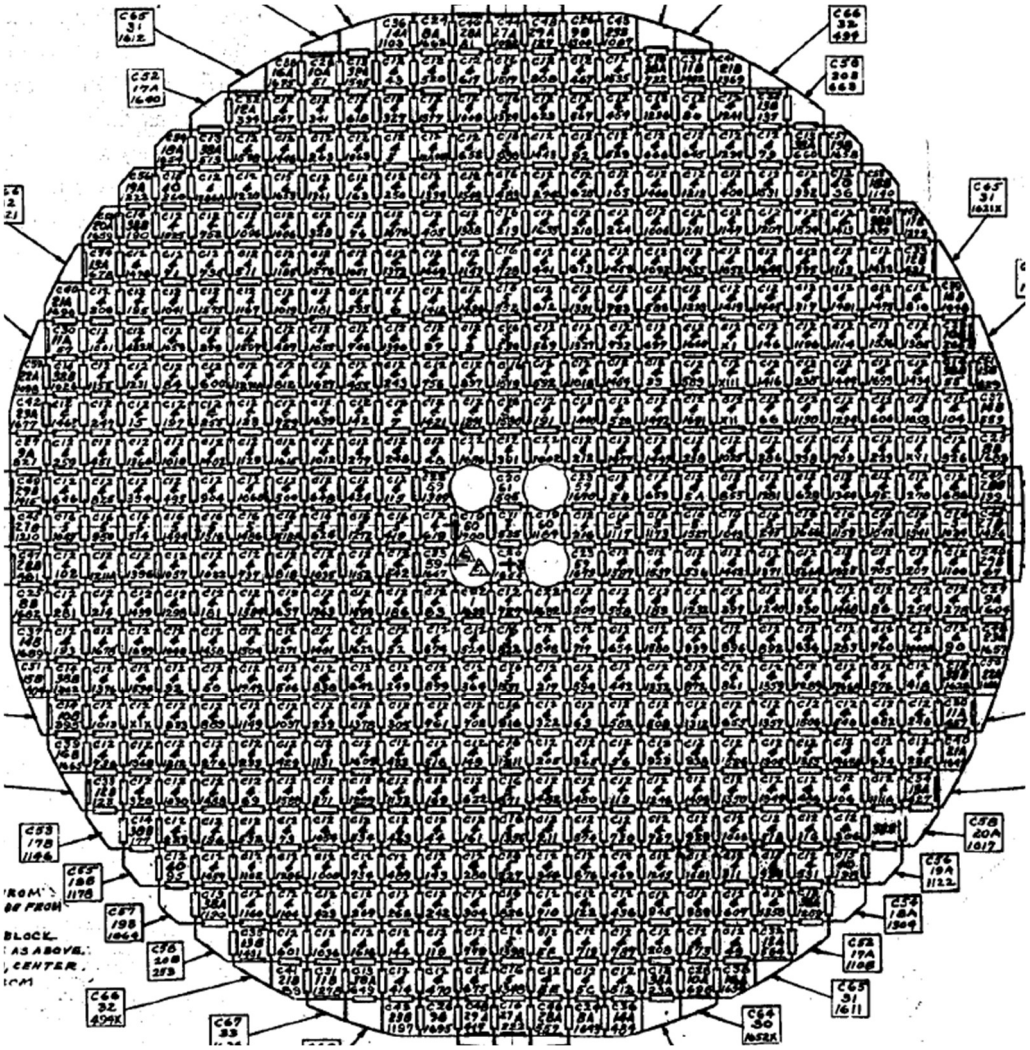

Fig. 9 MSRE - core radial cross-section [14]

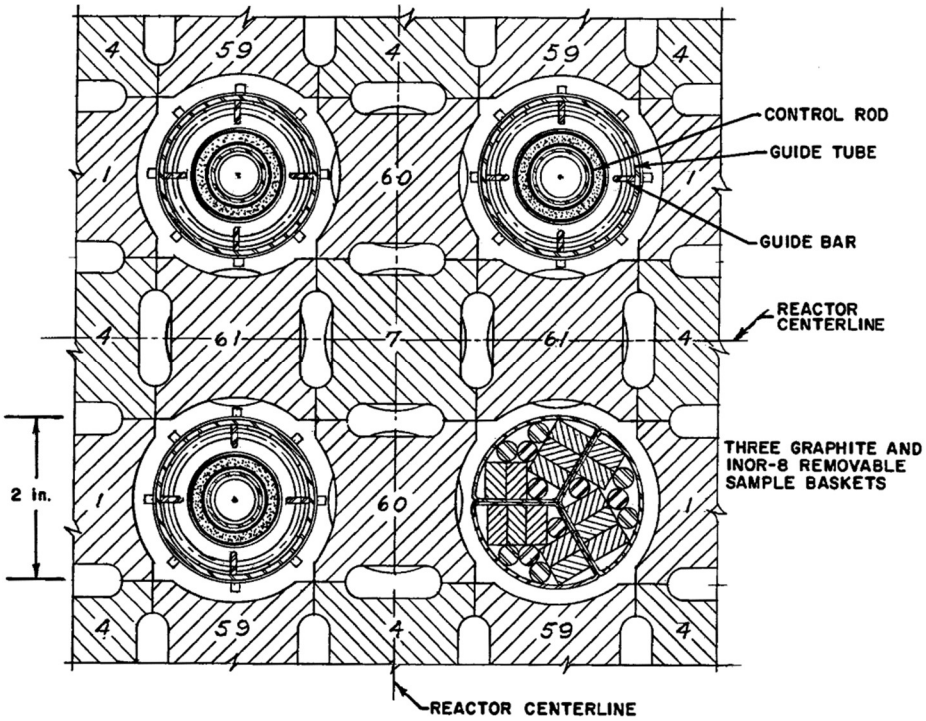

Fig. 10 MSRE - arrangement of the control rods [11]

Based on experience with ARE, the same fuel salt has been used in MSRE. On the contrary, Hastelloy-N - structure material used in MSRE was developed just for MSRE.
MSRE reactor was operated from 1965 - 1969. Science 1965 used U-235; in 1968, using U-233 as fuel, a criticality experiment was conducted. Therefore, it was the first nuclear reactor with U-233 fuel [13].

MSRE was shut down permanently in 1969. However, after a few years of experience and successful operation of the MSRE, post-examination work regarding materials behaviour was continued. Moreover, theoretical work was done on an industrial molten salt reactor called Molten Salt Breeder Reactor (MSBR).

1.2.3 Molten salt breeder reactor

The molten salt breeder reactor was intended to be a full-scale power reactor with an electrical output power of about 1000 MW and thermal reactor power of about 2300 MW. Fuel salt composition was as follows: ^{7}LiF-BeF_2-ThF_4-UF_4 with the corresponding mole fractions: 71.7, 16, 12 and 0.3. MSBR concept was scaled-up MSRE. It was intended to use the same moderator - graphite, and also the same structure material - Hastelloy-N [15].

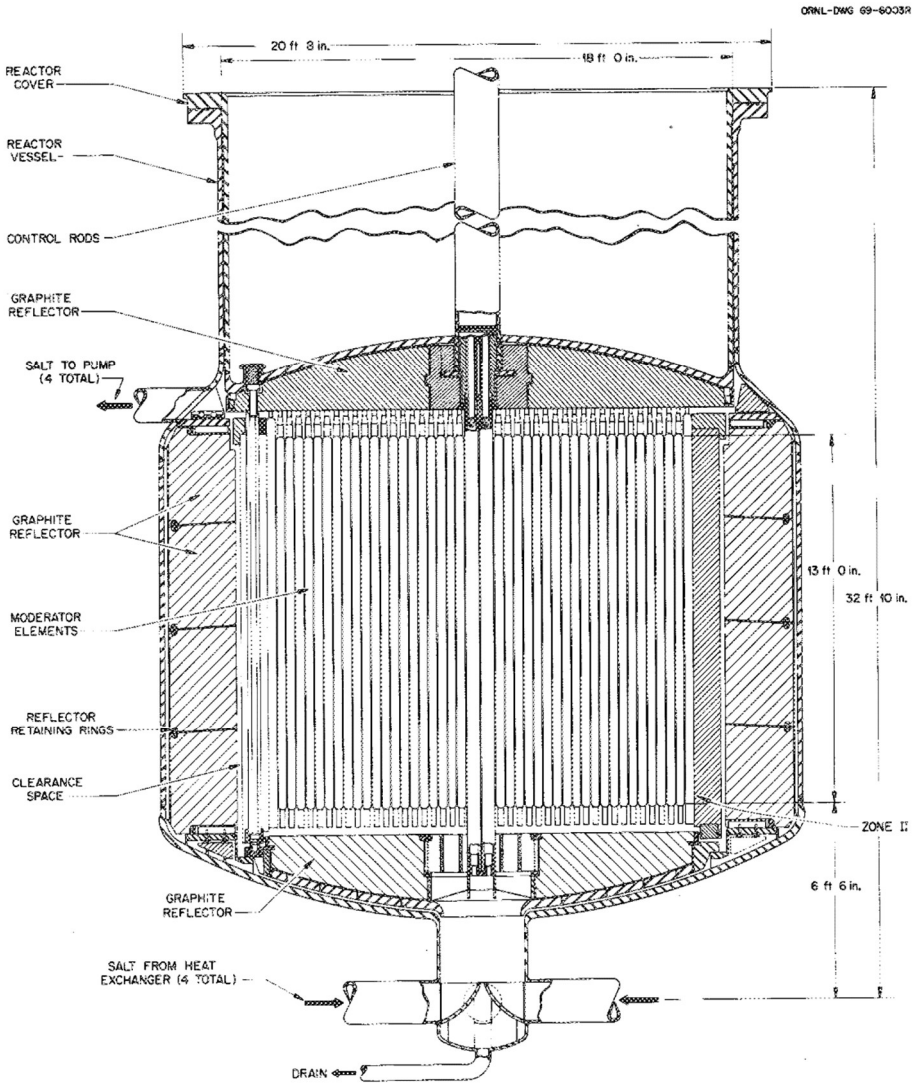

Fig. 11 MSBR - axial cross-section of the reactor vessel [15]

Nevertheless, based on the decision from 1973, due to financial reasons, the development of the molten salt technology in ORNL has been concluded [16].

1.2.4 Other conceptions

Molten salt technology was also developed in other countries, namely: the United Kingdom and the Soviet Union.

British project was developing in the 60s and beginning of the 70s. The idea was to build a 2500 MWe molten chloride salt-fast reactor [17].

The Soviet project was started in the second half of the 70s. Work was performed at the Kurchatov institute - the most significant nuclear institute in the Soviet Union.

Nevertheless, neither the British nor the Soviet project was ever concluded with the actual molten salt reactor.

After the mentioned projects, the development of molten salt technology stopped for some time. Finally, however, due to several reasons: including an increase in LWR safety requirements (thus costs), looking for safer reactor technologies, and looking for high-temperature reactors, molten salt reactor technology started to be more promising and interesting.

1.3 Recent MSR concepts

In this section, several nowadays molten salt projects have been established.

1.3.1 IMSR-400

This reactor Integral Molten Salt Reactor (IMSR) is a thermal spectrum graphite reactor based on fluoride salts. It is developed by a Canadian company: Terrestrial Energy. It has 400 MW of thermal power and 194 MW of electrical power. The design for this project is presented in Fig. 12. It can be seen that the reactor core, primary pumps and heat exchangers are closed into one barrel. Therefore, it can be considered as a small modular reactor [18].

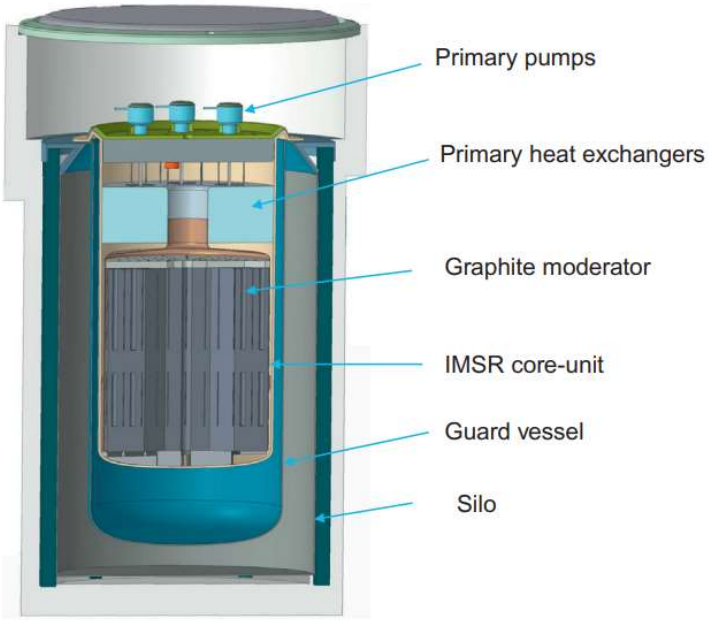

Fig. 12 IMSR with primary components [18]

1.3.2 MSFR

Molten Salt Fast Reactor (MSFR) is a French reactor concept run in the frame of the SAMOFAR project. As the name suggests, it is a fast neutron spectrum reactor with 3000 MW_{th} power. The reactor is pool-type. The initial fuel load can be U-235 or U-233, with at least 5% enrichment. Fuel salt is based on fluoride salt: LiF, with Li-7, enriched up to 99.995% due

to neutron economy reasons. Heat is extracted from the fuel salt by 16 heat exchangers, which are placed around the reactor [19].

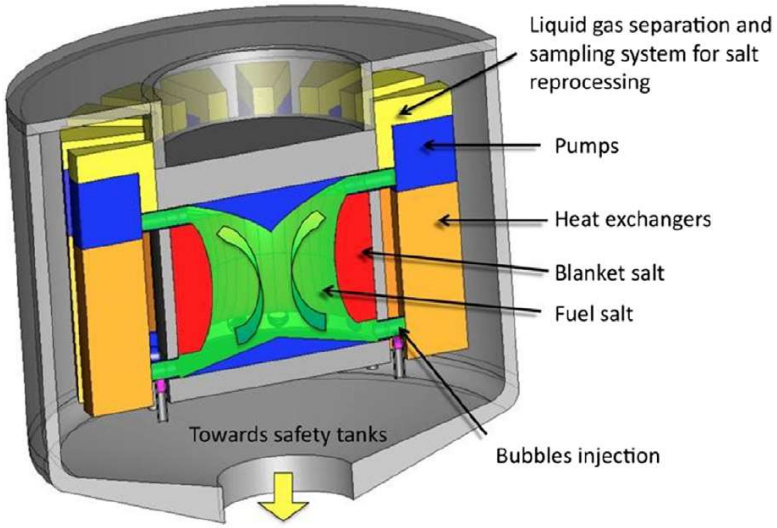

Fig. 13 MSFR concept design [19]

1.3.3 MSTW

Molten Salt Thermal Wasteburner (MSTW) is a thermal spectrum nuclear reactor based on a mixture of spent fuel and thorium salts. Graphite blocks play the role of the moderator. The single unit has 270 MW_{th} and 100 MW_e. Fuel is based on fluoride salts. The single unit lifetime is estimated to be seven years and should be exchanged for the new one. Plant lifetime is estimated to be 60 years [20]. MSTW conceptual design can be seen in Fig. 14.

Fig. 14 MSTW concept design [20]

1.3.4 TMSR-500

ThorCon Molten Salt Reactor (TMSR-500) is a thermal neutron spectrum, graphite project. It is led by ThorCon company. The power plant consists of 2 units, each 250 MW_e. Each unit needs to be replaced every four years. As the name suggests, the reactor is intended to work on the thorium cycle. Fuel composition is the same mixture as it has been used in MSRE in ORNL [21]. A single unit can be seen in Fig. 15.

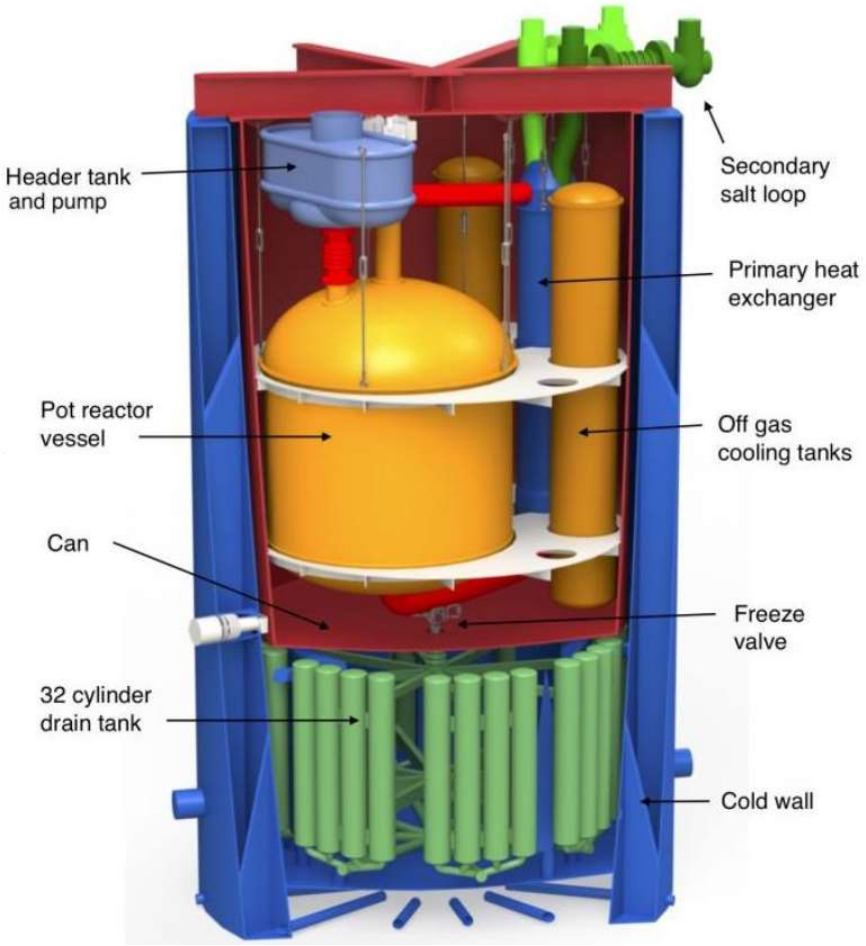

Fig. 15 TMSR-500 concept design [21]

1.3.5 MOSART

The MOlten Salt Actinide Recycler & Transmuter (MOSART) is a molten salt project currently running in Russia. The reactor has 2400MW_{th}. It is a fast neutron spectrum pool-type reactor. Fuel salt is based on fluoride. It is intended to run for 50 years. Lead is used here as a coolant. What can be interesting, in this fast reactor, graphite is used as a reflector [22].

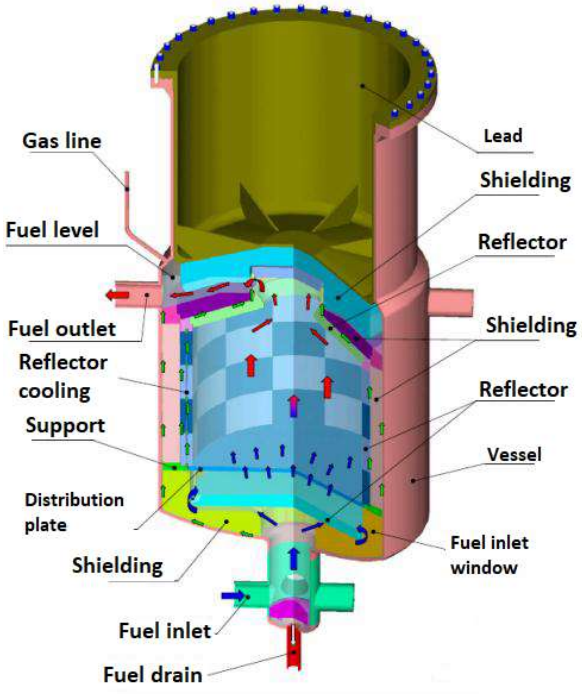

Fig. 16 MOSART concept design [22]

1.3.6 TAP

Transatomic Power reactor is a 1250 MW_{th} molten salt reactor. The concept was created in collaboration between ORNL and Transatomic Power Corporation (TAP). The reactor design is mainly based on the MSRE reactor. However, there are a few significant changes.
Firstly, TAP is intended to work on different fuel salt. Instead of LiF-BeF_2-ZrF_4-UF_4, LiF-UF_4 has been proposed. This choice's drawback is the higher melting point of the fuel salt (490^{0}C instead of 434^{0}C). Nevertheless, such change increase significantly uranium concentration in the reactor (from about 0.9% to over 27%), which is substantial from an economic point of view.
Secondly, in the TAP reactor, zirconium hydride is intended to be used instead of graphite as a moderator. From the neutronic point of view, neutron moderation is more efficient by zirconium hydride than graphite. It is because of the relatively small energy change due to neutron-graphite collision, compared with the neutron-hydrogen collision. What is even more interesting, part of the moderator rods is moveable. Therefore, it can allow changing the neutron spectrum during the reactor lifetime.

A schematic view of the reactor core can be seen in Fig. 17 [23].

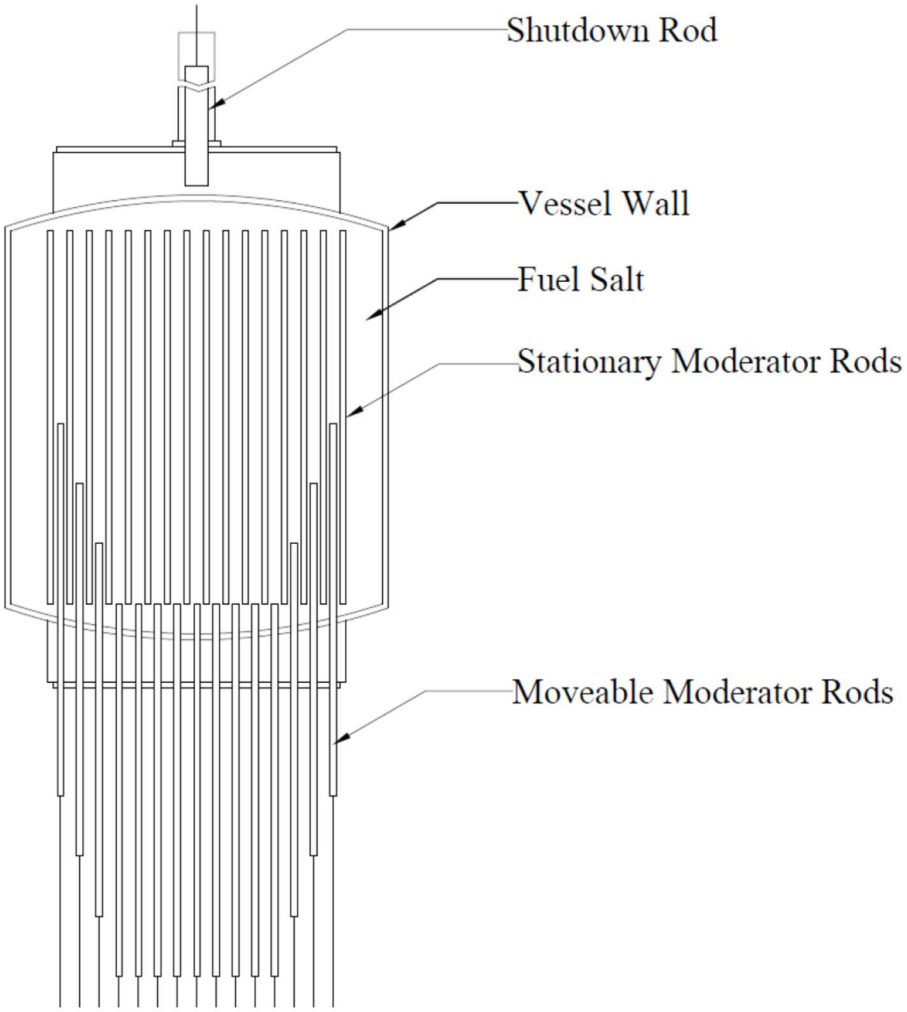

Fig. 17 TAP reactor design concept [23]

1.3.7 DFR

Dual Fluid Reactor (DFR) is another liquid, circulating fuel reactor concept [24], [25]. DFR consists of two loops: a fuel loop and a coolant loop. The DFR has two basic options for fuel: a molten salt or a metallic eutectic denoted as DFR_s and DFR_m, respectively. For the coolant, the most probable option is liquid lead or lead-bismuth eutectic.

What is unique in this reactor concept is that heat is taken from the fuel loop to the coolant in the reactor core. Therefore, the reactor also plays the role of the heat exchanger. The conceptual design for the dual fluid reactor can be seen in Fig. 18 [25]. Under the reactor core, a melting plug is installed. In case of a temperature rise, the plug will be melted, and the fuel will drain into subcritical tanks below the reactor.

The reactor is intended to have a pyroprocessing unit which will allow it to extract specific elements and feed the reactor during operations. The pyroprocessing unit can separate fission products with the highest decay

heat fractions and store them in dedicated storage, as shown in Fig. 18. Such a solution allows transporting the fuel to subcritical tanks without a cooling system for these tanks. One of the propositions for fuel pumping is magnetohydrodynamic pumps [26].

There are already many different research papers and theses regarding different types of fuel and power, for example, DFR_s with 3 GW_{th} [27], DFR_s with 100 MW_{th} [28], and DFR_m with 250 MW [29]. Currently, the development of DFR is mainly conducted in China, Germany, and Poland. Many different research studies have been done for the salt version of the DFR with different thermal power, 3000 MW [30], 500 MW [31], 100 MW [28], and 2 MW [32]. On the contrary, the proposed metallic version of the DFR still has many unknown areas. To fulfil part of them, this dissertation deals with the metallic eutectic version DFR_m with 250 MW_{th}, similar to the model presented in previous research [29], [33].

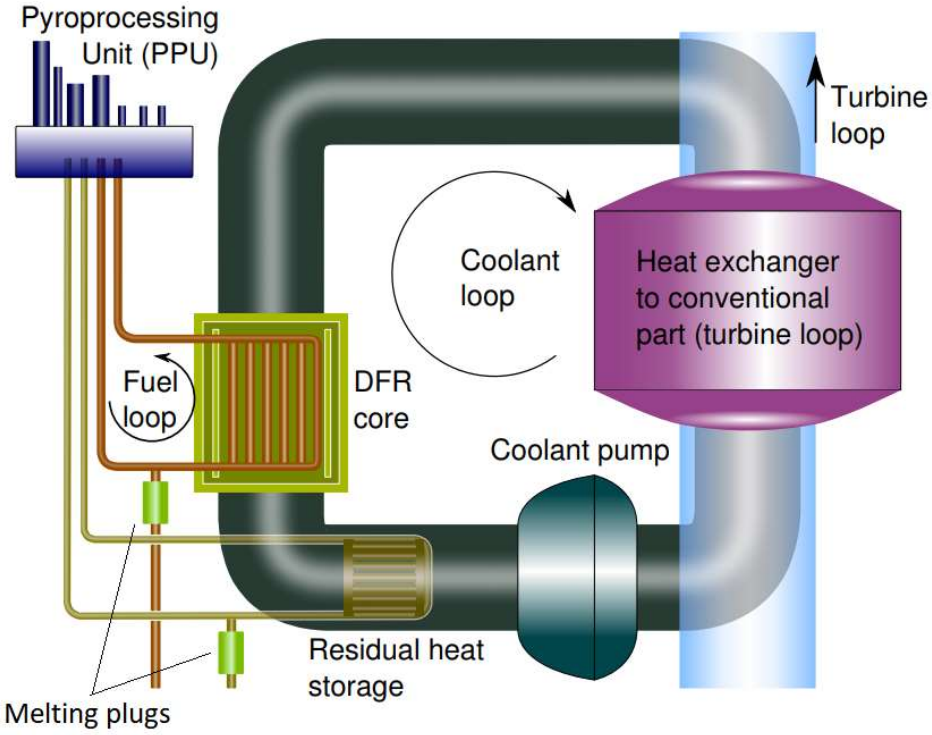

Fig. 18 Schematic view of the dual fluid reactor [25]

Chapter 2 MSRE Model

DFR, like many other molten salt reactor concepts, was never constructed. To simulate the behaviour of such a reactor, the author of this thesis decided to model MSRE. Since both MSRE and DFR are circulating fuel reactors, it will validate the modelling approach to a certain degree. The reason behind the reactor choice as a model validator is simple: MSRE was one of the two ever-built molten salt reactors and is a well-documented facility. In this chapter created Serpent model has been described.

2.1 Static neutronic simulation

In this section, the neutronic model in the Serpent code has been established.

2.1.1 MSRE model in the Serpent code

To properly model the neutronic characteristics of the DFR_m, the Serpent 2.1.31 code has been used. The Serpent is Monte Carlo-based code. It can simulate 3D systems, calculate neutron-photon distribution, and perform burnup calculations [34].

2.1.2 MSRE geometry and materials

Serpent code needs two types of data for the model: geometry data and materials data. In research [35] MSRE model has been created in Serpent to benchmark the MSRE criticality experiment from 1 June 1965 [36]. Therefore, the author of this thesis decided to prepare a similar model and use it for the criticality experiment benchmark and the regular reactor operation model.

Levels for different reactor parts can be seen in Fig. 19 and Fig. 20. Information about volumes occupied by fuel in different fuel loop parts and corresponding transit time is presented in Table 3. Dimensions for the main components of the MSRE used in the model are shown in Table 4.

Table 3 Fuel volumes in different fuel loop parts [11]

Fuel loop component	Fuel volume, ft^3	Fuel volume, m^3	transit time, s
Reactor core	25	0.708	9.4
Upper head	10.5	0.297	3.9
Reactor vessel to pump	2.1	0.0595	0.8
Pump bowl - mainstream	0.9	0.0255	0.3
Pump bowl - outside the mainstream	3.2	0.0906	-
Pump to the heat exchanger	0.8	0.0227	0.3
Heat Exchanger	6.1	0.173	2.3
Heat exchanger to the reactor vessel	2.2	0.0623	0.8
Vessel inlet	9.7	0.275	3.6
Lower head	10	0.283	3.8

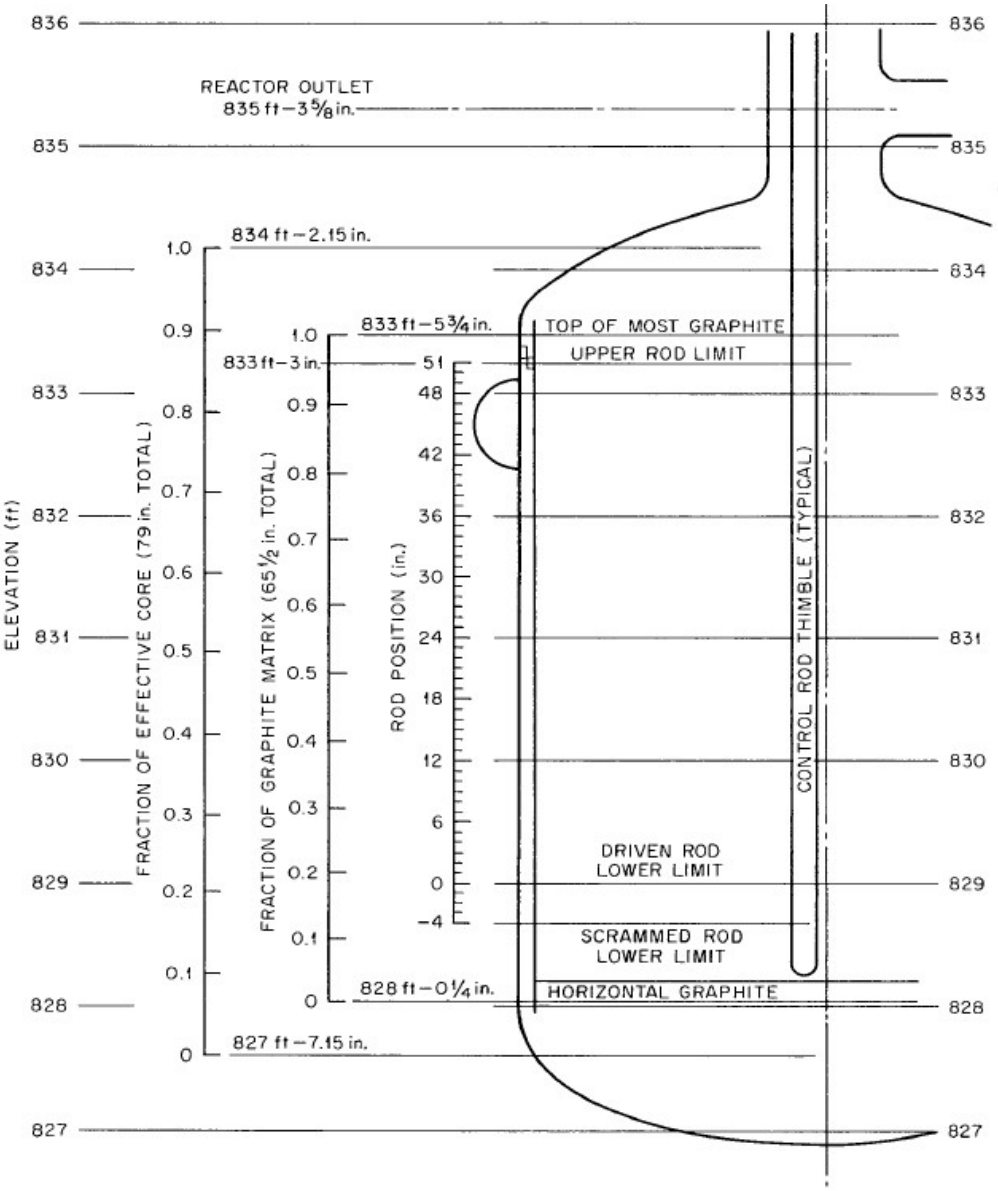

Fig. 19 Axial levels for MSRE [37]

Table 4 MSRE model dimensions

Geometry element	Dimension, cm
Graphite height in the reactor core	160.02
Graphite matrix radius	70.168
Fuel channel length	3.048
Fuel channel width	1.016
Core barrel inner radius	70.485
Core barrel outer radius	71.12
Core vessel inner radius	73.66
Core vessel outer radius	75.09
Fuel distributor inner radius	10.16
Fuel distributor outer radius	10.99
Insulation thickness	12.7
Thermal shield thickness	35.56

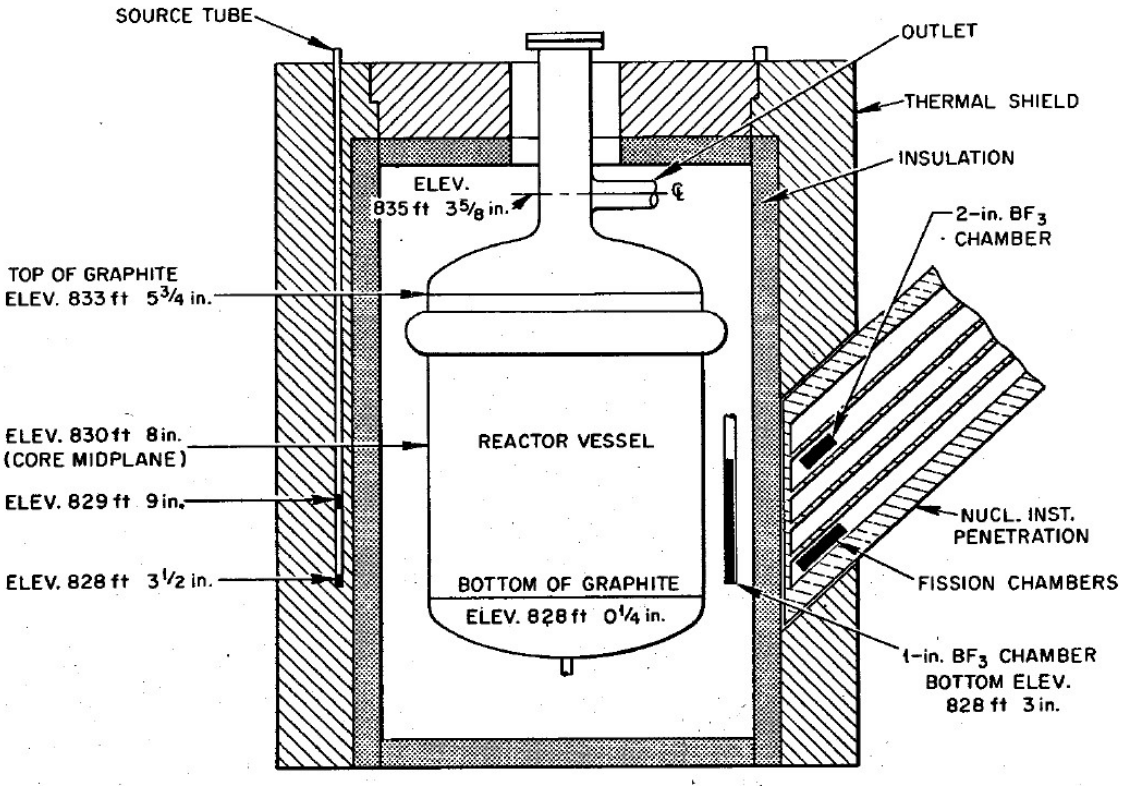

Fig. 20 Elevation levels for different MSRE parts [37]

The geometry of the MSRE model created in Serpent can be seen in Fig. 21 and Fig. 22.

The most important parts of the model are as follows: the reactor core, upper and lower head, the half-torus part, which plays the inlet

distributor role and the vertical pipe above the upper head. This vertical pipe is an outlet pipe for the fuel and where the control rods are placed.

An insulation layer and thermal shield surround the reactor vessel. The insulation layer is made of high thermal resistance material called "Careytemp 1600" to minimize heat losses. The thickness of the insulation layer is 5 inches [38]. A thermal shield is made of stainless steel and circulating water. This layer was mainly to decrease neutrons and gamma radiation escaping from the system. The thermal shield is composed of about 50% water and 50% carbon steel [39]. 1-inch stainless steel plates cover the thermal shield. A 1-inch stainless steel cover separates the thermal shield and insulation layer. In both regions: the thermal shield and insulation layer are modelled as a homogenized medium. Similarly, the lower head region is modelled as homogenized with volume proportions of 0.908 and 0.092 for fuel and INOR-8, respectively [11].

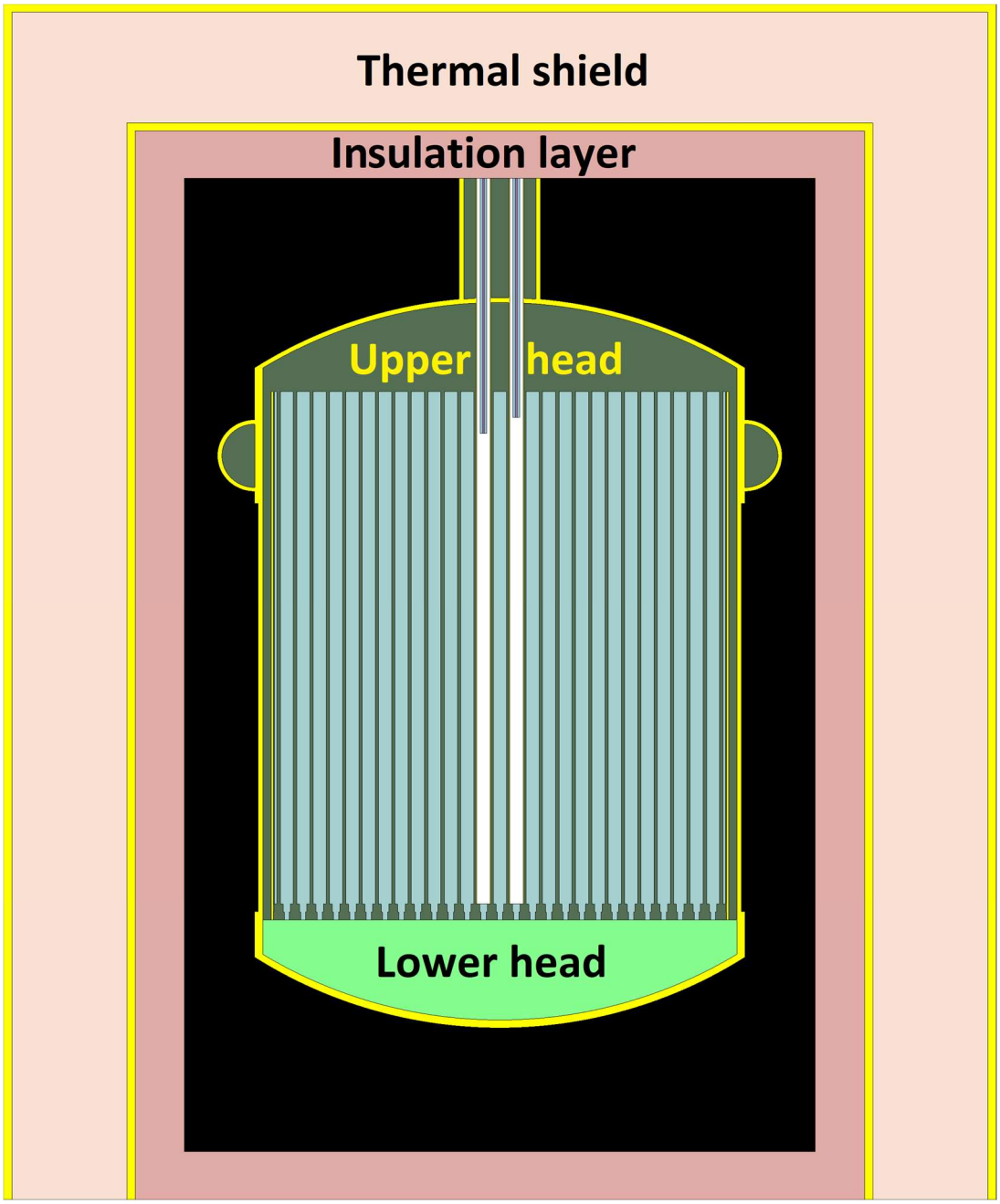

Fig. 21 Vertical cross-section of MSRE model in Serpent

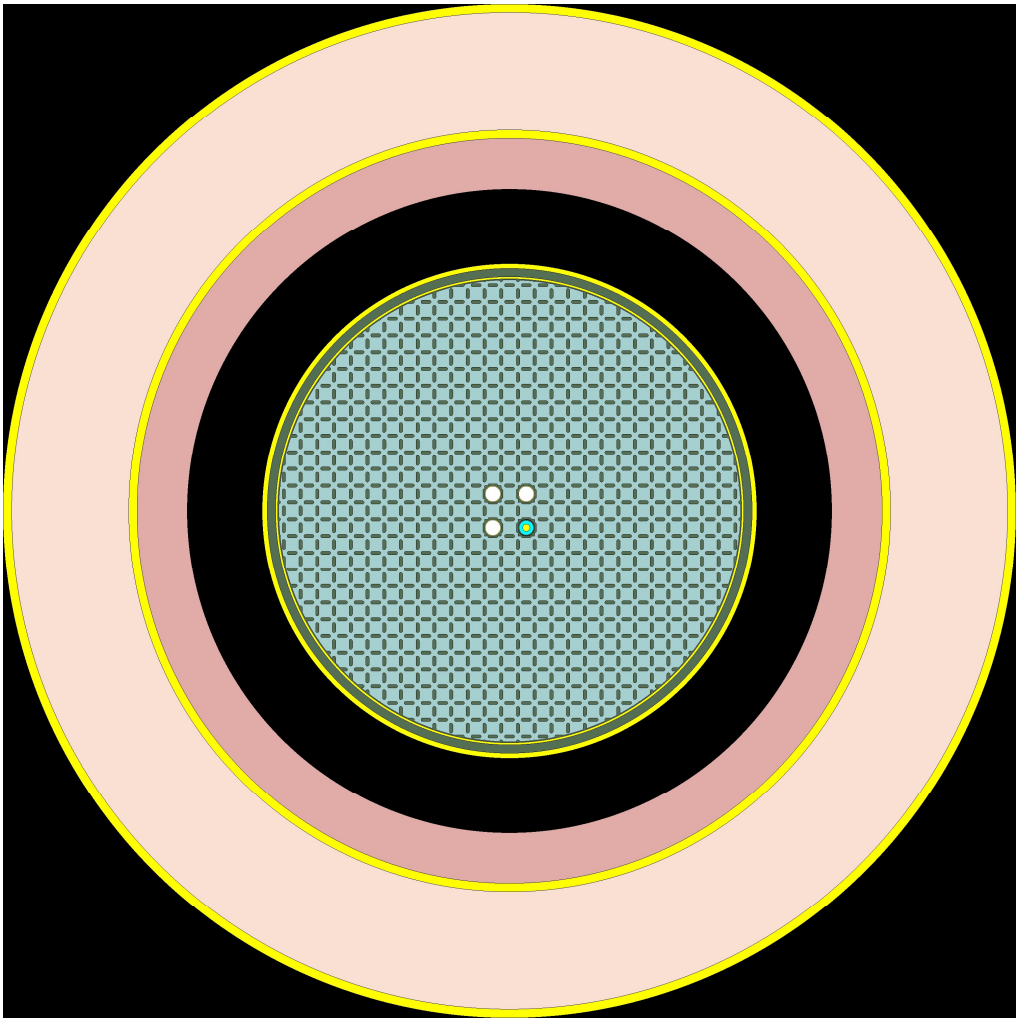

Fig. 22 Horizontal cross-section in the middle of height MSRE model in Serpent

The main materials used in the model and corresponding densities are placed in Table 5. Graphite impurities are presented in Table 6. Acronym STP means Standard Temperature and Pressure conditions - which corresponds to 273.15 K and 1 atmosphere. Graphite in the MSRE played the moderator role.

Table 5 Material densities used for MSRE model [11], [38]

Material	Density, g/cm^3
Graphite	1.86
INOR-8	8.7745
Fuel	2.3275
Insulation	0.1602
Thermal shield	4.279
304 Stainless Steel	7.56

Table 6 Graphite chemical impurities [11]

Element	quantity
Boron	0.00008 wt %
Vanadium	0.0009 wt %
Sulfur	0.0005 wt%
Oxygen	6 cm^3 of CO in STP per 100 cm^3 graphite

INOR-8 composition has been presented in Table 7. INOR-8, also called HASTELLOY-N, is a nickel-based alloy invented specially for MSRE. It was used as a structural material for places where fluoride salt was present.

Table 7 INOR-8 chemical composition [11]

Element	wt% [11]	Value used in the model
Ni	66 - 71	70.135
Mo	15 - 18	17.5
Cr	6 - 8	7
Fe	max 5	3.5
C	0.04 - 0.08	0.06
Ti + Al	max 0.5	0.25
S	max 0.02	0.01
Mn	max 1	0.5
Si	max 1	0.5
Cu	max 0.35	0.18
B	max 0.01	0.005
W	max 0.5	0.25
P	max 0.015	0.01
Co	max 0.2	0.1

Fuel salt composition has been presented in Table 8. In the second column, the initial chemical composition of the fuel has been presented. Uranium for initial fuel loading has been enriched to about 31%.

2.1.3 Sampler-enricher and off-gas system

Fuel was added through a dedicated " sampler-enricher " facility during reactor operation. This system enables to feed of the reactor during the operation (enricher part) and also to take some samples of the fuel salt (sampler part). During regular operation, a single capsule was added per 7 days. The chemical composition of the capsule is as follows: $LiF\text{-}UF_4$, with molar fractions of 73% and 27%, respectively. Each fuel capsule contains about 145 grams. Thus, it contains about 90 g of uranium. Uranium delivered by "sampler-enricher" was highly enriched - U-235 enrichment was about 93% [40]. In Table 8, in the last column, the chemical composition of the feed fuel is presented.

Table 8 Fuel salt chemical composition [41]

Element	Initial fuel, wt%	Feed fuel, wt%
Li	10.33	4.961
Be	6.7	0
Zr	11.02	0
U	4.44	61.653
F	67.51	33.386

One of the advantages of liquid fuel reactors is the capability of online fuel reprocessing. The Serpent has the option to simulate fuel reprocessing in such reactors.

Fuel reprocessing was realized for MSRE through an off-gas system. This system allows for the extraction of fission gases from fuel salt during the operation. The of-gas system works online - during reactor operation and continuously.

During MSRE operation, an off-gas system removed gases (Xe, Kr, He and H) from the fuel salt. The Off-gas system was a ring containing a lot of small holes. A schematic view of the off-gas system is presented in Fig. 23. Fig. 23 was based on the data from the report [42].

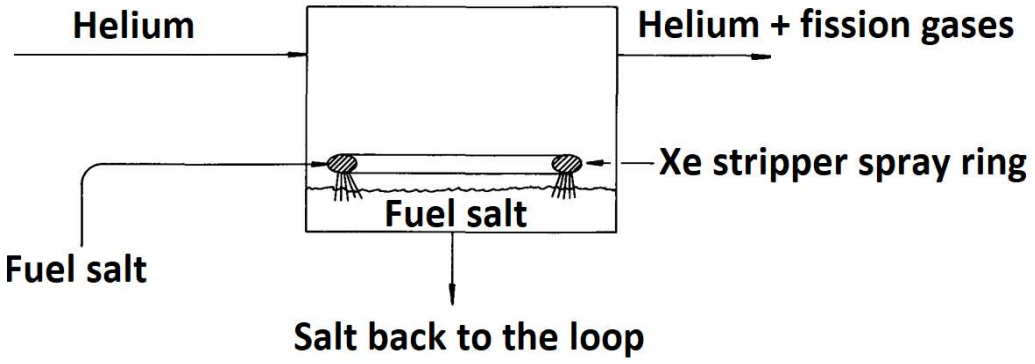

Fig. 23 MSRE off-gas system schematic view

A ring containing fuel salt was placed in the helium atmosphere. Fuel flows through this ring and sprays the fuel salt into the helium atmosphere. Fission gases stay in the helium gas, while the fuel salt, due to gravity, falls. Helium and fission products were transported to further processing.

2.1.4 Control rods

In the middle part of the reactor core, there were three control rods and 1 sample basket for irradiation purposes. A cross-section of the core's central part is presented in Fig. 10. The poison material used in control rods was gadolinium oxide. The chemical composition is Gd_2O_3 and Al_2O_3 (70% and 30% mass content, respectively). Poison has been formed into segments. Each rod consists of 32 poison segments. Segments have been developed into rings coated by the Inconel shell. Three segments are presented in Fig. 24 on the left-hand side. In the same figure, detailed dimensions can be found. Information about other materials used in different radial layers in control rods is presented in Fig. 25.

The guide tube is made from HASTELLOY-N, and the gap between the guide tube and the poison part is filled with cooling gas, which is a pressurized mixture of nitrogen and oxygen (95 and 5%, respectively). Neutron capture, scattering and other reactions cause the temperature rise of the poison material. Therefore, there is a necessity to cool this part of the system. Cooling gas is also present from the inner side of the poison material. Data for the materials and geometry used for control rods can be found in research [11] and [43]. Densities for different materials used for control rods are presented in Table 9.

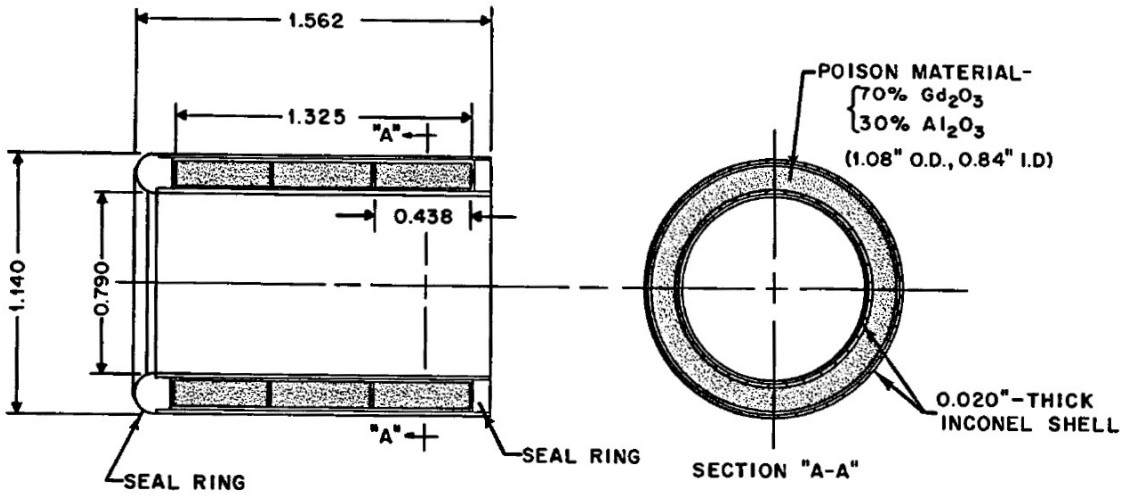

Fig. 24 Control rods poison material geometry [11]

Table 9 Material densities used in MSRE control rods [11], [37], [43],

Material	Density, g/cm^3
INOR-8	8.7745
Cooling gas	0.0009
Inconel	8.05
Poison	5.873
Stainless steel	7.56

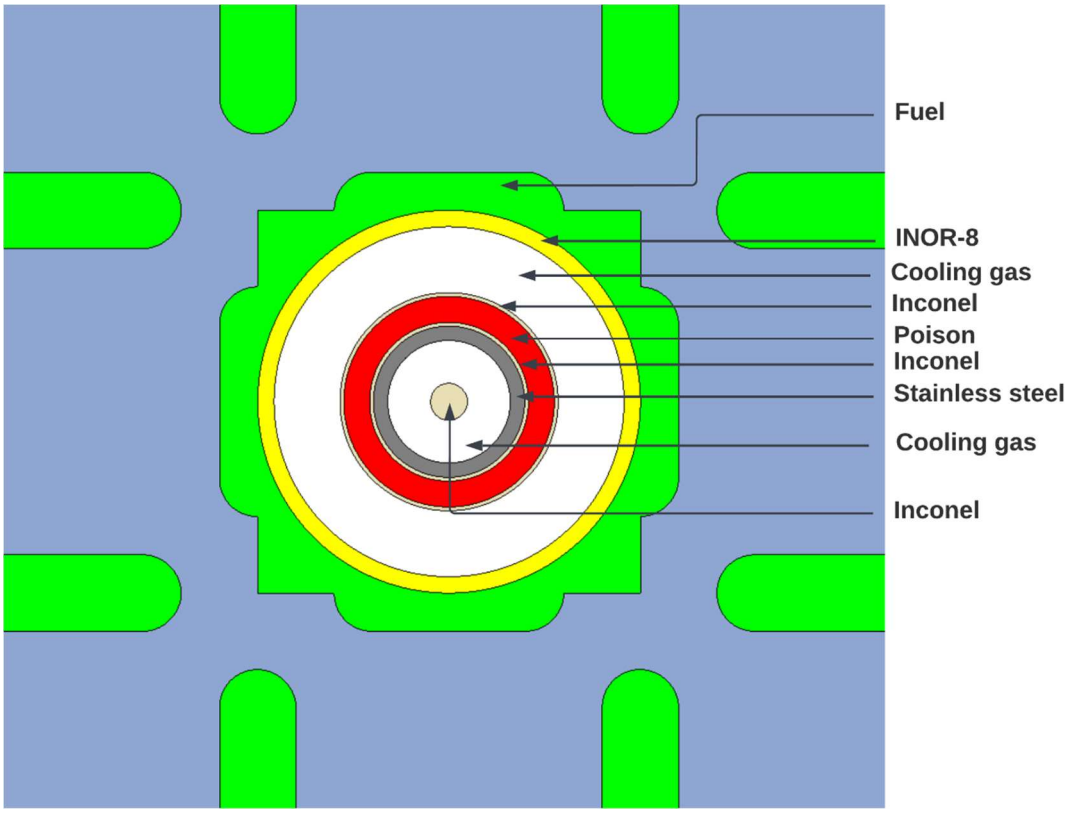

Fig. 25 Control rod radial material division.

2.2 Transient simulation

2.2.1 TRACE and SNAP code description

The Serpent is a neutronic code. Different type of code must be used to include thermal-hydraulic impact for the reactor behaviour. From many other thermal-hydraulic codes, the TRACE code has been chosen. The TRACE code, formerly called TRAC-M, is the best-estimate reactor systems code developed by the U.S. Nuclear Regulatory Commission. TRACE can be used to perform transients and steady-state analyses for PWRs and BWRs [44].

The Symbolic Nuclear Analysis Package (SNAP) is a flexible and user-friendly graphical user interface (GUI) created for NRC codes. SNAP currently includes support for the CONTAIN, COBRA, FRAPCON-3, MELCOR, PARCS, RADTRAD, RELAP5 and TRACE analysis codes. In addition, each code is supported by a separate plug-in [45].

2.2.2 Necessary modifications

TRACE has excellent capabilities, and it is a very flexible code. However, it has some drawbacks. TRACE can model only several fluids. There are as follows: nitrogen, water, heavy water, sodium, lead-bismuth, air, and helium.

In MSRE, different fluids were used as fuel and coolant. To model them, the properties of two fluids: lead-bismuth and sodium, have been changed to the properties of the MSRE coolant and fuel. The MSRE fuel and coolant properties are presented in Table 10 [46].

Such change was possible due to the modification TRACE source code. The author of this thesis modified three files: “EosDataM”, “EosInitM”, and “EosM”. The first file contains information about the molecular weight of all used fluids. In the second file - “EosInitM”, reference fluids properties for the equation of state and conditions (temperature and pressure) have been changed. In the last file - “EosM”, functions describing changes in different thermo-physical parameters as a function of temperature and pressure have been modified. After all these modifications, the source has to be compiled to produce a new executable TRACE file with modified fluids.

Another difference between standard light water reactors or any solid fuel reactors and DFR is the place of heat generation. In a typical nuclear reactor, heat is generated in the solid fuel pellets - usually made from

UO_2. However, in molten salt reactors and DFR, heat is not generated in the solid but in the liquid fuel.

Fortunately, TRACE can model such phenomena properly. One of the available TRACE components, "Fluid Power", allows users to model heat deposition directly into fluid.

The last necessary change relates to the coupling between thermal-hydraulic and neutronic calculations. TRACE has the built-in capability to change the power based on reactivity feedback from the system. It allows taking into account; delayed neutrons precursors (DNP) groups, power shape, and other essential parameters. Unfortunately, these parameters are available only for "POWER" component. This component can generate heat only in solid materials; therefore, it is unsuitable for liquid fuel reactors. Therefore, a neutronic solver, coupled with a temperature field, has to be built.

Table 10 Basic thermodynamic properties of fuel and coolant salts for MSRE [46]

Reference temperature		922 K	844 K
Reference pressure		1 bar	1 bar
Property	Unit	Fuel	Coolant
Molar weight	$\frac{g}{mol}$	41.5	33.1
Thermal conductivity	$\frac{W}{mK}$	5.535	6.054
Density	$\frac{kg}{m^3}$	1998	2267
liquidus temp.	K	722	728
Specific heat	$\frac{J}{kgK}$	1927	2000
Viscosity	$Pa\,s$	0.00827	0.001

2.2.3 Neutronic equations for transient calculations

It has been decided that, at that moment, the point-kinetic model will be sufficient to simulate reactor behaviour during transient scenarios. However, due to fuel circulation on the loop, point-kinetics equations look different than for solid, non-circulating fuel. A typical point-kinetics model can be described by a set of equations (1). The first equation describes neutron density. The second equation describes delayed neutron precursors density for six groups of neutron precursors. Finally, the equation describes DNP concentration has only two terms; production term: $\frac{\beta_i}{\Lambda} n(t)$ and destruction term: $\lambda_i C_i(t)$ - related to decay of the precursors.

$$\frac{dn(t)}{dt} = \frac{\rho(t) - \beta}{\Lambda} n(t) + \sum_{i=1}^{6} \lambda_i C_i(t)$$
$$\frac{dC_i(t)}{dt} = \frac{\beta_i}{\Lambda} n(t) - \lambda_i C_i(t) \quad (1)$$

However, for circulating fuel reactors, the situation looks different. It is because of delayed neutron precursors drift. To better understand this phenomenon, Fig. 26 have been created.

On the left-hand side, the reactor core is presented. Arrows points direction of the fuel circulation. Blue circles represent DNP. Most of the DNP is born in the middle part of the reactor core. However, many of them go through the reactor core to the upper part. Then, precursors go through the outer part of the primary loop. During this passage, a specific amount of them will decay and produce neutrons outside the reactor core. After some time, the rest of the DNP will re-enter the reactor core and decay in the reactor core.

As it is presented in Fig. 26, by blue circles, some fraction of DNP will decay outside of the reactor. Therefore, the DNP concentration re-entering the reactor is smaller than those going out of the reactor. That is qualitatively and quantitatively changed in comparison with stationary fuel reactors. It effectively decreases the number of delayed neutrons, which are crucial from the point of view of reactor kinetics and prompt criticality.

Thus, for circulating fuel reactors, the point-kinetics model can be described by a set of equations (2) [47]. Comparing the set of equations (1) and (2), it can be seen that the first equation describing neutron density is the same. However, the second equation describing DNP concertation is different. The circulating fuel case has two additional terms. First term: $\frac{C_i(t)}{\tau_c}$ represents neutron precursors which are going outside the reactor core. The denominator represents transit time in the reactor core. The longer this time is, the more precursors will decay in the reactor core and the smaller the loss of precursors.

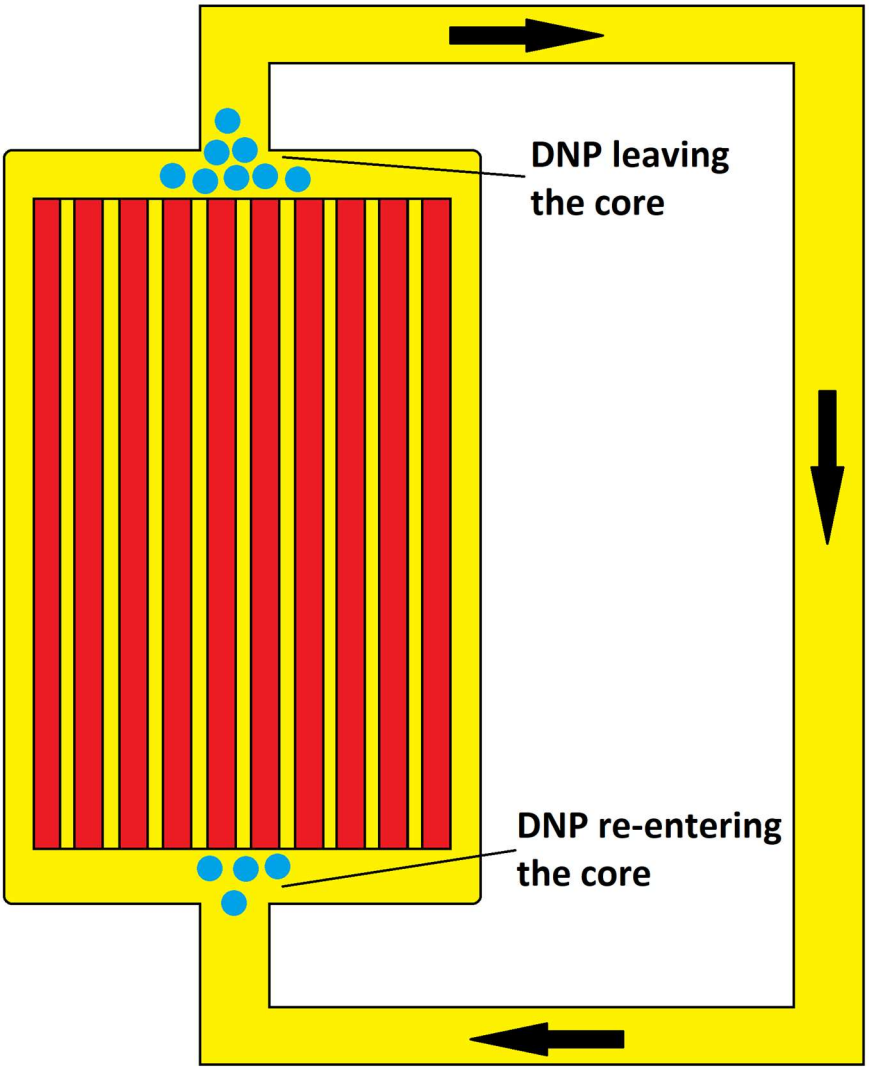

Fig. 26 Schematic view of delayed neutrons precursors loss

$$\frac{dn(t)}{dt} = \frac{\rho(t) - \beta}{\Lambda} n(t) + \sum_{i=1}^{6} \lambda_i C_i(t)$$
$$\frac{dC_i(t)}{dt} = \frac{\beta_i}{\Lambda} n(t) - \lambda_i C_i(t) - \frac{C_i(t)}{\tau_c} + \frac{C_i(t-\tau_l)}{\tau_c} e^{-\lambda_i \tau_l} \quad (2)$$

Second term: $\frac{C_i(t-\tau_l)}{\tau_c} e^{-\lambda_i \tau_l}$ represents neutron precursors that go back to the core - re-entering the core. Similarly, as it is for the first term, the bigger denominator τ_c will be, the smaller fraction of DNP will re-enter the reactor core. In the part $Ci(t-\tau_l)$, τ_l represents transit time through the primary loop, excluding the reactor core. For a specific time t, the amount of DNP which is going out from the core is equal to $C_i(t)$. At the exact moment, the amount of DNP that re-entering the core is equal to $C_i(t-\tau_l)$. The time shift - τ_l is because precursors, which are re-entering

the core, were created in the past, and their population can be different from the DNP population now. The last part of the second term is as follows: $e^{-\lambda_i \tau_l}$. It described neutrons precursors which decay outside the reactor core. The longer the time outside the reactor core (τ_l), the smaller the $e^{-\lambda_i \tau_l}$, which means a smaller overall DNP concentration. The same rule applies to the neutron's precursor decay constant-the higher the decay constant, the smaller the DNP concentration will be. However, it should be noted that a set of equations (2) can describe systems under several assumptions [47]:

- Fuel is homogenized
- Flow is at a constant rate
- Fission occurs only in the reactor core.

Therefore, a set of equations (2) cannot be used for scenarios when fuel velocity changes are noticeable.

2.2.4 Neutronic solver

Based on references [31], [48] and a set of equation (2), a similar neutronic solver was developed to simulate transient scenarios for the MSRE in TRACE. They must be rewritten to apply differential equations from (2) into TRACE code. To numerically solve the given differential equation, a set of equations (2) has been written in the form of finite differences instead of derivatives.

Lastly, a numerical scheme has to be chosen. Building a numerical scheme for seven equations (1 for neutrons density and 6 for DNP concentration) in TRACE code is a relatively tedious task. Secondly, the author decided to choose a numerically stable scheme. For those reasons, the author chose the forward-Euler scheme to implement a numerical solver. This scheme provided simplicity, but it is necessary to use sufficiently small-time step sizes h to ensure the numerical stability of the solution. TRACE has its internal algorithm to adapt timestep size during simulations. However, TRACE does not know that a neutronic solver from the available components in TRACE has been built. Therefore, running such calculations, limiting the maximum timestep size is necessary.

Fig. 27 presents the MSRE power after step reactivity insertion for three different maximum timestep sizes. It can be seen that for timestep size h=0.15 second, the numerical solver is unstable and produces huge spikes, which are unphysical and wrong. Decreasing the timestep size by 33% (from 0.15 to 0.1 seconds) is sufficient to ensure the stability of the

solver. As it is presented, reducing the timestep size further by one order of magnitude (from 0.1 to 0.01) changes the power curve very little. It means that results produced by the created solver are practically independent of the timestep size if stability is ensured.

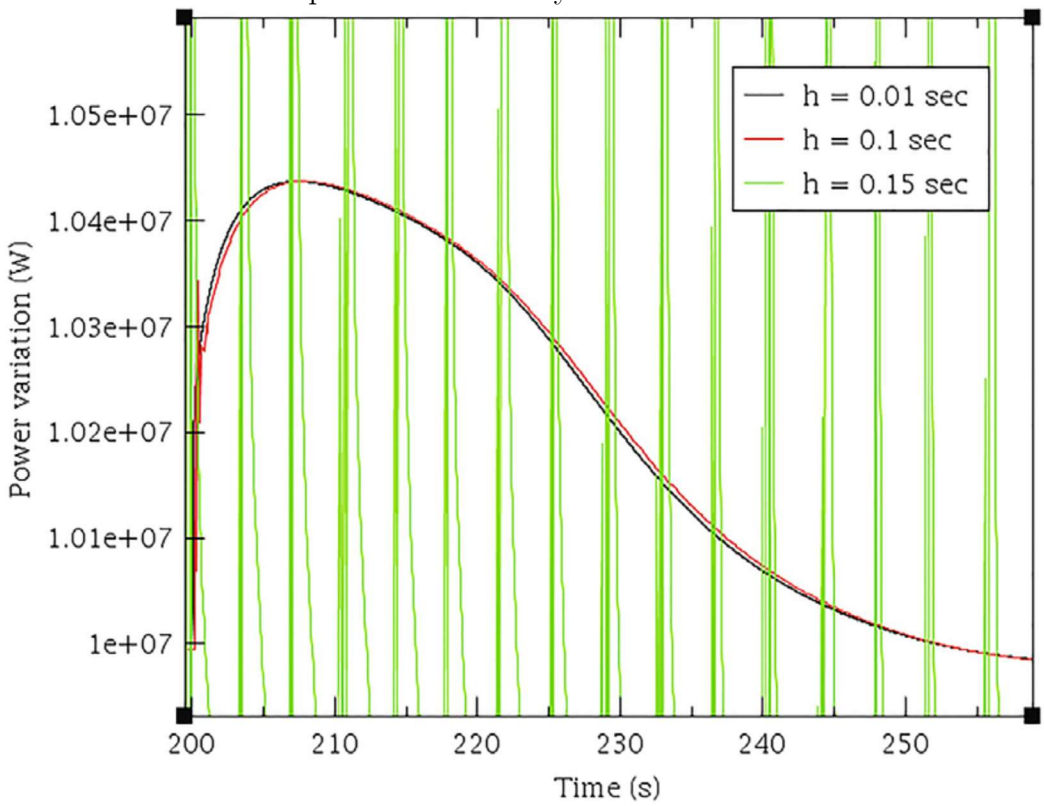

Fig. 27 MSRE power after step reactivity insertion for different timestep sizes

For the forward-Euler scheme, point-kinetics equations are presented here (3).

$$\begin{aligned} n(t+h) &= n(t) + h\left[\frac{\rho(t)-\beta}{\Lambda} n(t) + \sum_{i=1}^{6} \lambda_i C_i\right] \\ C_i(t+h) &= C_i(t) + h\left[\frac{\beta_i}{\Lambda} n(t) - \lambda_i C_i - \frac{C_i}{\tau_c} + \frac{C_i(t-\tau_l)}{\tau_c} e^{-\lambda_i \tau_l}\right] \end{aligned} \tag{3}$$

To create a neutronic solver, described by a set of equations (3), "Control Systems" need to be used. "Control systems" is a set of tools available in the TRACE code which allows for modifying, reading and manipulating parameters and variables in the TRACE code system. "Control systems" consists of the following types of components:

- "Trip data" - there are switch controllers (Boolean login - On/Off). They can activate or deactivate other TRACE components like

"control blocks" for example. Trip data components are very convenient during transient calculations to initiate some events.

- "Control blocks" - contain several classes of components.
  - "Arithmetic" - allows for basic mathematical operations like adding, dividing, multiplying, exponential.
  - "Calculus" - allows for more sophisticated calculations like differentiation, integration, logarithm.
  - "Controller" - allows for creating an "interactive variable", which can be set as a physical variable and can be used for parallel calculations in such a way as to have different values in different parallel tasks. This class also offers ready-to-use logic for switchers, PI and PID controllers and others.
- "Signal variables" - allow reading many different data types from the other components, like temperature, pressure, velocity, density, turbine torque, valve position, density, heat transfer coefficient, core power, reactivity, and many others.
- "General tables" - is a 2D table with an independent and dependent variable set of points. It can be used for such data pairs: power and time, heat flux and time, reactivity and time and many others.

In the model created by the author of this thesis, only "Control blocks" and "signal variables" has been used. An example of the control block application has been presented in Fig. 28. It shows a summation of 6 groups of delayed neutron fractions to get the total delayed neutron fraction.

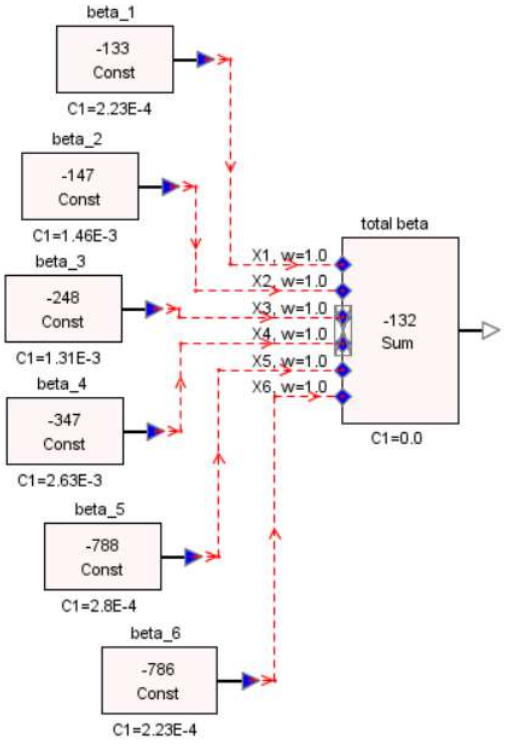

Fig. 28 Control blocks example - summation of 6 groups of delayed neutrons fractions

Another example is presented in Fig. 29. It shows part of the neutron density equation, namely the prompt neutrons generation part: $\frac{\rho(t)-\beta}{\Lambda}n(t)$. There are several inputs for reactivity: feedback from fuel, moderator and compensative reactivity. To explain compensative reactivity, solving the set of equations (2) for steady-state conditions is necessary.

Equations for the point-kinetics model differ for stationary and circulating fuel; thus, solutions are also different. Solving the set of equations (2), initial values can be calculated as presented in equations (5) and (6).

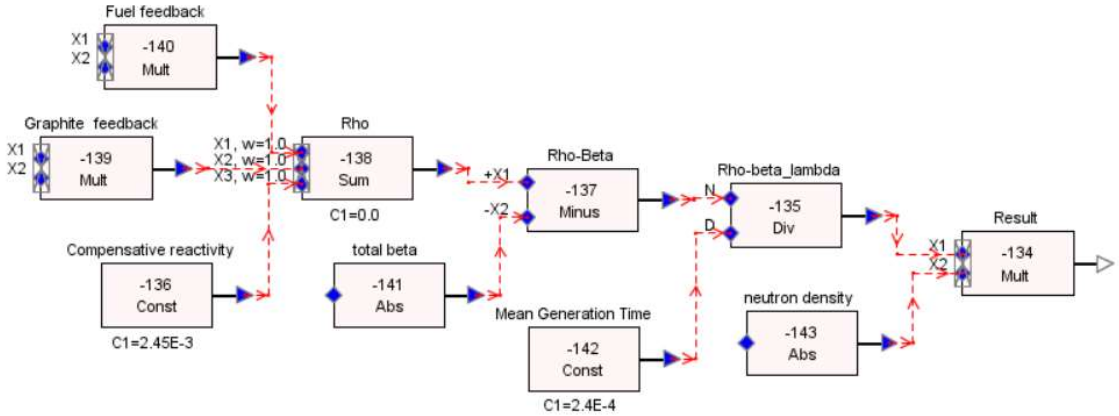

Fig. 29 Control blocks example - neutron density calculation

The parameter ρ_0 in equation (5) is also known as the **reactivity loss**. As discussed in paragraph 2.2.3, the fuel circulation causes a part of the neutron precursors to decay outside the reactor core. The number of

precursors that decay outside the reactor core differs between the number of precursors for stationary fuel and for circulating fuel. Precursor concentrations for the mentioned cases can be found based on equations (1) and (2). Assuming the same neutron density n_0 for both cases: with circulating fuel and with stationary fuel, precursors loss can be described as follows (4):

$$\text{precursors loss} = \sum_{i=1}^{6} \frac{\beta_i n_0}{\Lambda \lambda_i} - \sum_{i=1}^{6} \frac{\beta_i n_0}{\Lambda[\lambda_i + \frac{1}{\tau_c}(1 - e^{-\lambda_i \tau_l})]} \tag{4}$$

Therefore, some delayed neutrons are effectively lost outside the fission zone, making beta fractions smaller. Quantitatively this loss is equal to the **reactivity loss:** ρ_0 (5).

$$\rho_0 = \beta - \sum_{i=1}^{6} \frac{\beta_i \lambda_i}{\lambda_i + \frac{1}{\tau_c}(1 - e^{-\lambda_i \tau_l})} \tag{5}$$

The parameter C_{i0} in equation (6) represents DNP concentration. Both, C_{i0} and ρ_0 are used as initial condition and are implemented in the neutronic solver.

$$C_{i0} = \frac{\beta_i n_0}{\Lambda[\lambda_i + \frac{1}{\tau_c}(1 - e^{-\lambda_i \tau_l})]} \tag{6}$$

In Table 11 data, for the TRACE neutronic solver, for two types of fuel: U-233 and U-235 have been collected. The table includes:

- Fuel and graphite (moderator) reactivity temperature coefficients
- Mean generation time
- Neutron density
- Six groups of precursors neutrons densities
- Six groups of delayed neutron fractions and corresponding decay constants

Most of the parameters presented in Table 11 were taken from the Oak Ridge National Laboratory (ORNL) report [49]. Parameters: "compensative reactivity" and DNP concentrations have been calculated concerning equations (5) and (6). As mentioned at the beginning of Chapter 2, the primary intention of the MSRE models in Serpent and TRACE is to validate the modelling approach. To compare TRACE models with ORNL

models created for MSRE, the same data used for reference ORNL models should be used.

Table 11 Neutronic data for TRACE solver for U-235 and U-233 [49]

	235-U	233-U	Unit
Fuel temp. coefficient	-8.71	-11.3	pcm/K
Graphite temp. coefficient	-6.66	-5.81	pcm/K
Neutron generation time	$2.4*10^{-4}$	$4*10^{-4}$	s
Compensative reactivity - ρ_0	245	111.7	pcm
Neutron density	$2.7*10^{9}$	$2.7*10^{9}$	
Precursor density			
$C_{1,\,0}$	$7.33*10^{10}$	$4.43*10^{10}$	$1/cm^3$
$C_{2,\,0}$	$2.13*10^{11}$	$6.33*10^{10}$	$1/cm^3$
$C_{3,\,0}$	$1.46*10^{11}$	$1.83*10^{10}$	$1/cm^3$
$C_{4,\,0}$	$7.07*10^{10}$	$1.12*10^{10}$	$1/cm^3$
$C_{5,\,0}$	$6.85*10^{9}$	$7.3*10^{8}$	$1/cm^3$
$C_{6,\,0}$	$1*10^{9}$	$2.27*10^{8}$	$1/cm^3$
Delayed neutron fraction			
β_1	$2.23*10^{-4}$	$2.28*10^{-4}$	-
β_2	$1.46*10^{-3}$	$7.88*10^{-4}$	-
β_3	$1.31*10^{-3}$	$6.64*10^{-4}$	-
β_4	$2.63*10^{-3}$	$7.36*10^{-4}$	-
B_5	$7.66*10^{-4}$	$1.36*10^{-4}$	-
B_6	$2.8*10^{-4}$	$8.8*10^{-5}$	-
Decay constant λ_1	0.0124	0.0126	1/s
Decay constant λ_2	0.0305	0.0337	1/s
Decay constant λ_3	0.111	0.139	1/s
Decay constant λ_4	0.301	0.325	1/s
Decay constant λ_5	1.14	1.13	1/s
Decay constant λ_6	3.01	2.5	1/s

2.2.5 MSRE main components

This section presents more details about the MSRE's main components necessary to create a TRACE model. The list of these components is as follows:

- Reactor vessel
- The primary and secondary pump
- Heat exchanger

- Radiator

2.2.5.1 Reactor vessel

The reactor was partially described in sections 1.2.2 and Chapter 2. Here only complementary pieces of information are presented, mainly from the thermal-hydraulic point of view.

Fuel went from the heat exchanger to the flow distributor. It is half-torus around the reactor vessel. It was made in such a way as to distribute the fuel uniformly. Then through the holes, fuel salt went between the reactor vessel and core care - to the downcomer region. Next, fuel salt went down to the lower plenum. Here fuel is distributed and goes up to the graphite core. Next, fuel was heated and went further up to the upper plenum. Lastly, through the outlet pipe, the fuel went to the pump.

2.2.5.2 Primary and secondary pumps

The fuel and coolant pumps are quite similar. Both are centrifugal pumps. Both serve as a surge volume and expansion tank [11]. The fuel salt pump has a nominal volumetric flow rate of about 272 m^3/h and about 15 meters head. The pump's head is the maximum height that the pump can achieve, working against the gravitational force for a specific flow rate. The coolant salt pump has a nominal volumetric flow rate of about 190 m3/h and about 24 meters head.

2.2.5.3 Heat exchanger

The heat exchanger was one of the most crucial elements in the MSRE system. A schematic view of this component is presented in Fig. 30 [11]. In addition, design data regarding the heat exchanger are shown in Table 12 [11].

Table 12 MSRE heat-exchanger data [11]

Parameter	Value
Construction material	INOR-8
Shell-side	Fuel
Tube-side	Coolant
Tube pitch	19.685 mm
Tube arrangement	Triangular
Active shell length	182.88 cm
Outer shell diameter	40.64 cm
Inner shell diameter	38.1 cm
Number of U-tubes	159
The effective heat transfer surface	23.6 m^2
The logarithmic mean temperature difference	73.89
Pressure drops - shell side	1.65 bar
Pressure drops - tube side	2 bars

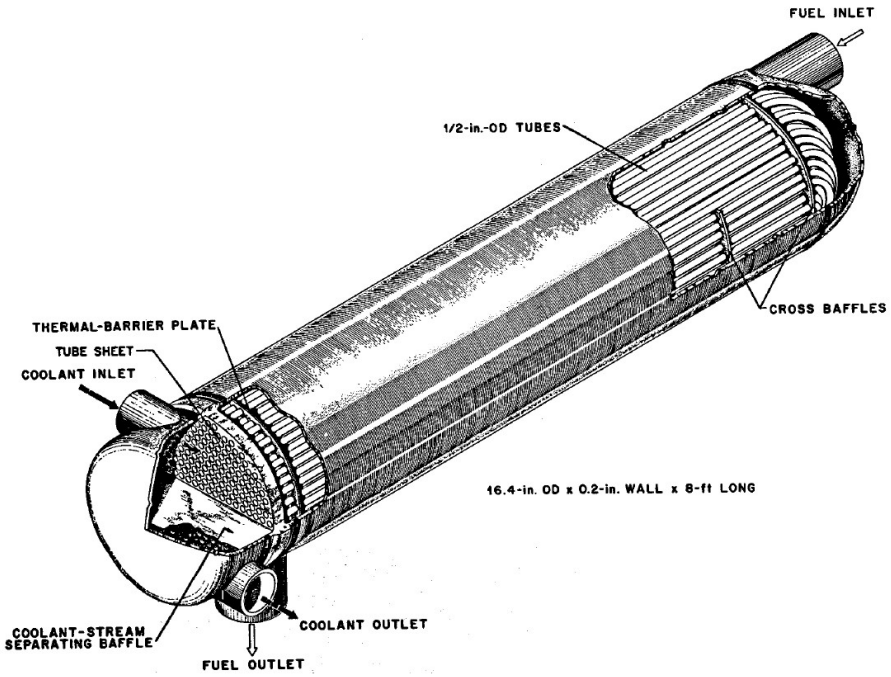

Fig. 30 Schematic view of the MSRE heat exchanger [11]

2.2.5.4 Radiator

The heat sink in the MSRE was provided by a large radiator, cooled by two air fans. Hot air goes to the stack, dissipating energy into the atmosphere. Cooled salt recirculates to the heat exchanger. A schematic view of the radiator can be seen in Fig. 31 [11]. Design data are presented in Table 13 [11].

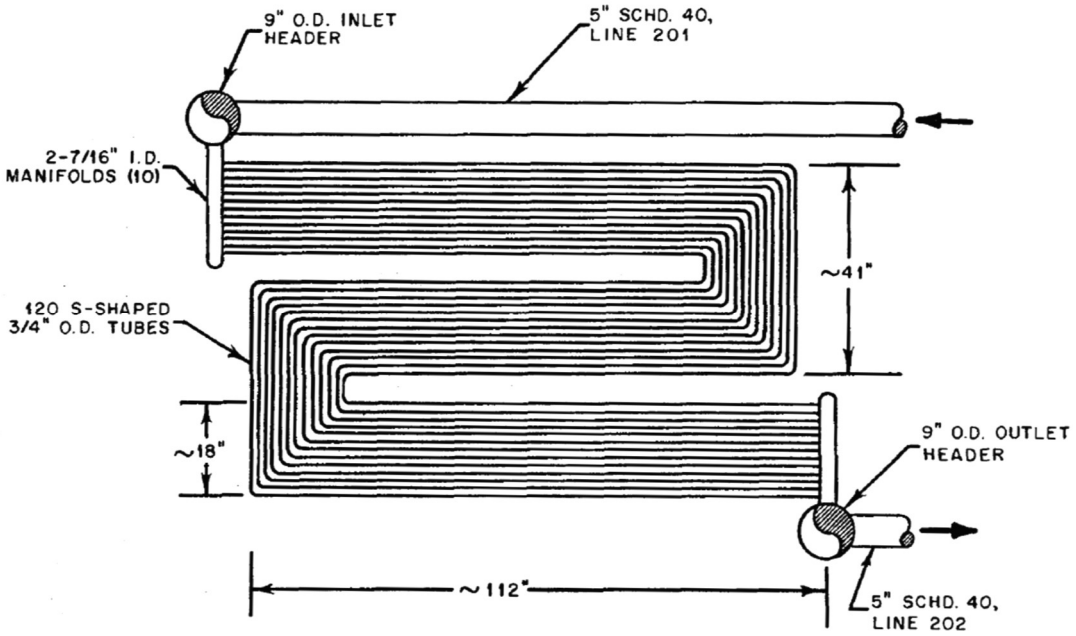

Fig. 31 MSRE radiator scheme [11]

Table 13 MSRE radiator design data [11]

Parameter	Value
Heat load	10 MW
Construction material	INOR-8
Salt temperature inlet	866.5 K
Salt temperature outlet	825 K
Salt flow	189 m^3/h
Logharitmic mean temperature difference	479 K
Tube diameter	1.905 cm
Wall thickness	0.18288 cm
Tube length	9.144 m
Tube matrix	12x10
Spaces between tubes	3.81 cm

2.2.6 Oak Ridge National models assumptions

This section contains information and assumptions regarding the ORNL model for transient and steady-state calculations (temperature profiles).

2.2.6.1 Transient simulation model

Data regarding the ORNL model for transients' scenarios can be found in reports [50] and [49]. Thermo-hydraulic model created in ORNL is presented in Fig. 32 Fig.

32 MSRE thermo-hydraulic model created in ORNL [49]. The reactor core is divided into nine regions. Each region is represented by two nodes.

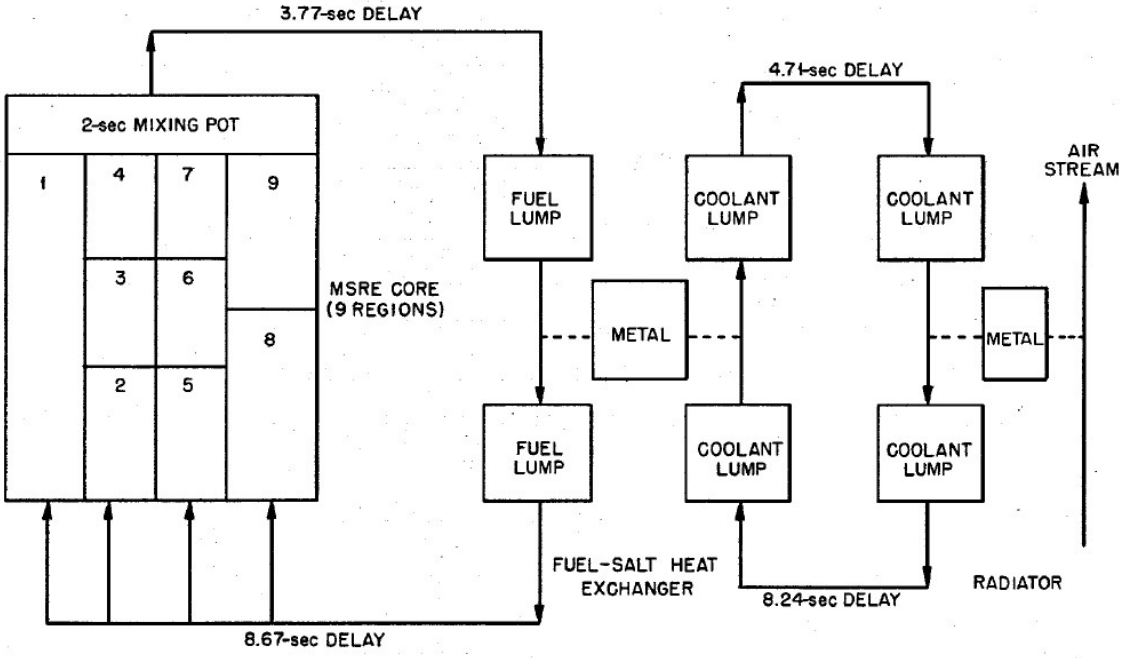

Fig. 32 MSRE thermo-hydraulic model created in ORNL [49]

Fractions of power generated in different regions in the fuel and graphite are presented in Table 14 [50]. Heat capacity for different reactor core regions is presented in Table 15 [50]. Fule-to-graphite heat transfer coefficient multiplied by the area for different reactor regions is presented in Table 16 [50].

Table 14 Power fraction for different reactor core regions [50]

	fuel salt		graphite	
core region	node 1	node 2	node 1	node 2
1	0.01493	0.01721	0.000946	0.001081
2	0.02736	0.0455	0.001685	0.00306
3	0.04504	0.04656	0.003029	0.003131
4	0.05126	0.04261	0.003447	0.002395
5	0.03601	0.06069	0.002216	0.004081
6	0.06014	0.06218	0.004044	0.004182
7	0.06845	0.05664	0.004603	0.003184
8	0.06179	0.07707	0.00392	0.005183
9	0.09333	0.07311	0.006277	0.004305

Table 15 Heat capacity for fuel and graphite regions in the reactor core [50]

	Heat capacity		
	fuel salt		graphite
core region	node 1	node 2	
1	0.0151	0.0158	0.07
2	0.0512	0.0349	0.2114
3	0.028	0.028	0.1606
4	0.035	0.0682	0.2056
5	0.0866	0.0592	0.3576
6	0.0473	0.0473	0.2718
7	0.0592	0.1152	0.3478
8	0.238	0.1384	0.9612
9	0.1615	0.271	0.9421
Unit	MJ/^{0}F	MJ/^{0}F	MJ/^{0}F

Table 16 Fuel to graphite heat transfer coefficient

core region	Heat transfer coef. Fuel to graphite - hA
1	0.000392
2	0.001204
3	0.0009
4	0.001174
5	0.001977
6	0.001525
7	0.001985
8	0.005445
9	0.00536
Unit	MW/^{0}F

2.2.6.2 Steady-state simulation model

The hydraulic model for steady-state calculations has been divided into five concentric regions [51]. The first region corresponds to the central part of the reactor core, where control rods and sample basket is placed. The second and third region corresponds to full-sized fuel channels. Forth region corresponds to partial fuel channels. Lastly, the fifth region corresponds to the downcomer. Each region has its own fuel fraction, a number of fuel channels, velocity and flowrate. Those data are collected in Table 17 [51].

Table 17 Regions for steady-state hydraulic model

Region	Channels number	Fuel fraction	Velocity, m/s	Flow rate, m^3/h
1	12	0.256	0.61	16
2	940	0.224	0.18	180
3	108	0.224	0.45	51
4	78	0.142	0.25	20
5	0	1	0.08	5.5

Fig. 33 and Fig. 34 present axial and power distributions from the ORNL model [51], respectively.

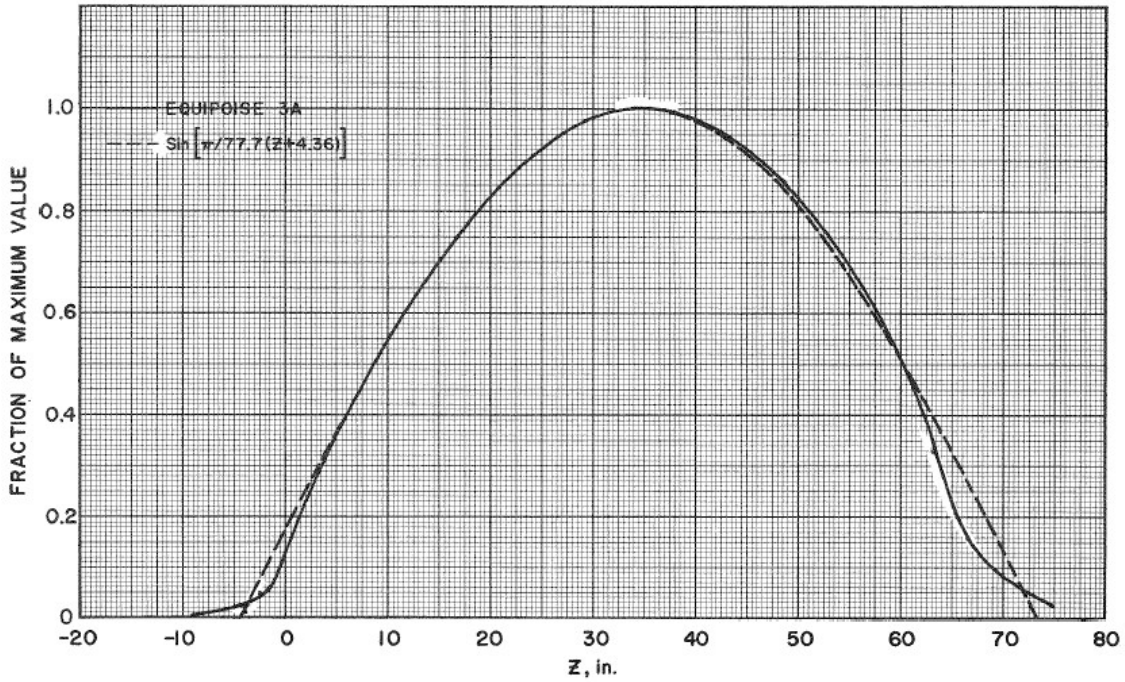

Fig. 33 Axial power distribution from ORNL steady-state model [51]

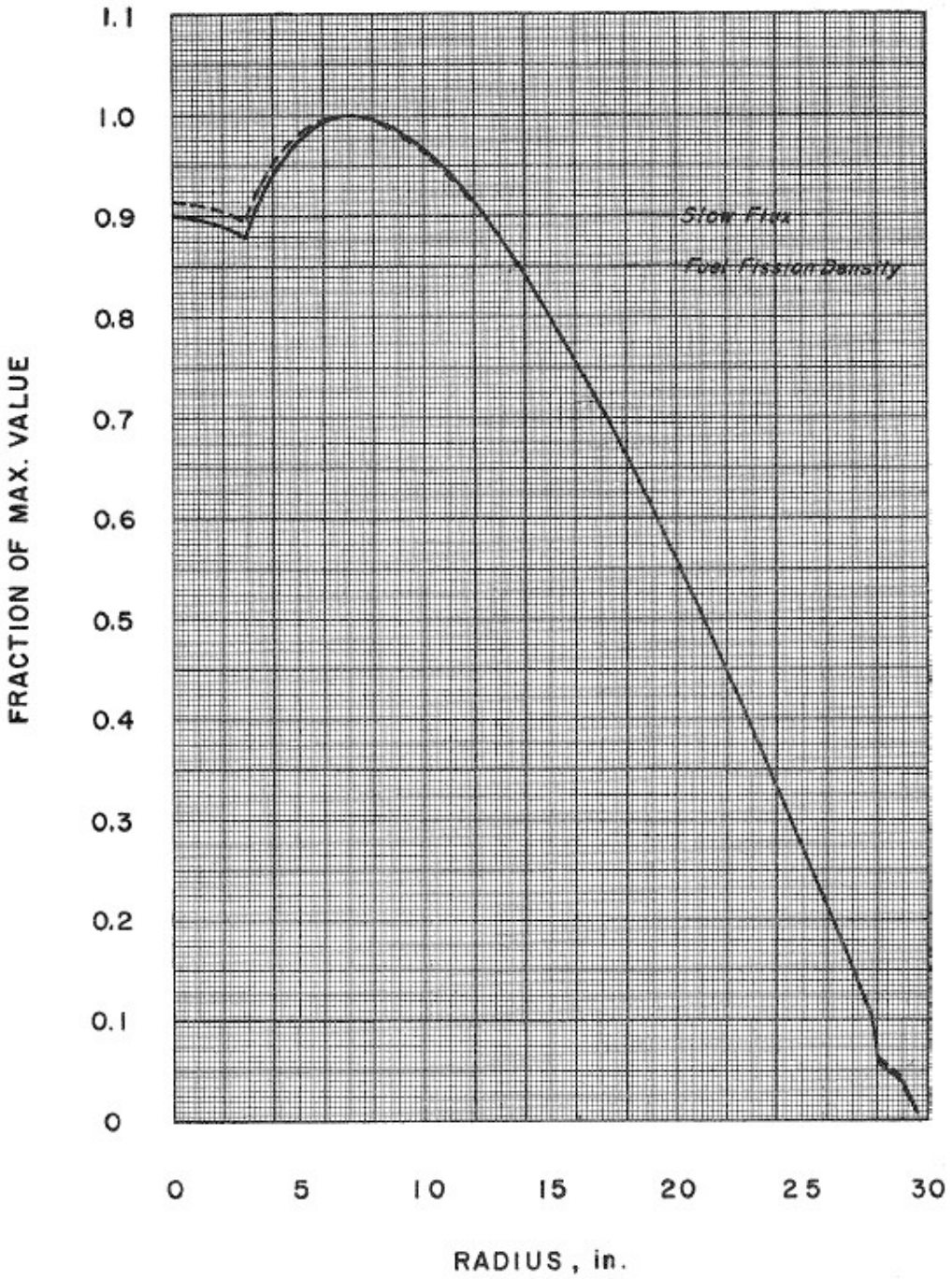

Fig. 34 Radial power distribution from ORNL steady-state model [51]

2.2.7 TRACE hydraulic model

Based on the provided data in the previous sections, a hydraulic model of the MSRE fuel and coolant loops has been created. The model is presented in Fig. 35.

Five inches pipes connect all components in the model.

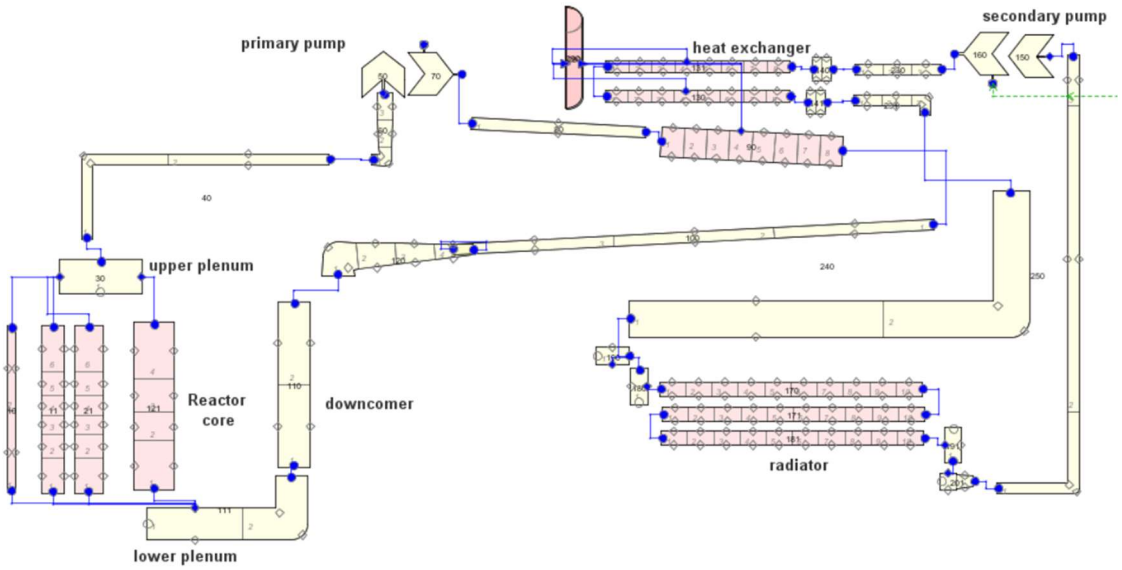

Fig. 35 MSRE TRACE hydraulic model

The thermophysical properties of the materials used in the MSRE model created in TRACE are presented in Table 18 [11].

Table 18 Properties of graphite and INOR-8 used in MSRE [11]

Property	Graphite	INOR-8	Unit
Pressure	1	1	bar
Temperature	922	922	K
Density	1900	8775	$\frac{kg}{m^3}$
Specific heat	1518	578	$\frac{J}{kgK}$
Thermal conductivity	67	22	$\frac{W}{mK}$
Emissivity	0.8	0.2	-

2.2.8 Different nodalizations

For transients' scenarios, two models have been proposed: one with flat horizontal power distribution, presented in Fig. 36, and the second with four radial rings, presented in Fig. 37. For steady-state axial temperature distribution, the model illustrated in Fig. 38 has been proposed.

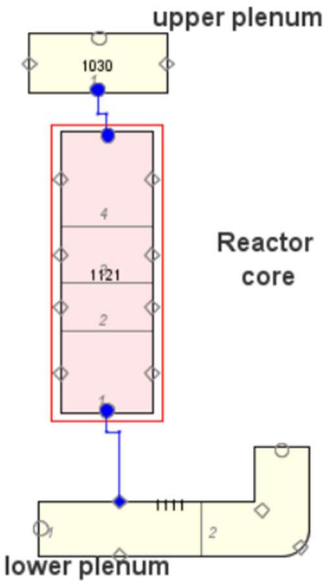

f

Fig. 36 MSRE core model with 1 radial ring

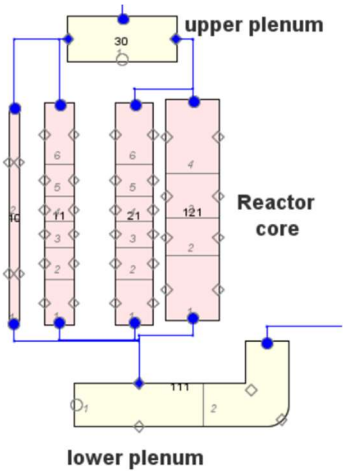

Fig. 37 MSRE core model with 3 radial rings

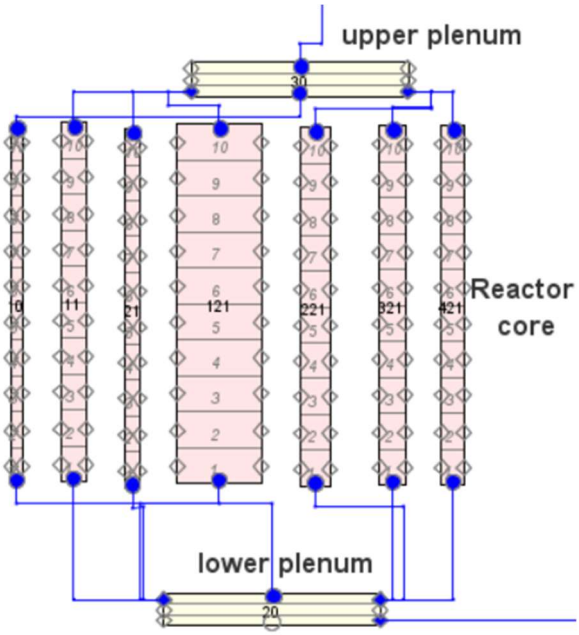

Fig. 38 MSRE core model with 7 radial rings

Chapter 3 MSRE Simulation

In Chapter 2, MSRE models in the Serpent and the TRACE codes have been presented. In the following chapter, results received from these models are established.

3.1 MSRE Serpent model results

The Serpent model of the MSRE was created mainly for benchmark author's results and Oak Ridge National Laboratory results or different reference results.

3.1.1 Criticality experiment

The first example is presented in Table 19. The table compares the results of the k_{eff} obtained from the thesis author model and results from another research [35] for the MSRE criticality experiment. The results presented in Table show good agreement between the author's model and other research results [35].

Table 19 MSRE criticality experiment benchmark results

Case	k-effective
Fratoni MSRE workshop [35] (SERPENT2, ENDF/B-VII.1 cross sections)	1.01276 ± 0.000098
Authors results (SERPENT2.1.31, ENDF/B-VII.1 cross sections)	1.00952 ± 0.00013

3.1.2 Horizontal and vertical power distribution

Another example is presented in Fig. 39 and Fig. 40. Fig. 39 shows the horizontal power distribution obtained by the author in the Serpent code and ORNL model. It can be seen that both models calculate radial power profiles with good agreement.

The most significant discrepancy can be found in the very central region of the reactor core. ORNL model was based on calculations in GNU - multigroup diffusion theory code [52]. However, diffusion theory does not work well in regions with high absorption, such as control rod regions [53]. In the middle part of the reactor, three control rods are placed. Secondly, codes based on Monte-Carlo, like Serpent, are higher accuracy than diffusion codes. Therefore, one can speculate that the ORNL model overpredicted radial power generated in the middle part of the reactor

core. Nevertheless, this is only a general rule, and only experimental validation can provide evidence of which code delivers better results.

Control rods in the reactor's middle part explain why radial power does not have a peak in the middle of the reactor.

Fig. 40 is a similar comparison. However, it presents vertical power distribution instead of radial. The author's results and ORNL model results overlap each other and show excellent agreement.

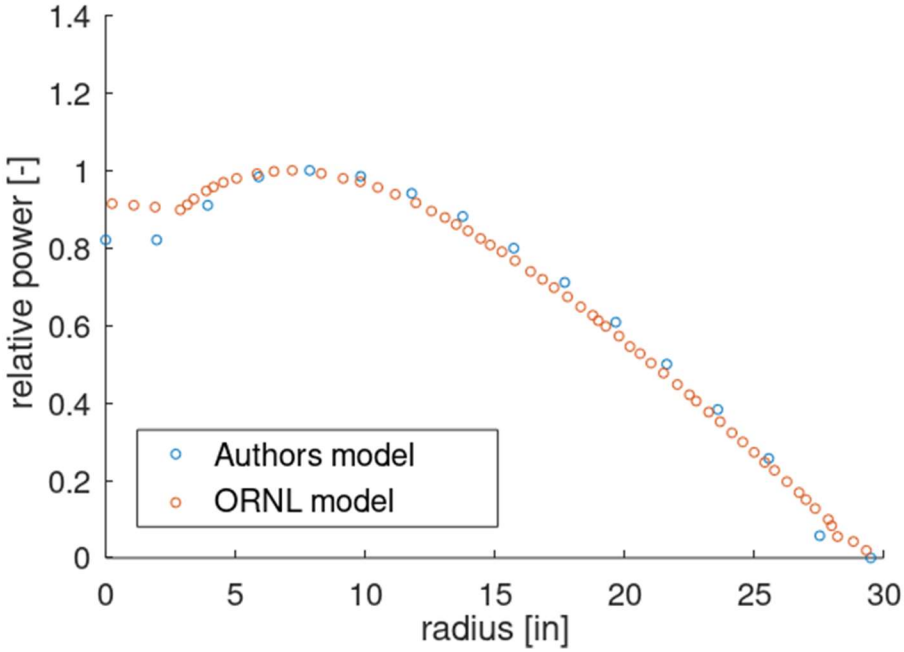

Fig. 39 MSRE horizontal power distribution. Comparison of author and ORNL models results [52]

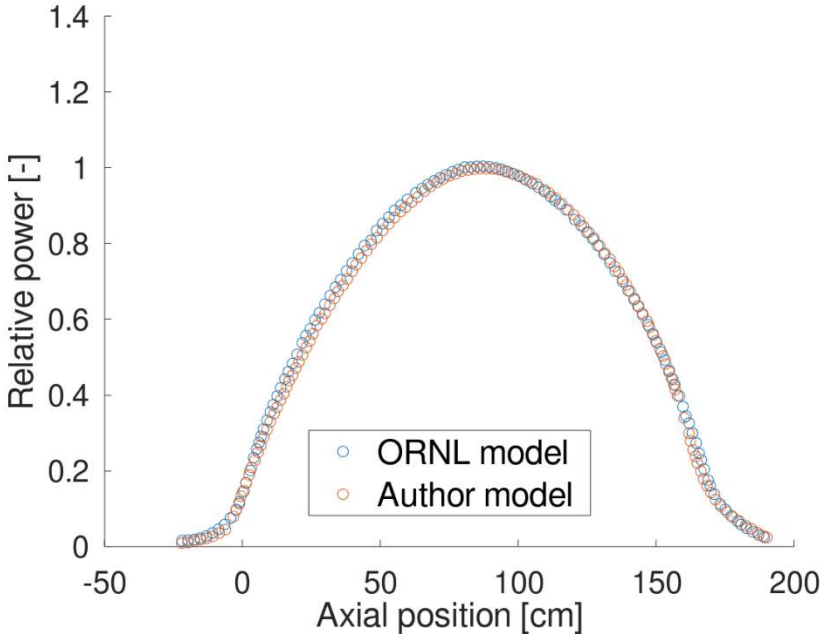

Fig. 40 MSRE vertical power distribution. Comparison of author and ORNL models results [52]

3.1.3 Fuel reprocessing

To show the impact of fuel reprocessing during the reactor operation, three different cases have been calculated:

- "Full reprocessing" - is the case where fuel is added to the reactor and fission gases are extracted. As was mentioned in section 2.1.3, the reactor was fed with one capsule per week. Each capsule contains about 90 grams of uranium, which was highly enriched - 93% of uranium 235 [40]. In the Serpent model, 100% of the efficiency of the fission gases is assumed - for simplicity. Extracted gases are as follows: Xe, Kr, He, and H [11].
- "Partial reprocessing" - in this case, fission gases are removed from the fuel salt, similarly to the "full reprocessing" case. In this scenario, fuel is not added to the system during the operation.
- "No reprocessing" - in this case, fission gases are not removed from the system. Also, fuel is not added to the reactor during the operation.

In Fig. 41 k_{eff} during one year of the MSRE operation has been presented for all 3 cases described above. It can be seen that xenon extraction can increase reactivity slightly above 1% of of k_{eff}. It is mainly because of the

large capture cross-section of Xe-135 in thermal spectrum reactors (2.6 million barns [53]).

It is also seen that in the case of feeding the reactor, k_{eff} dropped below 1.03 after about 100 days and stayed at this level till the end of the considered period.

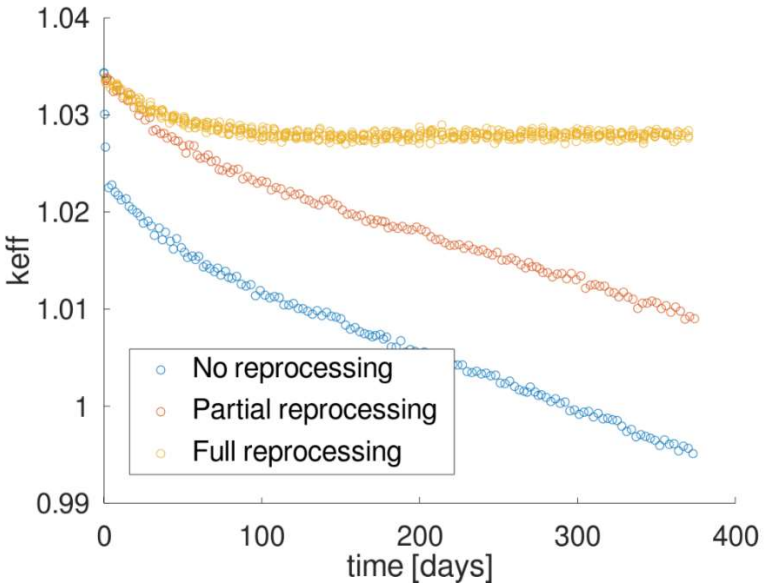

Fig. 41 MSRE multiplication factor during 1 year for different reprocessing strategies

In Fig. 42 decay heat during one year of the MSRE operation has been presented for the same scenarios mentioned above. Decay heat rises rapidly during the first several days. Then, it progresses relatively slowly during the rest of the year and has a value of about 6.4%. Moreover, it can also be seen that removing fission gases in the author's model practically did not affect decay heat. That is because all removed gaseous isotopes did not generate much heat during decay.

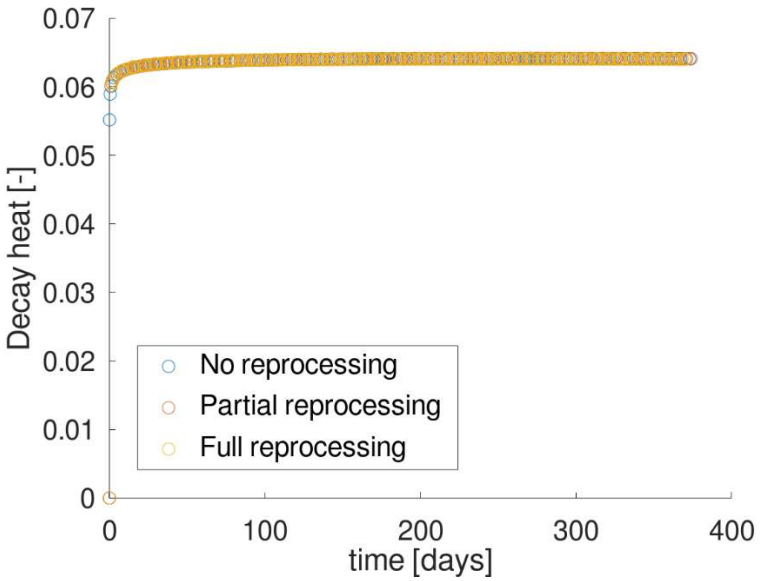

Fig. 42 MSRE decay heat during one year for different reprocessing strategies

3.2 MSRE TRACE model results

In section 2.2, the TRACE model has been presented. In this section results of this model are established.

3.2.1 MSRE axial fuel temperature

In Fig. 39, horizontal power distribution is presented. Maximum power occurs for a radial position equal to 7 inches from the mid-plane. The fuel channel, 7 inches from the mid-plane, is also the channel with the highest estimated temperature. The highest temperature in the core is a crucial parameter from many points of view:

- It has to be lower than liquid fuel safety temperature limits
- It has to be lower than the structure material temperature limits
- It can significantly affect phenomena like erosion and corrosion of the materials

A particular core model has been proposed to find temperature distribution in this channel. It is presented in Fig. 38.

Axial temperature distribution for the fuel and graphite is presented in Fig. 43. For the axial fuel distribution, the author's results are comparable with the results given by the ORNL model from research [51]. However, a more significant discrepancy can be seen for graphite temperature axial distribution. The author's model probably overestimates the wall heat transfer coefficient compared to the ORNL model from research [51].

Nevertheless, in the ORNL report [51], heat transfer coefficient is not given; therefore, it is only speculation.

When heat transfer is overestimated, the temperature difference between the wall and fluid is smaller. It can be seen that the higher the axial level, the higher the discrepancy. It is because fuel and graphite temperature, at a specific level, depends on temperature from the lower level.

Nevertheless, the obtained temperature and graphite profile trends fit well with the ORNL model data.

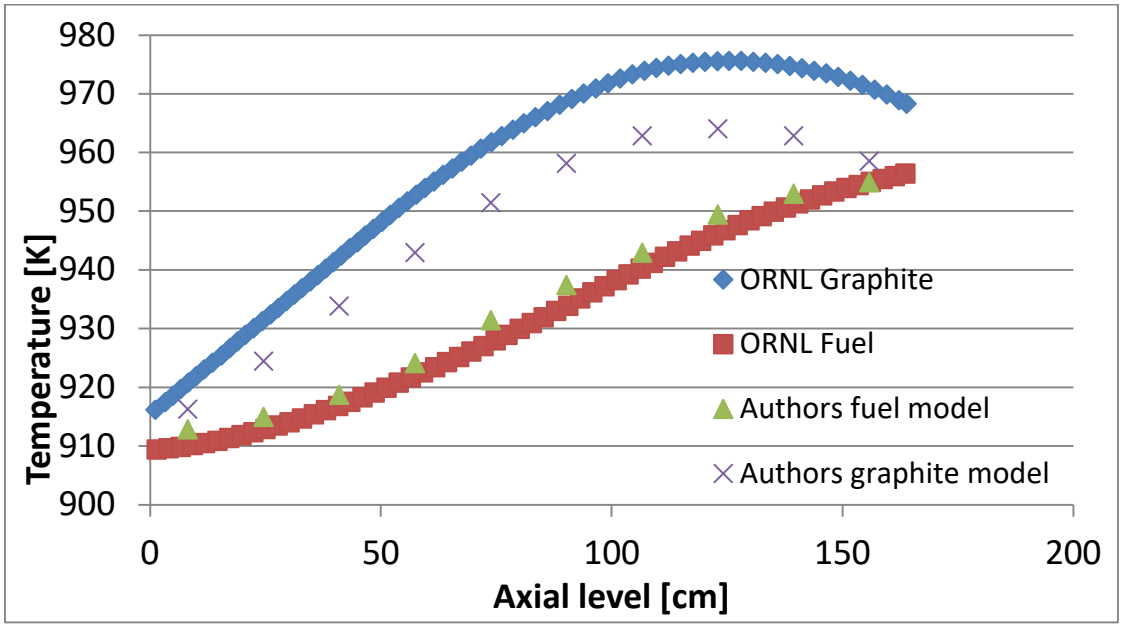

Fig. 43 MSRE hottest channel temperature axial distribution

3.2.2 MSRE transient scenarios - U-235

The prepared neutronic solver and thermal-hydraulic model can simulate the MSRE system's transient behaviour. In Fig. 44 and Fig. 45, 10 pcm has been inserted as a step function for two power levels: 1 MW and 10 MW, respectively, in the system based on U-235 fuel. For both scenarios, four results are presented. 1-ring and 4-rings models were prepared by the author of this thesis and correspond to the radial division of the reactor core. Graphical representation can be seen in Fig. 36 and Fig. 37. In Fig. 44 and Fig. 45, the green curve - "Ball1965 model" represents ORNL results from the report [50]. Blue curve - "Spinelii2010 model" represents results obtained from another research [54]. It can be seen that the "1-Ring model" does not perform as well as "4-rings" model if compared to the ORNL reference model. It shows the importance of radial nodalization. It is valid for both scenarios: 1 MW and 10 MW.

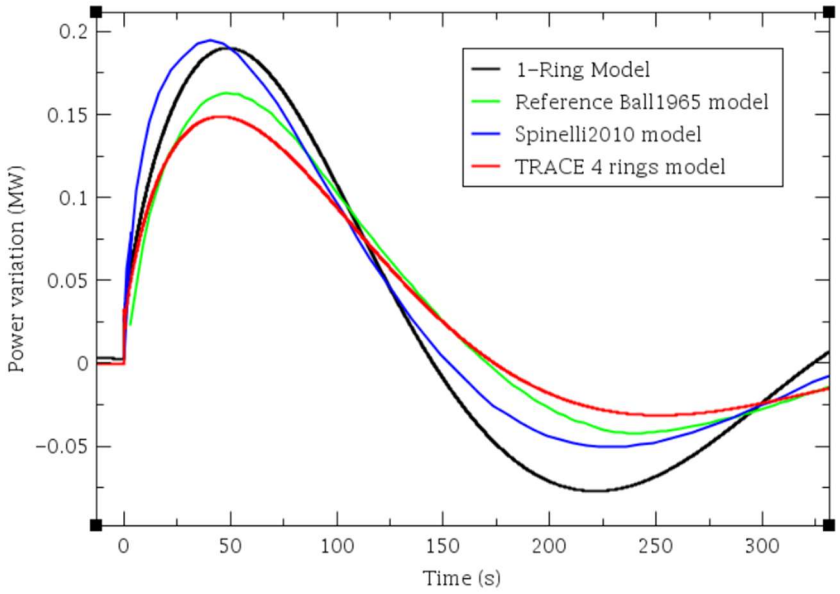

Fig. 44 MSRE power changes after 10 pcm injection for U-235 with 1 MW power

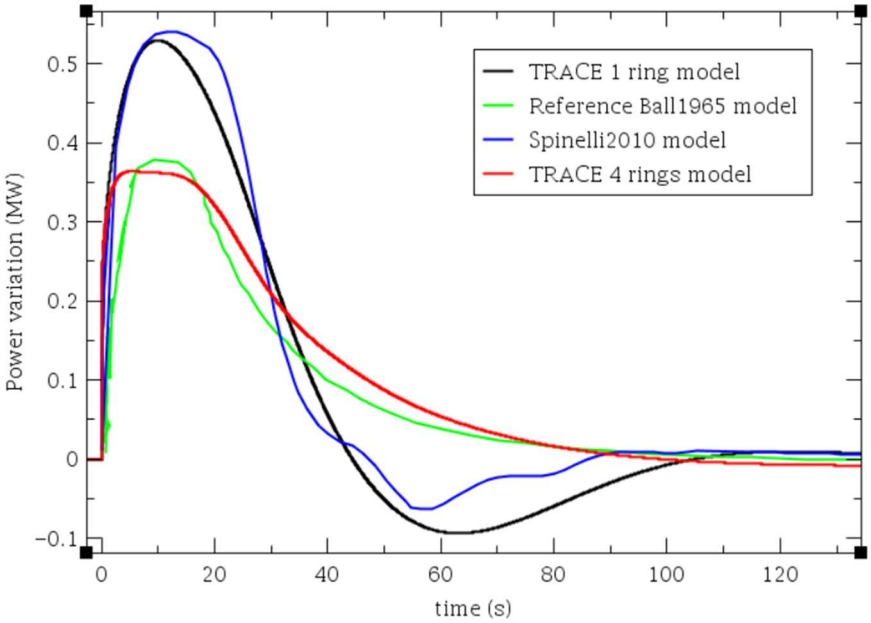

Fig. 45 MSRE power changes after 10 pcm injection for U-235 with 10 MW power

3.2.3 MSRE transient scenarios - U-233

A similar transient analysis has been performed for U-233. All Figures in this section are for step reactivity insertion equal to 20 pcm, but at different power levels.

In Fig. 46, Fig. 47, Fig. 48, Fig. 49 and Fig. 50, the reactor has the following nominal power: 0.1 MW, 0.5 MW, 1 MW, 5 MW and 8 MW, respectively.

Reference ORNL model data - “Steffy 1969” are taken from [49].

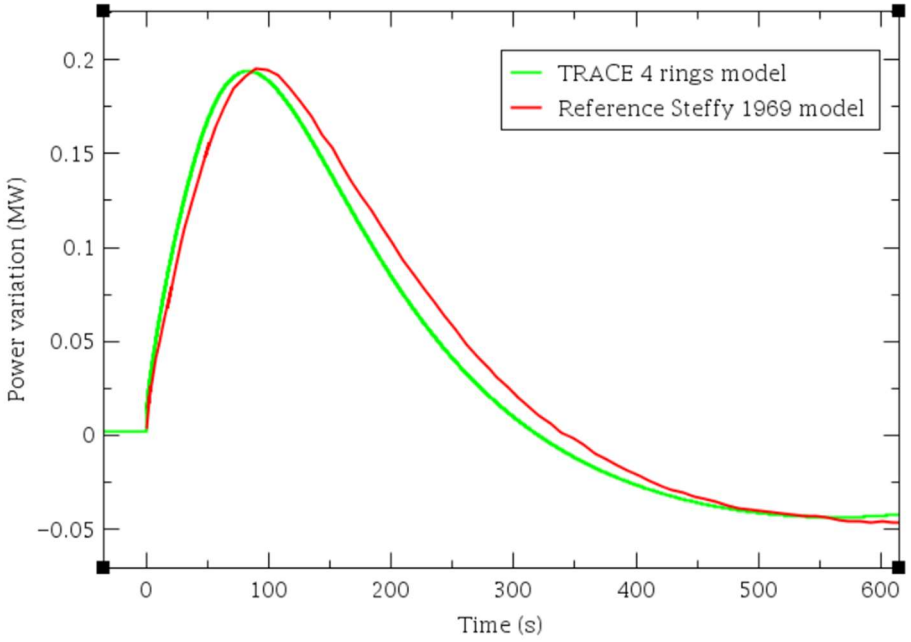

Fig. 46 MSRE power changes after 20 pcm injection for U-233 fuel with 0.1 MW reactor

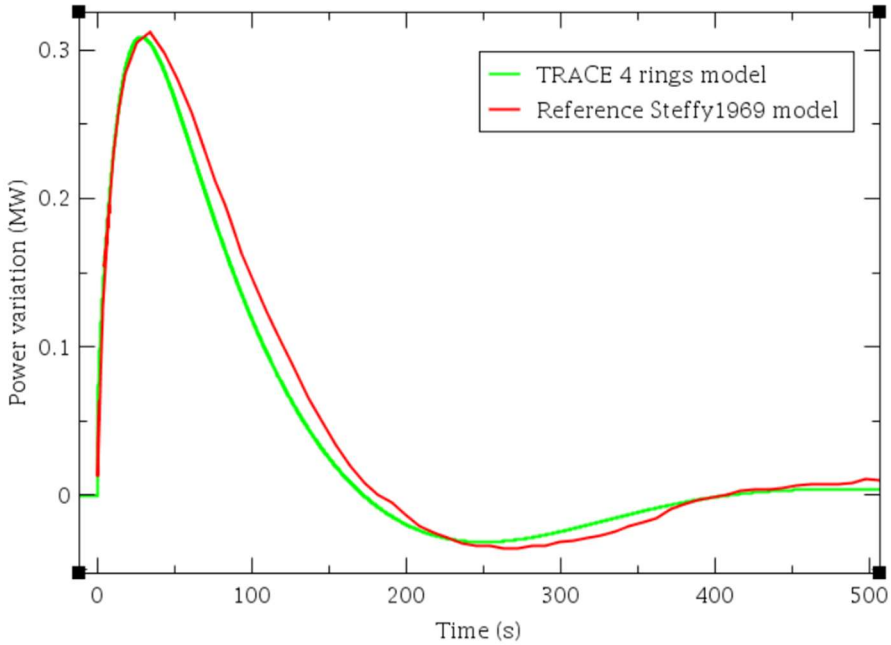

Fig. 47 MSRE power changes after 20 pcm injection for U-233 fuel with 0.5 MW reactor

It can be seen that the insertion of the same reactivity has a different impact on the power peak relative to the nominal power. For a scenario with 0.1 MW nominal power, the peak after insertion is about 0.2 MW - which is 200% of nominal capacity. For a scenario with 1 MW power, the power peak is about 0.4 MW - which is 40% of nominal power. Secondly, it can be seen that higher nominal power systems (8 MW, 5 MW nominal) are going back to the steady-state conditions faster than low power systems (0.1 MW and 0.5 MW nominal).

What is different for high and low power systems is adjustment time. First, there is a sharp power increase for high-power systems (5 MW and 8 MW). After that, the temperature rises so much that temperature reactivity feedback is stronger than the initial insertion. Thus, power is dumped very quickly. After that, power changes stabilize for several seconds (in Fig. 50, it is about 0.6 MW power level from 5 seconds to about 20 seconds - it is called the plateau region). After that, fuel which was initially heated up is re-entered into the reactor core and provides further negative reactivity feedback. Thus, the power is going to the stable, initial level.

The situation is different for the cases with low nominal power (0.1 MW and 0.5 MW nominal). The main reason is the relation between the system's power level and heat capacity. The heat capacity is the same for all the considered scenarios, and it is provided mainly by the large specific heat of graphite.

The time needed to get the balance between inserted reactivity and negative temperature reactivity feedback is longer than fuel salt circulation time. Thus, the plateau region does not appear for low-power systems. Instead of this, we can observe slow, damped oscillations.

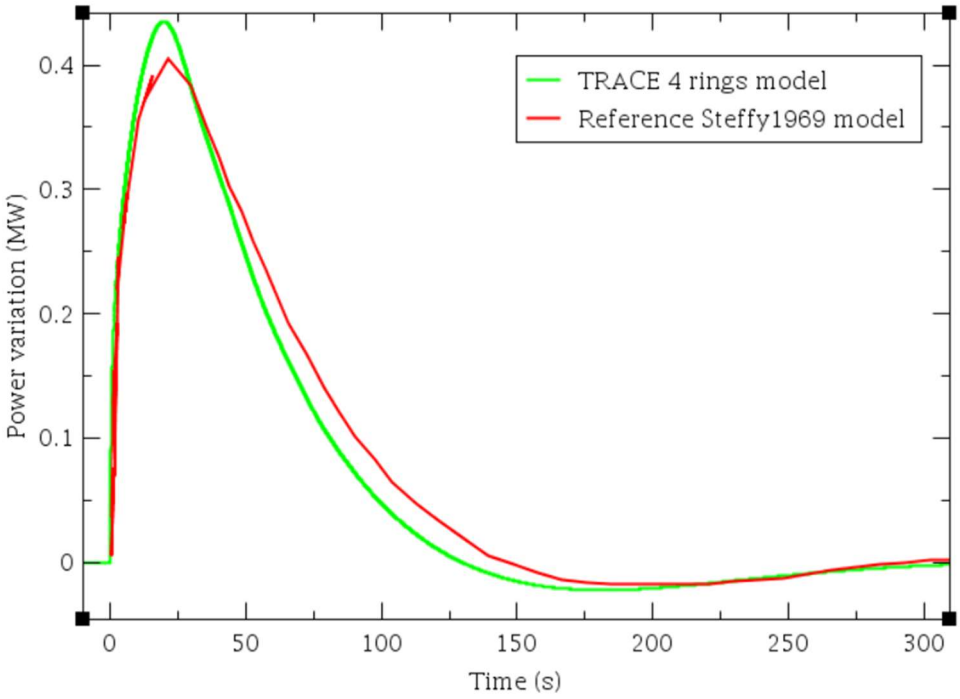

Fig. 48 MSRE power changes after 20 pcm injection for U-233 fuel with 1 MW reactor

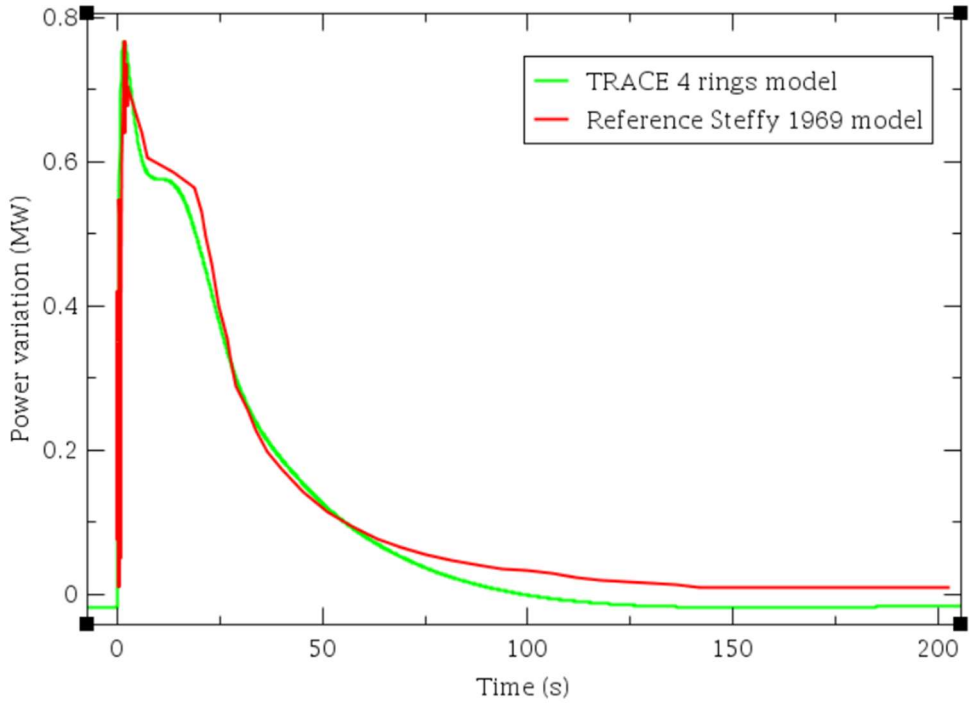

Fig. 49 MSRE power changes after 20 pcm injection for U-233 fuel with 5 MW reactor

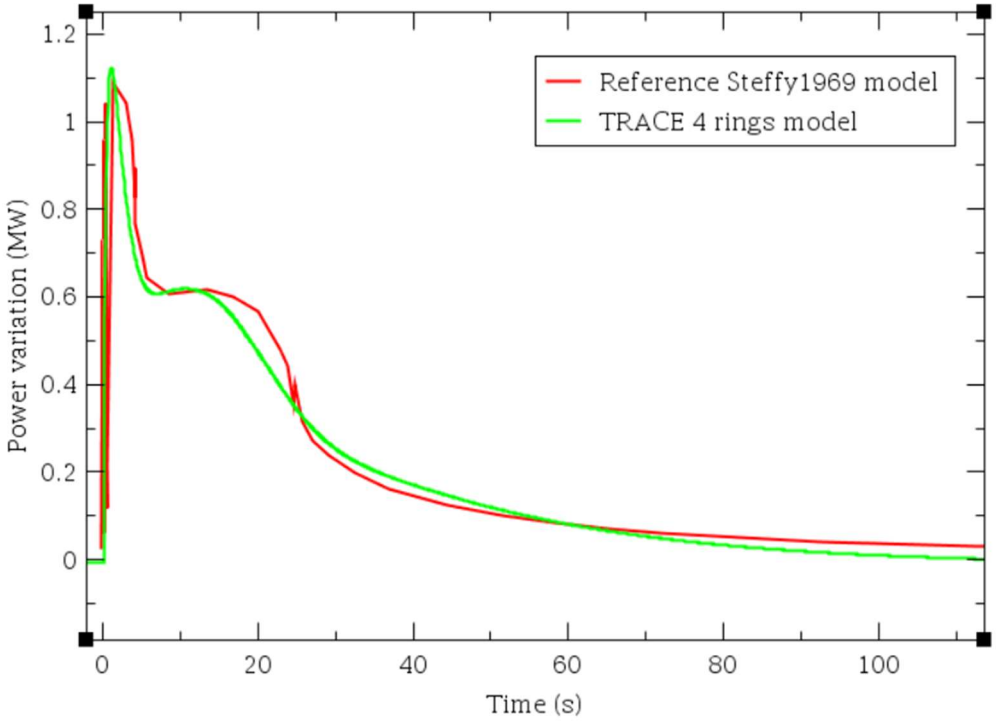

Fig. 50 MSRE power changes after 20 pcm injection for U-233 fuel with 8 MW reactor

Chapter 4 DFR Model

For DFR, the author prepared a few models based on the results received from the previous one; therefore, models and results for Serpent will be combined in this chapter.

4.1 Static neutronic simulation

Basic information regarding the Dual Fluid Reactor can be found in section 1.3.7. Here more pieces of information are provided. As was mentioned in that section, this thesis is focused on the metallic version with 250 MW thermal power, based on previous research [55], [56] and [57].

4.1.1 Geometry and materials properties for the initial Serpent model

In the model following materials have been used: uranium-chromium eutectic as fuel, silicon carbide as structural material and lead as coolant.

Dimensions for the reactor parts have been presented in Table 20. Data presented in that Table are taken from research [56]. In Table 21, material composition and densities data for materials used in the model can be found.

As a fuel, uranium-chromium eutectic has been proposed. Chromium density has been taken from research [58]. Uranium density has been taken from research [59]. Silicon carbide density and lead density have been taken from research [60] and [61], respectively.

The model created in Serpent is presented in Fig. 51, Fig. 52 and Fig. 53. Mentioned Figures present: a horizontal cross-section of the reactor core, a vertical cross-section of the reactor core and a horizontal cross-section of the inlet/outlet regions, respectively.

Table 20 DFR geometrical data

Property	**value**
Reactor height	120 cm
Inlet/outlet region height	15 cm
Reactor vessel radius	85 cm
Reactor vessel thickness	3 cm
Reflector zone thickness	30 cm
Core barrel thickness	2 cm
Pitch of the core lattice	2.8 cm
Fuel pipe inner radius	0.95 cm
Fuel pipe outer radius	1.1 cm
Number of fuel pipes	1615
Pitch of the inlet/outlet lattice	1.616 cm
I/O pipes inner radius	0.516 cm
I/O pipes outer radius	0.667 cm

Table 21 DFR materials compositions used in the Serpent model

Fuel composition	
U-235	12.8 wt. %
U-238	82.42 wt. %
Cr	4.78 wt. %
Coolant and reflector composition	
Pb	100%
Material structure composition	
SiC (silicon carbide)	100%
Material	Density function
Fuel density (12), (13)	$18.835 - 1.9548\ \mathrm{T}\ 10^{-3}\ \mathrm{g/cm^3}$
Lead density (14)	$11.367 - 1.1944\ \mathrm{T}\ 10^{-3}\ \mathrm{g/cm^3}$
SiC density (15)	3.21 $\mathrm{g/cm^3}$
B_4C density for burnable poison	2.52 $\mathrm{g/cm^3}$

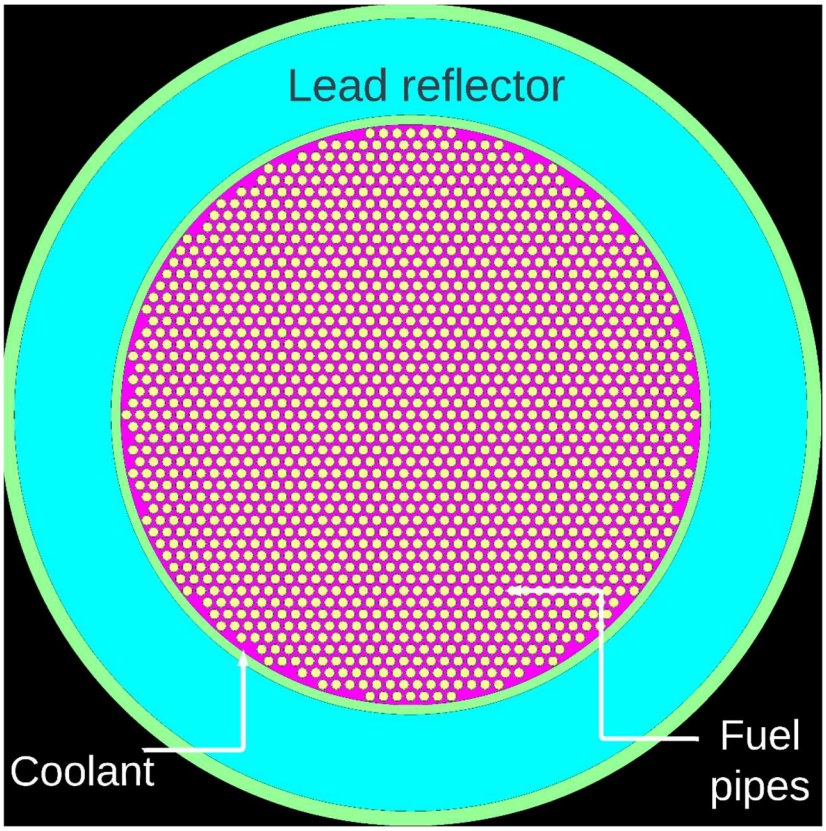

Fig. 51 DFR Serpent model horizontal cross-section - reactor core

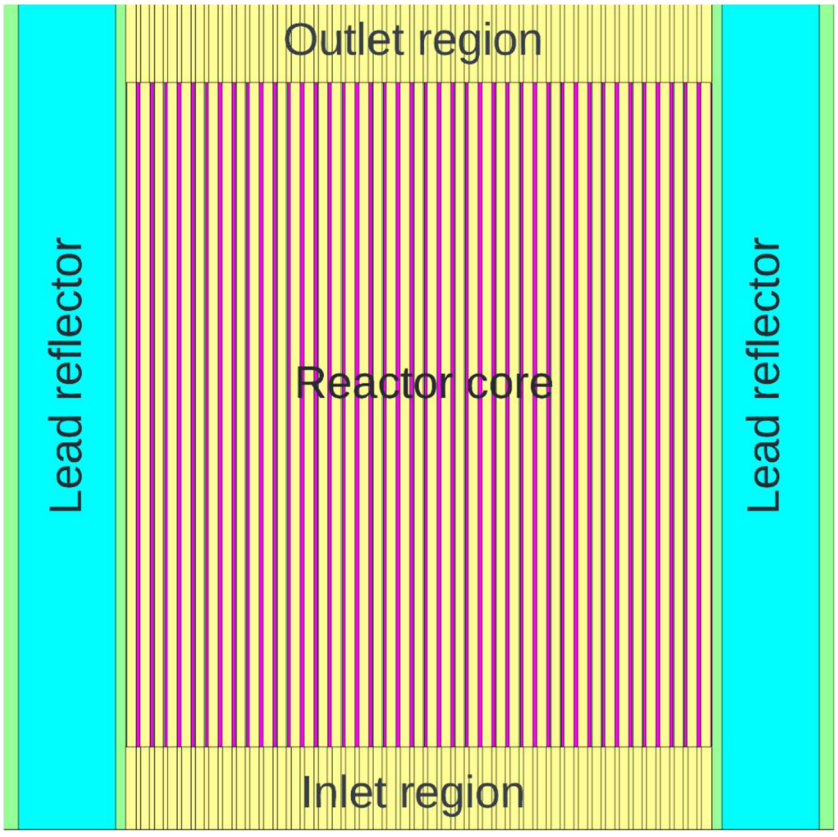

Fig. 52 DFR Serpent model vertical cross-section

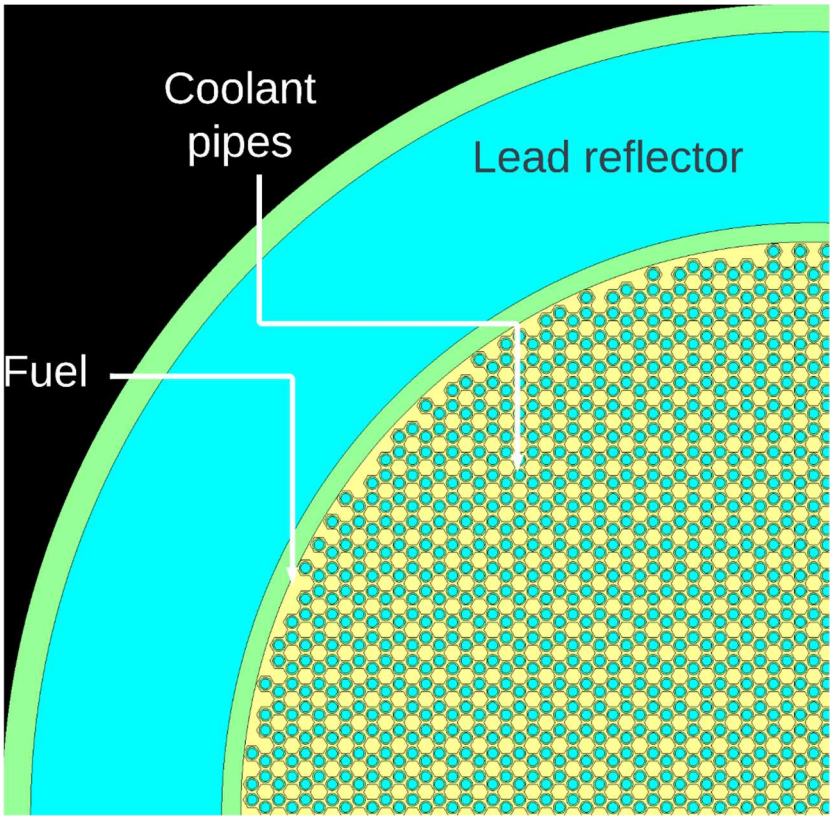

Fig. 53 DFR Serpent model horizontal cross-section - inlet/outlet regions

In the reactor core, fuel is placed inside the pipes, and coolant is outside of the pipes. In the inlet/outlet regions, the situation is the opposite - fuel is outside pipes, and coolant is in the pipes.

4.1.2 Results of the initial model

In this section, results from the model given in the previous section - 4.1.1, have been presented.

One of the ideas of the inventors of the Dual Fluid Reactor is to control the reactor only by changing fuel and coolant pump flow rates[25]. Changing those parameters, fuel and coolant temperate will be changed. Therefore, it will also change neutron balance due to the temperature reactivity coefficients of the fuel, coolant and reflector.

To calculate temperature reactivity coefficients for the fuel, coolant and reflector, Serpent burnup calculations and "branch" capability have been used. First, burnup calculations have been performed for temperature 1200 K for all materials. Then, branch calculations for 1800 K have been performed separately for fuel, coolant and reflector to see the impact of k_{eff} change for each of these materials.

The temperate reactivity coefficient, denoted as α, can be calculated with the equation (7). Subscriptions 0 and 1 refer to the initial burnup

calculations (1200 K) and elevated temperature of the material (1800 K), respectively.

$$\alpha = \frac{\Delta\rho}{\Delta T} = \left(\frac{k_1 - 1}{k_1} - \frac{k_0 - 1}{k_0}\right)\frac{1}{\Delta T} = \frac{k_1 - k_0}{k_1 k_0 (T_1 - T_0)} \tag{7}$$

Results of the temperature reactivity coefficients are collected in Table 22. Subscripts f, c, and r refer to the fuel, coolant and reflector. Calculations have been performed in Serpent 2 code, with 500 active cycles, 200 inactive cycles and 100000 neutrons per simulation. The fuel coefficient is about one order of magnitude greater than the reflector coefficient and two orders greater than the coolant coefficient.

It can be seen that the reactivity coefficient is going to be more negative with higher burnup. It is because, during burnup, the amount of fission products increases with time. Part of them has strong resonances, which could be a reason for the more negative fuel temperature coefficient for the longer-operated reactor.

The reflector temperature reactivity coefficient changes with burnup differently than the fuel temperature reactivity coefficient. In the beginning, the value is more negative, and with higher burnup, it will be less negative. The neutron energy shift probably causes this phenomenon. Increasing the lead temperature in the reflector zone will affect the neutron energy spectrum and make it harder. It means that more neutrons have higher energy than before. For higher burnup, there is less U-235 and more Pu-239. Pu-239 has a lower capture-to-fission ratio than U-235. Therefore, shifting the energy spectrum to higher energy will produce more neutrons in case of higher Pu-239 content.

The coolant temperature reactivity coefficient seems to behave similarly; one can speculate it has the same explanation. However, the difference between k_{eff} for 1200 and 1800 K is so small that calculated uncertainties for temperature reactivity coefficient for coolant are comparable with obtained values.

As it has been presented in Table 22, the temperature reactivity coefficient for coolant varies from -0.0623 to 0.0406 pcm/K. Uncertain propagation has been performed, assuming the confidence interval to be 95%. As a result, the uncertainty for the temperature reactivity coefficient for coolant is about 0.03 to 0.04 pcm/K. Comparing this value with the temperature reactivity coefficient, it can be seen that uncertainty is the same order of magnitude as the calculated value. Therefore, it can be postulated that the temperature reactivity coefficient for coolant is small and close to 0 value.

In thermal, solid fuel reactors, the doppler effect is the main contributor to the negative temperature coefficient. Due to a higher temperature, the thermal motion of the fuel nuclei is more significant. Thus, effectively, resonance peaks in the so-called resonance region are broader. Therefore, neutrons' chances to avoid capture (mainly by U-238) during the thermalisation process will be lower.

Nevertheless, this mechanism is not working efficiently for fast reactors. It is because, in fast systems, neutrons are moderated very little. Thus, the impact of broadening capture cross-section peaks is smaller. It is the main reason most fast reactors are short and thick compared with thermal reactors. Such reactor design ensures a negative temperature coefficient based on the thermal expansion of the reactor core.

However, the situation is also different for liquid and circulating fuel reactors. In case of fuel temperature rise due to thermal expansion, some fraction of the fuel will be pushed-out from the reactor fission zone. Therefore, it will decrease the number of fissile isotopes and reduce the multiplication factor. This mechanism is valid for reactors such as MSRE and DFR.

Table 22 Temperature reactivity coefficients for fuel, coolant and reflector for different burnup

BU MWd/kg	α_f pcm/K	α_r pcm/K	α_c pcm/K
0	-3.23	-2.93 E-01	-5.5 E-02
3.6	-3.34	-2.86 E-01	-4.76 E-02
11.6	-3.45	-2.98 E-01	-6.23 E-02
27.6	-3.59	-3.04 E-01	1.32 E-02
43.6	-3.79	-2.52 E-01	1.37 E-02
59.6	-3.95	-2.54 E-01	4.06 E-02
Average	**-3.56**	**-2.81 E-01**	**-1.62 E-02**

Based on the presented data in Table 22, it can be seen that the fuel temperature coefficient has the most significant impact on the negative temperature feedback of the reactor. As was mentioned, the fuel temperature coefficient is much stronger than the coolant and reflector coefficient. As it is presented, the coolant coefficient became positive for a few burnup points. Nevertheless, those value has considerable uncertainty, as was mentioned. Moreover, there are two orders of magnitude smaller than the negative fuel coefficient. Thus, the impact is

negligible even if the coolant coefficient is positive.
As was mentioned, the fuel temperature coefficient is much stronger than the rest of the calculated coefficients. However, it is still one order of magnitude smaller than the temperature coefficient for the salt version of the DFR, which is based on chloride salts. In research [62] the temperature reactivity coefficient for fuel salt was calculated and is about -40 pcm/K.

Fuel has to operate above the melting point of the uranium-chromium eutectic, which is about 1133 K [63]. From the upper side, the temperature limit for SiC, based on research [64], is found to be about 1923 K. Over this temperature, SiC is no longer elastic and starts to deform under stress. However, the temperature should be closer to lower limits because of erosion and corrosion problem at high temperatures.

In Fig. 54, k_{eff} changes during reactor operation for three different temperatures have been presented. It is for 1200 K, 1500 and 1800 K. It can be seen that elevating the temperature of the fuel will not decrease keff enough to make the reactor critical. Therefore, some modifications have been proposed, shown in the next section- 4.1.3.

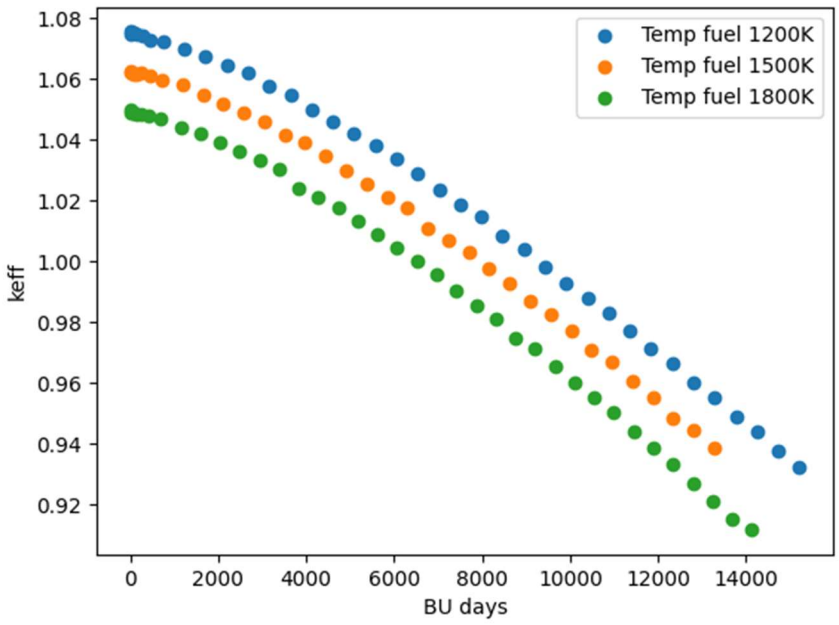

Fig. 54 keff changes during reactor operation for 3 different fuel temperatures

4.1.3 Geometry and fuel composition modifications

The author decided to modify the thickness of the reflector - now thickness is equal to 30 cm instead of 20 cm. The second modification is

to decrease the enrichment of the uranium to correspond fuel composition presented in Table 23.

Table 23 DFR fuel composition after modification

Fuel composition	
U-235	11.2 wt. %
U-238	84.02 wt. %
Cr	4.78 wt. %

For such changes, burnup calculations have been performed for 1200 K isothermal temperature for all materials. Results can be seen in Fig. 55 as a blue dot set. The orange dots in Fig. 55 represent the SCRAM case - insertion of the control rod assemblies - this case will be described later. The multiplication factor at the beginning is slightly above one, increasing with time till about 2500 days. After that, it gets a maximum of about 1700 pcm excess. After 2500 days, keff starts to decline. After about 5400 days of operation, the excess reactivity is low and close to 1. To keep the reactor working, the reactor is started to be fed. The feed rate corresponds to about 250 grams of fuel per week. The fuel capsule added to the fuel during operation has the same composition as that presented in Table 23.

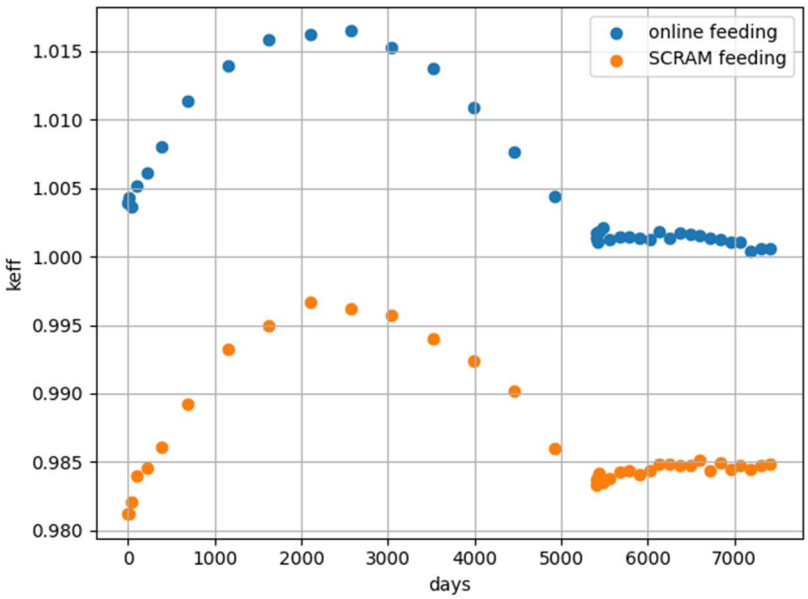

Fig. 55 keff changes during reactor operation with and without rods insertion

To compensate for mentioned maximum excess of reactivity - 1700 pcm, the temperature in the reactor core has to be elevated by more than 400 K. The temperature gradient in the reactor core is about 300 K. Taking into account some safety margins; it can be postulated that either lower

either upper-temperature limits will be exceeded. Secondly, as it has been shown, the reactor will be subcritical after about 5500 days which is about 15 years. DFR is intended to work for about 20 years.

For that reason, some solutions have to be delivered to control reactivity.

The reactor can be designed in such a way as to have minimum excess of reactivity at the beginning of life, and k_{eff} is going down with burnup. Then, to maintain criticality, feeding the reactor can be started at the very beginning of the reactor's lifetime.

Another option can be introducing control rods in the reactor as a reactivity control system.

What can also be made is to combine both methods. It gives better flexibility, and both methods can also be used as a shutdown safety system. The author decided to propose control rods in the reflector zone. Due to inlet and outlet regions below and over the reactor core, placing control rods in the reactor core is very challenging. Therefore, the reflector zone has been chosen.

Control rods have been collected into assemblies - each assembly has 19 control rods. Twenty-four assemblies have been placed into the reflector zone. The arrangement can be seen in Fig. 56. Detailed dimensions of the control rods and assemblies can be found in Fig. 57. Control rods are made of B_4C (90% enriched boron), helium gap and silicon carbide.

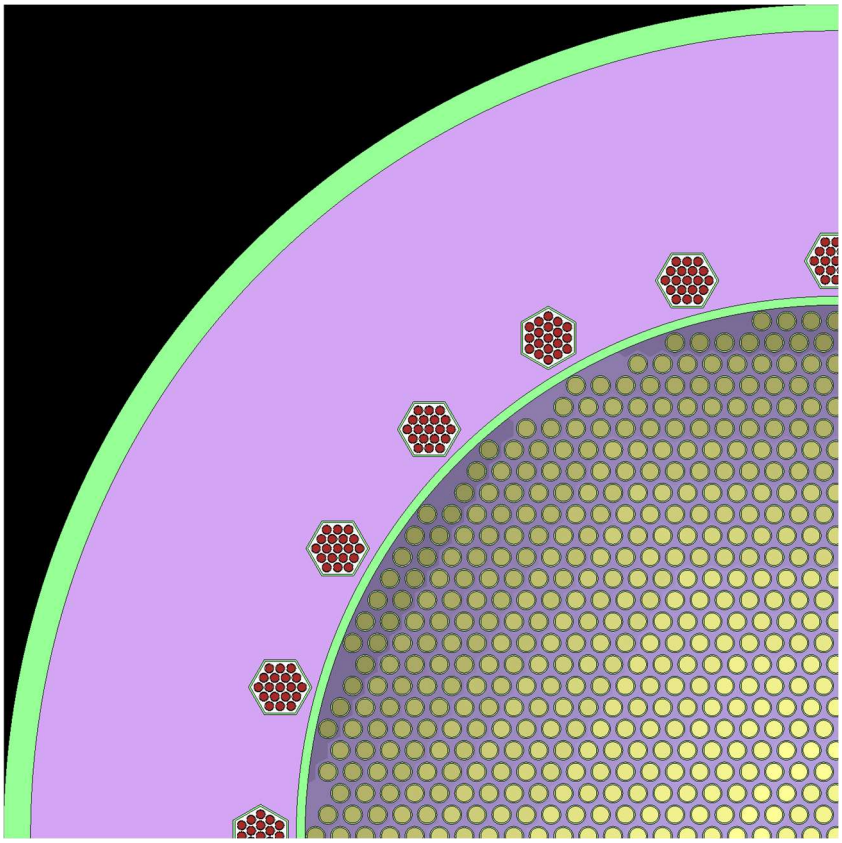

Fig. 56 Control rods in reflector zone - core horizontal cross-section

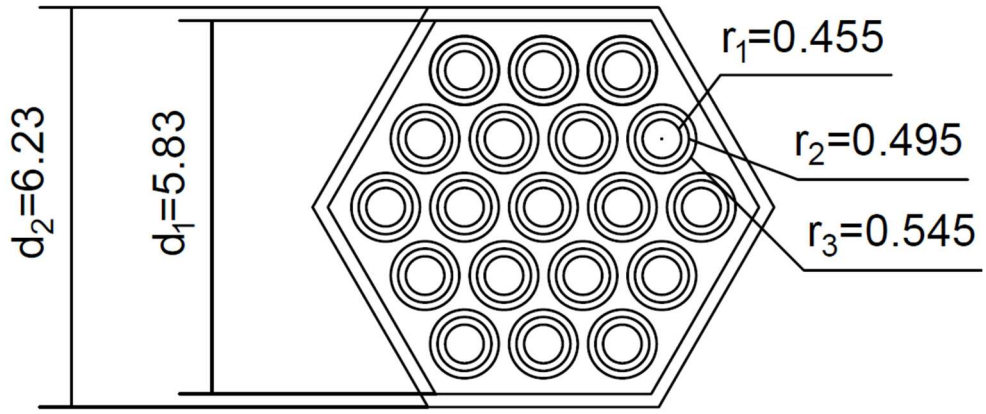

Fig. 57 Detailed geometry for control rods assembly

In Fig. 55, orange dots represent k_{eff} for specific burnup after full insertion of the assemblies with control rods - SCRAM. The reactor became subcritical for all the cases. However, a given reactivity margin is not high. Nevertheless, adding more control rods into the reflector zone is still possible. These calculations are mainly to illustrate that this solution can be sufficient.

In Table 24, neutronic data for DFR are presented. Most of them are taken from the created model in Serpent. Reactivity loss - ρ_0 and

precursors concentrations - C_i are calculated as an initial condition, based on equations (5) and (6), respectively.

Fig. 58 presents power profiles for BOL (Beginning Of Life) and EOL (End Of Life). Every point (blue or red dot) represents power generated in the specific fuel pipe. It can be seen that the power profile did not change during the whole lifetime (about 20 years). That is a feature of liquid, circulating fuel reactors. However, it looks different in solid fuel reactors. The neutron flux is never uniform in the reactor core. For that reason, in other regions, a different number of specific isotopes has been created. Also, in various assemblies and fuel rod's reaction rate of fission will be different. Therefore, the power profile changes significantly during reactor operation in solid fuel reactors. However, it is not the case for liquid, circulating fuel reactors. Fuel constantly flows through the reactor core, and isotopes in the fuel are practically uniformly distributed. Therefore, the power profile for those types of reactors is almost constant, as it is presented in Fig. 58.

Table 24 DFR neutronic data

Parameter	BOL	EOL	Unit
Neutron generation time	$2.36*10^{-7}$	$2.15*10^{-7}$	s
Reactivity loss ρ_0	319	180	pcm
Neutron density	$2.7*10^{9}$	$2.7*10^{9}$	$1/cm^3$
Precursor density			
C_1	$9.1*10^{13}$	$2.4*10^{13}$	$1/cm^3$
C_2	$2.2*10^{14}$	$9.4*10^{13}$	$1/cm^3$
C_3	$6.6*10^{13}$	$3.28*10^{13}$	$1/cm^3$
C_4	$8.0*10^{13}$	$5.1*10^{13}$	$1/cm^3$
C_5	$9.2*10^{12}$	$6.6*10^{12}$	$1/cm^3$
C_6	$5.4*10^{11}$	$2.54*10^{11}$	$1/cm^3$
Delayed neutron fraction			
β_1	$1.80*10^{-4}$	$1.80*10^{-4}$	-
β_2	$1.09*10^{-3}$	$7.05*10^{-4}$	-
β_3	$1.09*10^{-3}$	$6.18*10^{-4}$	-
β_4	$3.32*10^{-3}$	$1.83*10^{-3}$	-
B_5	$1.19*10^{-3}$	$7.16*10^{-4}$	-
B_6	$3.75*10^{-4}$	$1.8*10^{-4}$	-
Decay constant λ_1	0.0125	0.0125	1/s
Decay constant λ_2	0.0315	0.0305	1/s
Decay constant λ_3	0.111	0.111	1/s
Decay constant λ_4	0.325	0.328	1/s
Decay constant λ_5	1.34	1.32	1/s
Decay constant λ_6	9.14	9.55	1/s

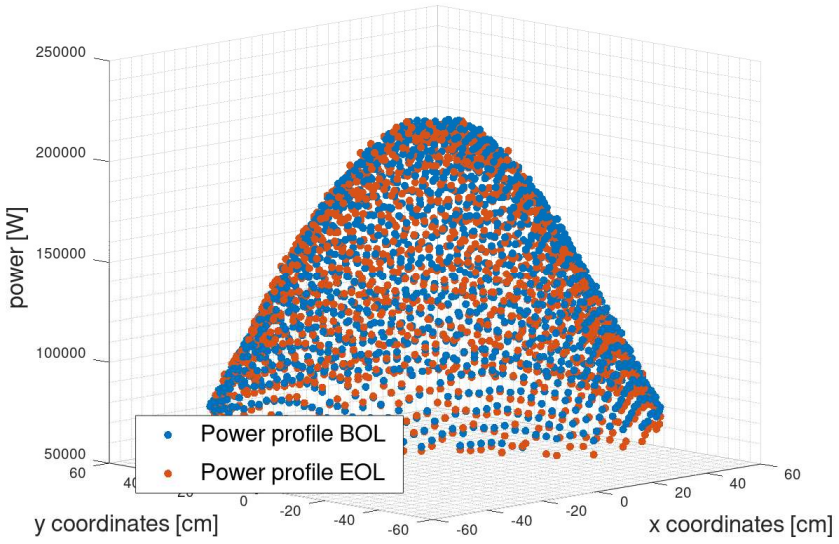

Fig. 58 DFR power profile for BOL and EOL

Power profile from Fig. 58, neutronic data from Table 24 and reactivity temperature coefficient from Table 22 (average values) are used for the neutronic solver created in the TRACE code, which is described in 4.2.

4.2 Transient simulation

In section 2.2 author describes the MSRE model created in the TRACE code. For DFR, a similar model has been created. Thus:

- TRACE code has been used
- A neutronic solver has been built based on the same set of equations (2)
- Sodium and lead-bismuth properties have been substituted with DFR fuel and coolant fluids
- The modified TRACE version has been compiled, and a new executable file has been created

The main difference between the MSRE model created and described in section 2.2, is the source of data. For example, in the case of MSRE, neutronic data have been taken from ORNL reports. In the case of DFR, all needed data are taken from the DFR model created in Serpent.

Some results of Serpent calculations have been presented in this Chapter. These results are used for TRACE model improvements.

4.2.1 Used materials

In the DFR model created in TRACE following materials have been used:

- Uranium-chromium eutectic as a liquid fuel
- Lead as a coolant
- Silicon carbide as a structural material

The properties of liquid lead have been taken from research [61].

There is a lot of research regarding the properties of liquid chromium and liquid uranium. However, data regarding liquid uranium-chromium properties are minimum. To overcome this obstacle, the author used the binary mixtures rule. In general, rules of mixtures are sets of equations useful for estimating different properties of mixed fluid. In the case of mixing two fluids, it can be called a binary rule of mixtures.

Different rules of mixtures for a specific property are collected in Table 25. Based on them, various thermophysical properties have been calculated as a function of temperature. Finally, results are collected and established together with lead properties in Table 26.

Table 25 Rule of mixtures for different thermophysical properties

Property	Equation
Surface tension [65]	$\sigma = y_A\sigma_A + y_B\sigma_B$ where σ – surface tension. y – mole fraction of the component of the mixture
Thermal conductivity [66]	$\lambda = w_A\lambda_A + w_B\lambda_B - (\lambda_B - \lambda_A)\left(1 - \sqrt{w_B}\right)w_B$ where λ – thermal conductivity. w – weight fraction of the component of the mixture
Specific heat [67]	$C = C_A w_A + C_B w_B$, where C – specific heat (29), w – weight fraction of the component of the mixture
Viscosity [68]	$ln\eta = y_A ln\eta_A + y_B ln\eta_B$, where ŋ – viscosity. y – mole fraction of the component of the mixture

Table 26 Thermophysical properties for fuel and coolant for DFR.

Reference pressure	1 bar		
	Unit	Fuel	Coolant [61]
Surface tension	$\frac{N}{m}$	$2.02 - 2.75 \times 10^{-4} \times$ T [59], [69]	$0.52 - 1.13 \times 10^{-4} \times$ T
Thermal conductivity	$\frac{W}{mK}$	20.1 [59], [70]	$9.2 + 0.011 \times$ T
Density	$\frac{kg}{m^3}$	$18835 - 1.95 \times$ T[59], [58]	$11367 - 1.19 \times$ T
Melting point	K	1133 [63]	600.5
Specific heat	$\frac{J}{kgK}$	235 [59], [58]	$175.1 - 0.05 \times$ T $+ 1.99 \times 10^{-5} \times T^2 - 2.1 \times 10^{-9} \times T^3 - 1.524 \times 10^6 \times T^{-2}$
Viscosity	Pa s	0.006 [59],[71]	$4.55 \times 10^{-4} e^{\frac{1069}{T}}$

For structural materials, silicon carbide has been used. Data for SiC used in the TRACE model are presented in Table 27.

Table 27 Properties of SiC - structural materials for DFR

Property	Unit	Value
Density	$\frac{kg}{m^3}$	3210
Heat capacity	$\frac{J}{kgK}$	690
Thermal conductivity	$\frac{W}{mK}$	$6.1 \times \frac{10^4}{T - 115}$

4.2.2 Hydraulic DFR model in the TRACE

The hydraulic model of the DFR created in TRACE can be seen in Fig. 59. Model consists of 2 loops: a fuel loop with chromium-eutectic and a coolant loop with lead. Twelve rings represent the reactor core with fuel pipes. Each ring is thermally coupled with the so-called “VESSEL” component, which represents lead in the reactor core. Below and over reactor core elements, upper and lower plena are placed, which represent inlet and outlet regions. Fuel and coolant pumps are modelled with so-called “FILL” and “BREAK” components, representing a system's boundary conditions.

Heat is generated in the fuel pipes, directly in the liquid fuel, by "FLUID POWER" components. Heat is transferred to the lead loop by heat structures and sinks out from the system in the secondary loop.

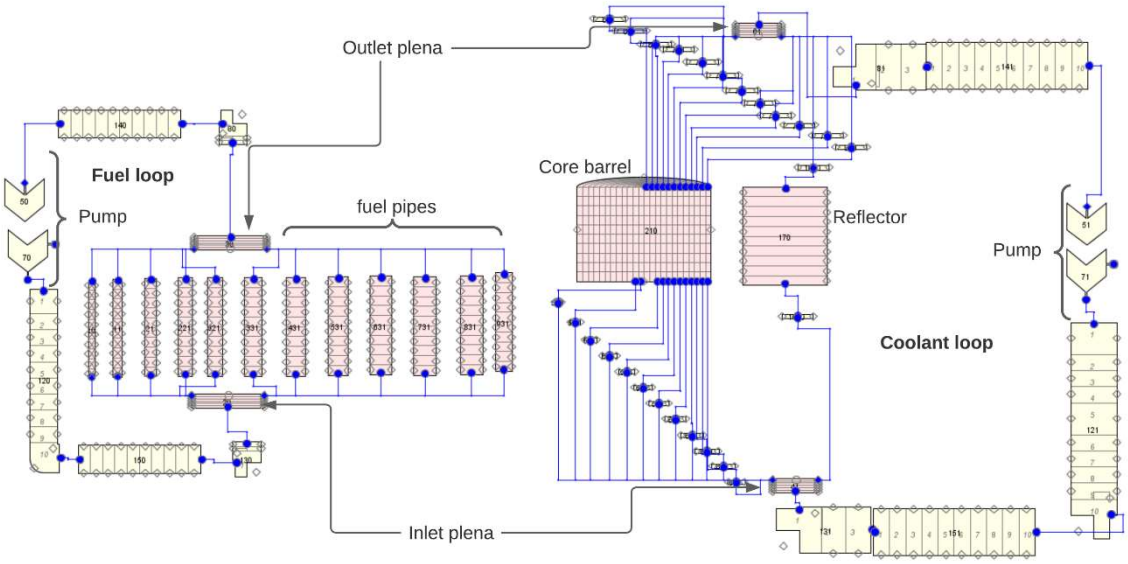

Fig. 59 Hydraulic DFR model in the TRACE

4.2.3 Neutronic solver

As was mentioned, a neutronic solver has been created similarly as it was done for the MSRE model. In addition, the solver has been built based on the presented previously forward Euler scheme. Neutronic data for this model has been taken from Table 24.

4.2.4 Nuclear importance

One of the variables in the set of equation (2) is reactivity $\rho(t)$: $\frac{dn(t)}{dt} = \frac{\rho(t)-\beta}{\Lambda} n(t) + \sum_{i=1}^{6} \lambda_i C_i$. This variable has several components, which can be represented by equation (8).

$$\rho = \rho_0 + \alpha_f\left(\overline{T}_f - \overline{T}_{f,0}\right) + \alpha_c\left(\overline{T}_c - \overline{T}_{c,0}\right) + \alpha_r\left(\overline{T}_r - \overline{T}_{r,0}\right) + \rho_{inserted} \qquad (8)$$

In equation (8), subscripts "0" denoted initial, steady-state conditions This equation has five components:

- Reactivity loss - ρ_0, it is the initial condition based on formula (5)
- Temperature reactivity feedback for fuel, coolant and reflector, based on reactivity temperature coefficient from Table 22, and temperature differences

- Inserted reactivity - it is reactivity added to the system to disturb the reactivity balance and see the behaviour of the system, for example, step reactivity insertion

The first and last components from the above list, reactivity loss and inserted reactivity, are pretty straightforward. However, temperature reactivity feedbacks are a bit more complex. Firstly, temperature change during transient is different for different radial and axial cells. Secondly, the same temperature change in other reactor places can affect reactivity with different impacts. Therefore, an additional calculation has been performed to consider the various impact of different cells in the model.

The DFR model in Serpent has been divided into 12 radial zones (from the inside to the outside) and 10 axial zones (from the bottom to the top). Radial and axial divisions are presented in Fig. 60 and Fig. 61, respectively.

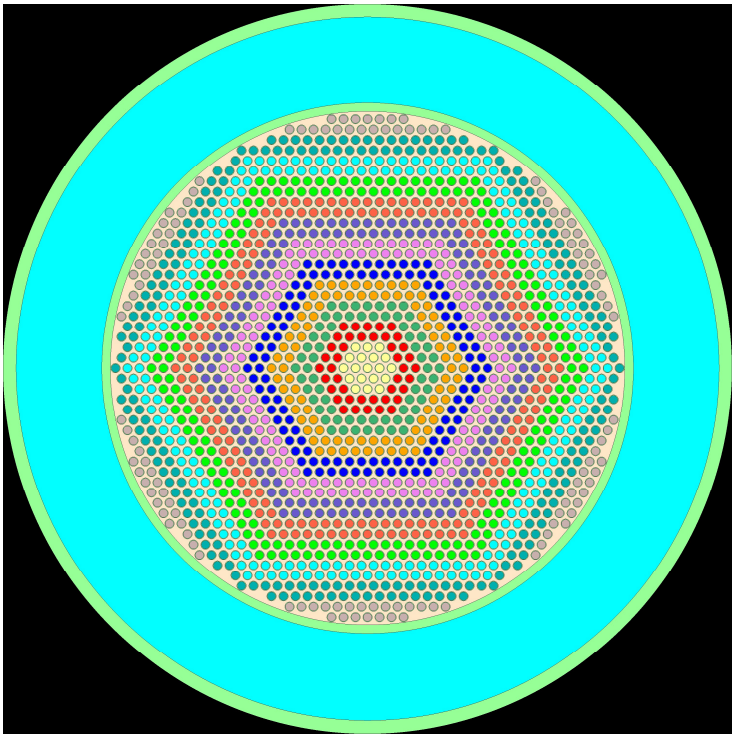

Fig. 60 DFR horizontal division in Serpent model

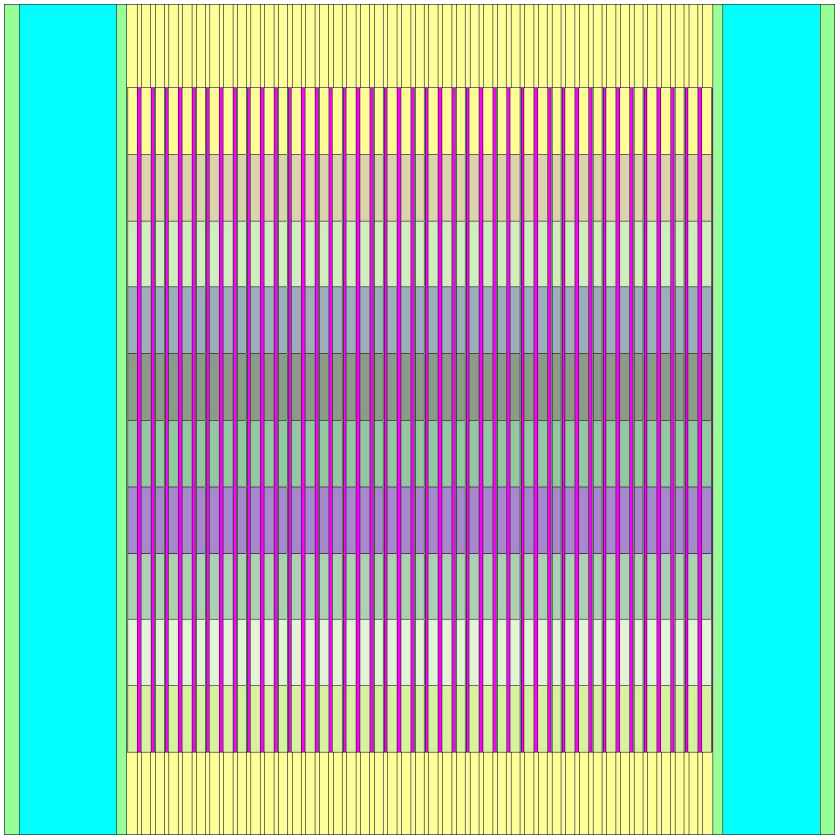

Fig. 61 DFR vertical division in Serpent model

To measure what is the impact of each radial and axial level following procedure has been implemented:

- Calculation with uniform fuel temperature in the core has been performed for temperatures equal to 1200 K.
- Ten separate calculations have been performed. For each calculation, different axial level has elevated fuel temperature. However, the rest axial levels had an unchanged temperature of 1200 K.
- Such temperature change in different axial positions affects the multiplication factor with other impacts.
- After calculations for all axial levels, results are normalized using formulas (9) and (10).
- The same scheme has been implemented for radial division.

$$w_{level} = \frac{\Delta k_l}{\sum \Delta k_l} \tag{9}$$

This procedure delivers so-called "nuclear-importance" weights for all radial and axial positions. Weights are presented in Table 28. It can be

seen that cells with lower weights have significant relative uncertainties, especially radial central cells. A similar procedure has been implemented for coolant. However, because it has a small temperature reactivity coefficient, the results were in the order of statistical uncertainty.

$$\Delta k_l = k_{ref} - k_l \tag{10}$$

Table 28 Nuclear importance for radial and axial levels in DFR

level	Radial weight, 10^{-3}	Axial weight, 10^{-3}
1	19 ± 6	55 ± 5
2	42 ± 7	78 ± 6
3	72 ± 7	99 ± 6
4	101 ± 7	132 ± 6
5	113 ± 7	136 ± 6
6	114 ± 7	136 ± 6
7	122 ± 7	132 ± 6
8	120 ± 7	99 ± 6
9	93 ± 7	078 ± 6
10	90 ± 7	55 ± 6
11	75 ± 7	
12	40 ± 7	

Axial divisions are symmetrical. Therefore, corresponding values were averaged. For example, values for levels 2 and 9 or 1 and 10 were averaged. It can be seen that axial levels from the middle part of the reactor core have more than three times greater weights than axial levels from the peripheral regions.

It looks a bit differently for radial divisions because different radial levels consist of different numbers of fuel pipes. It is why levels in the middle (radial levels 7 and 8) have the highest weights, higher even for levels in the centre of the core. For radial cases, weights are a function of neutron flux and the number of pipes at a specific level.

The presented weights in Table 28 are implemented in a neutronic solver created in TRACE. Therefore, instead of taking the arithmetic average of fuel temperature, the weighted average is used.

4.2.5 Power and temperature distribution - model

Often, if the user does not know the temperature distribution, a common assumption for a model in Serpent code is an isothermal

temperature for specific material. It means that particular material has the same uniform temperature in the system. Such assumptions can lead to significant discrepancies between results produced by the given model and reality. It is crucial, especially for systems with large temperature gradients and strong temperature reactivity coefficients.

A similar problem occurs in the TRACE code with power distribution in the core. To solve this problem, for both mentioned codes, the author incorporates python scripts to exchange power and temperature fields between codes. The Serpent needs temperature distribution, which can be delivered by TRACE code. On the other hand, TRACE needs power distribution which the Serpent code can give. The coupling scheme is presented in Fig. 62. The scheme usually converges after 4-5 runs. To converge the scheme, Serpent calculations should be run with good statistics to decrease statistical uncertainty. Otherwise, it can be a source of differences in power profile, and the scheme will not be converged.

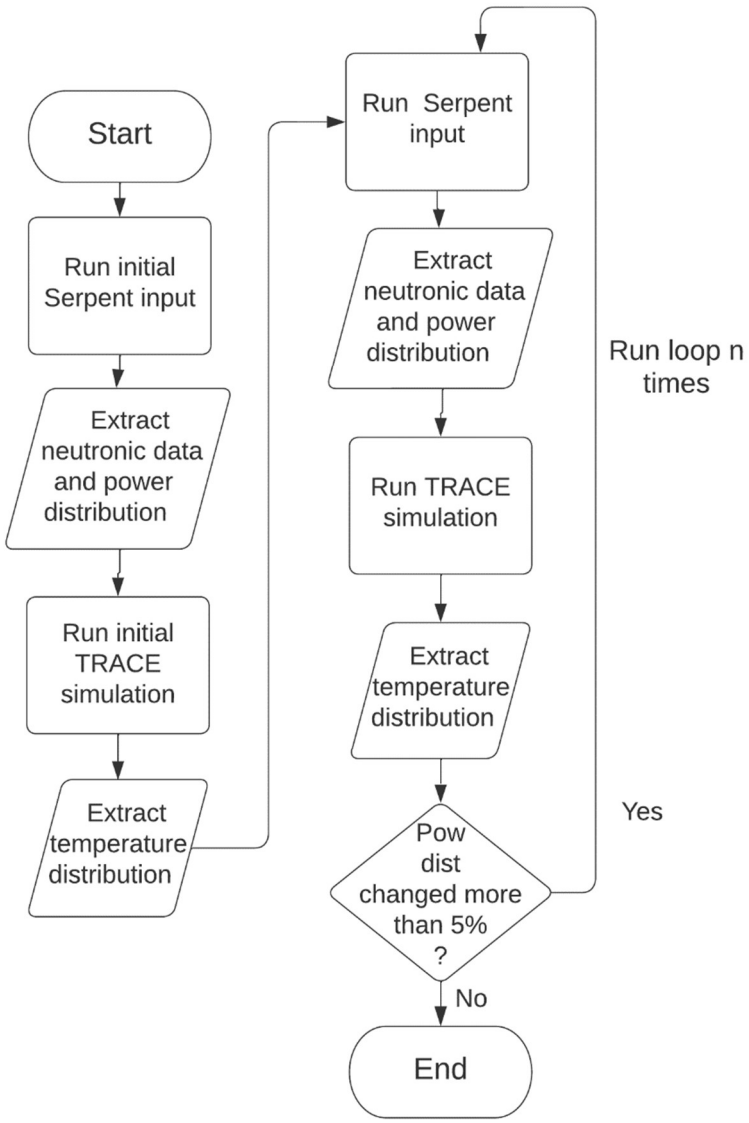

Fig. 62 Coupling scheme between TRACE and Serpent codes

4.3 Optimization DFR conditions

Nuclear reactors, heat exchangers and whole nuclear power plants are multidimensional optimization problems. The main parameters which are essential in such systems are:

- Safety
- Efficiency
- Costs

In this section, several criteria which are important from the point of view of mentioned parameters have been introduced.

4.3.1 Temperature limits

The temperature of the materials in a nuclear reactor is one of the most crucial safety issues. Temperatures of used liquids in DFR must be sufficiently far from the solidification and boiling point. The high temperature of liquid metals significantly impacts erosion and corrosion phenomena. From the point of view of the efficiency of the system, coolant temperature is a crucial parameter.

From the point of view of the proposed structural material for DFR - SiC, the temperature should be lower than 1650 ^{0}C. Based on previous research[64], silicon carbide, subjected to stress above 1650 ^{0}C, is no longer in the elastic range and starts to be plastic. It means, above mentioned temperature, SiC, does not go back to its previous dimension after the stress is taken out.

Boiling temperatures for uranium, chromium and lead are, respectively: 4404 K, 2945 K and 2022 K. Therefore, the temperature limit in the reactor from the upper side is SiC elasticity limitation, which is expressed, in Kelvins, by formula (11).

$$T_{max} = 1650 + 273 - upper\ margin \tag{11}$$

Where “upper margin” is the safety margin to ensure that this crucial point is never exceeded for fuel and coolant.

On the other side, fuel and coolant must always be liquid in the reactor core. Therefore, any of these metals should not solidify during reactor operation.

The solidification point of uranium-chromium eutectic is about 1133 K. Solidification point of lead is about 600 K. Minimum temperature for fuel and coolant can be expressed by formulas (12) and (13).

$$T_{fuel,min} = 1133 + lower\_margin \tag{12}$$

Similarly to the upper-temperature limit, the lower limit also has some safety margin denoted as “lower margin”.

$$T_{coolant,max} = 600 + lower\_margin \tag{13}$$

4.3.2 Neutronic safety

One of the most crucial safety parameters is a fraction of delayed neutrons. Delayed neutrons are essential from a safety point of view. Without them, operating current nuclear reactors would be extremely hard or impossible. Delayed neutrons act like a buffer for reactivity

changes and prevent the reactor from changing power rapidly. If the reactivity insertion is too high, it can make the reactor critical on the prompt neutrons. Such an event is called a reactivity accident. This accident occurred in 1986 in Chornobyl due to the wrong reactor design.

During reactor operation fraction of delayed neutrons change with burnup. U-235 content is decreasing during reactor operation, while Pu-239 content is increasing. Different isotopes produce different fractions of delayed neutron precursors, thus different fractions of delayed neutrons. A comparison of U-235 and Pu-239 is presented in Table 29, based on publication [53].

Table 29 Delayed neutrons fractions for U-235 and Pu-239 in fast and thermal systems [53]

Isotope	Beta fraction for thermal system	Beta fraction for fast system
U-235	$\beta = 0.0064$	$\beta = 0.0067$
Pu-239	$\beta = 0.0020$	$\beta = 0.0022$

As is presented in Table 29, a fraction of delayed neutrons strongly depends on the isotope and slightly depends on the neutron's energy. For Pu-239, the delayed neutron fraction is about three times smaller than for U-235. That is why delayed neutron fraction is a function of actinides composition. While actinides composition strongly depends on burnup, initial composition and neutrons energy spectrum. A fraction of delayed neutrons decreases with burnup for reactors with fresh uranium fuel.

However, for liquid, circulating fuel reactors, there is an additional drop of delayed neutrons due to fuel circulation and decay of DNP outside the reactor core. This effect was described in more detail in section 2.2.3. The relation between reactivity for static fuel and circulating fuel is presented by formula (14).

$$\beta_{circulating} = \beta_{static} - \rho_0 \tag{14}$$

Based on equation (14), the real value of available delayed neutrons in the system is $\beta_{circulating}$. While β_{static} is delayed neutron fraction for the velocity of the fluid equal to 0. The ρ_0 is so-called reactivity loss and it has been introduced in equation (5).

4.3.3 Velocity limits

As well as the temperature, as the velocity of the fluid, has a strong impact on erosion and corrosion problems. Therefore, the velocity at high

temperatures should stay relatively low to avoid this destructive phenomenon. In another research [28] related to DFR technology, velocity for fuel and coolant has been calculated. It has been decided not to exceed velocities from the analysis [28]. Mentioned velocity limits are collected in Table 30.

Table 30 Velocities limits, based on research [28]

Region	Velocity, m/s
Inlet/outlet fuel	3
Inlet/outlet coolant	5
Core fuel	0.52
Core coolant	1.35

4.3.4 Loops dimensions

Another type of parameter is the dimensions of the coolant and fuel loops. The coolant loop should be long enough to place the heat exchanger (steam-lead for the Rankine cycle, industrial heat, or helium-lead for the Brayton cycle). On the other hand, it should not be too long because it will increase the costs and make the whole system react slower to the load changes.

The fuel loop should be big enough to allow fuel to be a homogenized mixture (or close to such a state). On the other hand, it should not be too big because it will increase the amount of DNP, which will decay outside the reactor core, thus decreasing the reactor's safety. A large external fuel loop will also increase the amount of fuel for initial loading, which will affect the costs.

Proposed dimensions for both: coolant and fuel loops are presented in Table 31.

Table 31 Proposed dimensions for coolant and fuel loops

	Coolant loop	Fuel loop
Length of the external loop	9 m	5.9 m
Cross section of the external loop	0.273 m^2	0.5 m^2
Cross section of inlet/outlet region	0.6 m^2	0.677 m^2
Cross section of the core region	0.517 m^2	0.458 m^2

4.3.5 Optimal parameters

Taking into account all considerations established in sections 4.3.1 - 4.3.4, a few criteria for choosing optimal conditions for DFR has been proposed. The selected criteria are as follows:

- The temperature difference between the maximum and minimum fuel temperature in the fuel loop should be less than 300 K
- The temperature difference between the maximum and minimum coolant temperature in the coolant loop should be less than 500 K
- The maximum coolant velocity should be lower than the value from Table 30
- The maximum fuel velocity should be lower than the value from Table 30
- ρ_0 - reactivity loss; should be lower than $\beta_{circulating}$ - parameters based on equation (14)

Table 30 does not contain information about velocities in the external parts of the loops (outside reactor core and inlet/outlet regions). Therefore, it has been decided to limit the maximum velocity of an outer part not to exceed limits for the reactor core. Thus, they are 0.52 m/s and 1.35 m/s for fuel and coolant, respectively.

The difference between the lowest and highest allowable temperature for coolant is about 500 K higher than for fuel. It is why the temperature gradient for coolant is 200 K broader than for fuel (500 K and 300 K, respectively).

In case of a sudden blockage of the primary system, fuel velocity will drop from a specific value to 0. It will insert a certain amount of reactivity because DNP suddenly will stop going out from the core.

Based on the article [26] MHD pump is proposed for DFR. However, due to such a high working temperature, there is also an idea to rely only on natural convection. In the case of MHD, there are no moving elements in the fuel loop, and fluid is pushed only by the electromagnetic field. Thus, even when the pump fails, the fuel will not be stopped instantaneously due to certain inertia. In the case of natural circulation, there is no MHD pump. Thus, no such scenario will occur.

In both cases, the blockage of the fuel loop by the fuel itself is possible. If some part of the fuel is in a solid state (fission products have very different melting points, and many different compounds can be created in

such conditions), it could make a partial or a total stuck in the fuel loop. To estimate the occurrence of such an event, a lot of experiments and chemical simulations must be made. However, making a conservative assumption that such blockage will occur suddenly and will momentarily decrease fuel velocity to zero, ρ_0 - reactivity loss should be lower than $\beta_{circulating}$.

The results of the optimization are presented in Chapter 5.

Chapter 5 DFR Simulations

In this Chapter, the results of created models for DFR have been presented.

5.1 Results of the optimization

In section 4.3.5, optimization criteria have been proposed. Parameters which affect chosen criteria are fuel and coolant flow rates. Several different runs have been performed with different coolant and fuel flow rates. Results are presented in Table 32.

It should be noted that the velocities in Table 32 are not average values but maximum values. From the point of view of materials, maximum velocity is essential, especially for erosion and corrosion problems. The maximum velocities values occur for places where the temperature was the highest. In the reactor core, this place is at the very central radius region at the top of the reactor core.

In Fig. 63, the fuel temperature distribution in the reactor core has been presented. Fuel temperature in the core has an-uniform radial distribution. It is a consequence of the lack of burnable poison in the system and the specific power profile presented in Fig. 58. Fuel temperature in the central radial region (radial level 1) and at the top (axial level 10) is the highest. The gradient temperature in Fig. 63 corresponds to the gradient temperature in Table 32.

In Fig. 64, the coolant temperature distribution in the reactor core has been presented. Overall, the relative temperature differences of the coolant look similar to the fuel temperature distribution. However, absolute values between fuel and coolant are shifted by about 200-250 K.

The total gradient of coolant distribution does not correspond to the value from Table 32. In the inlet region, cold coolant takes heat from the hot fuel and increases its temperature. In the core region, the coolant temperature is still increasing. In the outlet region, the coolant temperature is still rising, while fuel will be colder. That is why the coolant temperature gradient from Table 32 does not correspond to the temperature gradient from Fig. 64. Coolant temperature gradient from Table 32, corresponds to the total gradient in the whole system, while Fig. 64 presents temperature distribution only in the core.

It can be seen that cases number 1 and 2, in Table 32, exceed the criterion regarding fuel temperature gradient. Cases 3, 4 and 5 fulfil this criterion. However, case 5 exceeds velocity limits in the external loop.

Thus, from the given cases, only cases 3 and 4 meet all the conditions. Case 3 is very close to the fuel gradient temperature limitation; it has 296 K, while the limit is 300 K. Case 4 is close to the outer loop velocity limit; it has 0.51 m/s, while the limitation is 0.52 m/s. Therefore, it can be postulated that, based on chosen criteria, the allowable fuel flowrate is in the range from 2200 kg/s to 2500 kg/s (for a given coolant flowrate, 5000 kg/s and loops dimensions proposed in Table 31). From established cases, case 4 has been chosen as the most optimal because it has ΔT for fuel smaller by 20 K.

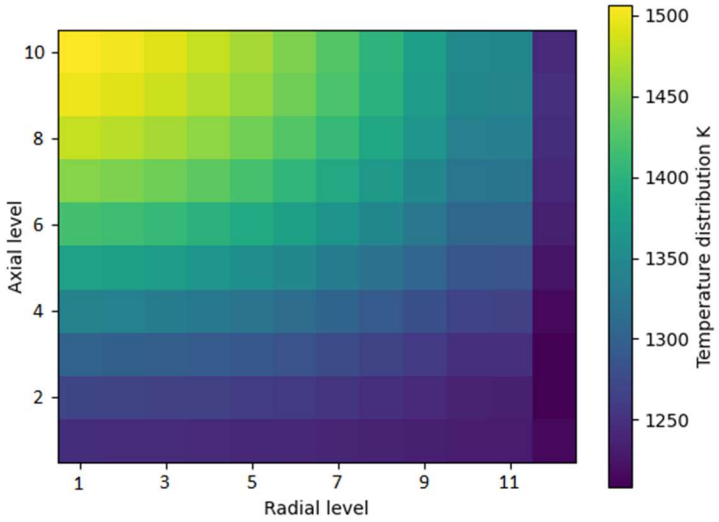

Fig. 63 Fuel temperature distribution in the DFR core

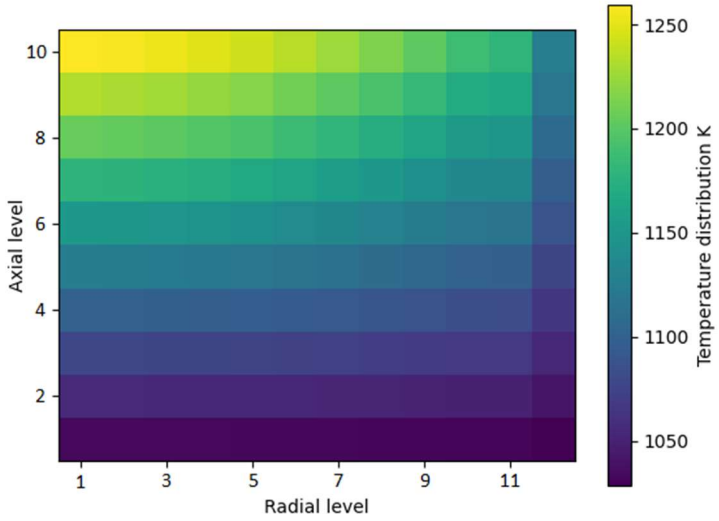

Fig. 64 Coolant temperature distribution in the DFR core

Table 32 Optimization criteria for different fuel flowrates

Case number		1	2	3	4	5
$\dot{m}_{fuel}$ kg/s		1500	2000	2200	2500	3000
$\dot{m}_{coolant}$ kg/s		5000	5000	5000	5000	5000
I/O region $v_{coolant}$ m/s		1.84	1.84	1.84	1.84	1.84
Core $v_{coolant}$ m/s		0.86	0.86	0.86	0.86	0.86
Loop $v_{coolant}$ m/s		0.84	0.84	0.84	0.84	0.84
I/O region v_{fuel} m/s		0.14	0.18	0.2	0.23	0.28
Core v_{fuel} m/s		0.33	0.38	0.4	0.43	0.48
Loop v_{fuel} m/s		0.31	0.41	0.46	0.51	0.62
fuel ΔT		352	310	296	276	251
coolant ΔT		431	431	431	431	431
BOL	ρ_0 pcm	290	313	319	328	340
	β_{circ} pcm	459	436	430	421	409
EOL	ρ_0 pcm	164	176	180	184	190
	β_{circ} pcm	250	238	234	229	223

5.2 Transient simulations

In this section, several different transient scenarios have been established.

5.2.1 Reactivity step insertion

Step change means that provided change is momentary. Thus, such change can be described by formula (15). Within one timestep, inserted reactivity changed from 0 to a certain level (in the presented example 100 pcm).

$$\begin{aligned} &for\ t < t_n, \rho_{inserted} = 0, \\ &for\ t \geq t_{n+h}\ \rho_{inserted} = 100\ pcm \end{aligned} \tag{15}$$

Several different reactivity step insertions have been simulated. Three reactivity insertion with positive values: 40 pcm, 70 pcm, 100 pcm and three negative reactivity step insertion values: -40 pcm, -70 pcm, and -100 pcm has been performed. To account for changes in the delayed neutrons fraction with burnup, calculations have been done for BOL and EOL.

Fig. 65 and Fig. 66 present power changes after positive reactivity insertion for BOL and EOL, respectively. Just after insertion, power is

peaking very strongly. Due to negative temperature feedback, power is decreased very rapidly within a few seconds. Between the third second and 10th second, power reached a plateau - inserted reactivity is in balance with the reactivity feedback. However, after about 10 seconds, the initially heated fuel returns to the reactor core. Due to the negative fuel reactivity coefficient, overheated fuel delivers negative reactivity, and power decreases. We can see that power oscillations are going lower and lower with time. After about 50 seconds, the power is close to being in balance. It can be seen that power changes for BOL and EOL look very similar. The main differences are the absolute value. Due to the lower content of U-235 and higher content of Pu-239, the total fraction of delayed neutrons is lower for EOL than for BOL. Therefore, power peaks after reactivity insertion are greater.

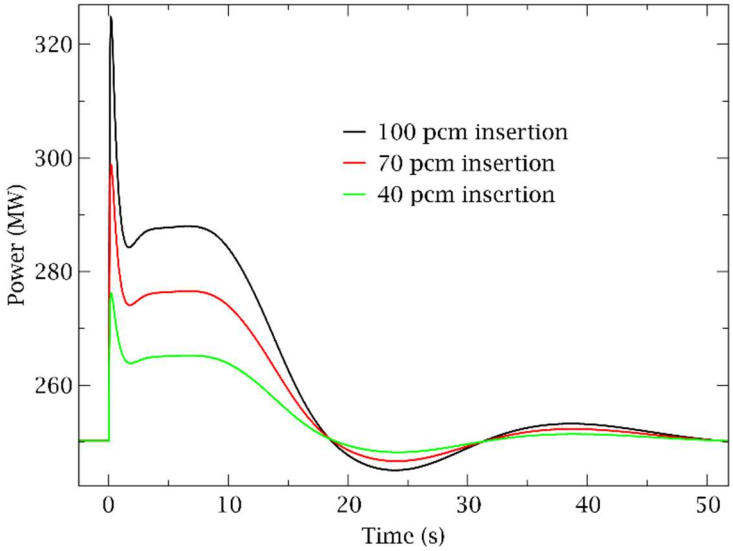

Fig. 65 DFR Power changes after step positive reactivity injection for BOL

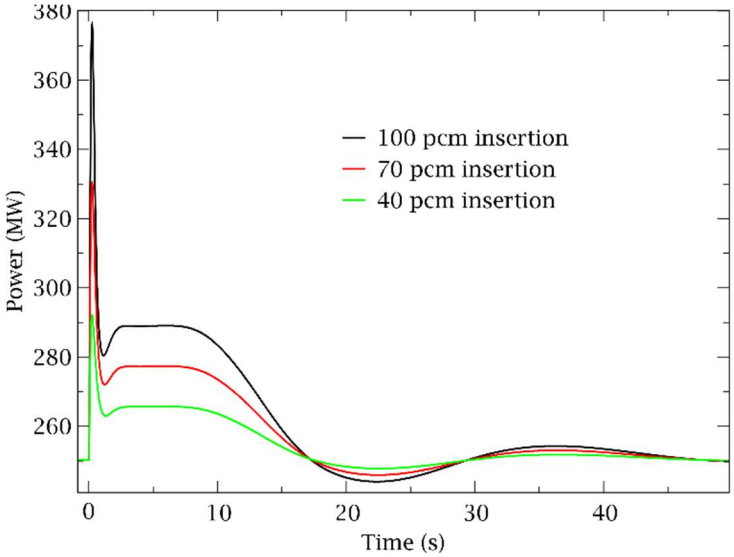

Fig. 66 DFR Power changes after step positive reactivity injection for EOL

Similar scenarios have been presented in Fig. 67 and Fig. 68. However, negative reactivity has been inserted instead of positive reactivity. Differences between positive and negative reactivity insertion are mainly absolute values. The behaviour is very similar but, of course, the opposite. Thus, power is dropping dramatically. Then, due to reactivity feedback, the power is partially recovered. Then, power is almost stable for several seconds (plateau region). After about 10 seconds, cold fuel re-enters the reactor core and provides positive reactivity, increasing power. After about 50-60 seconds, reactor power is stable and has a nominal value of 250 MW.

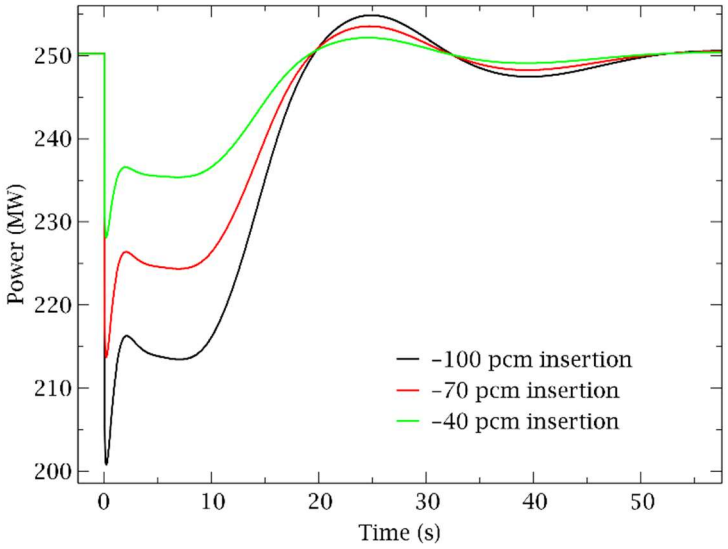

Fig. 67 DFR Power changes after step negative reactivity injection for BOL

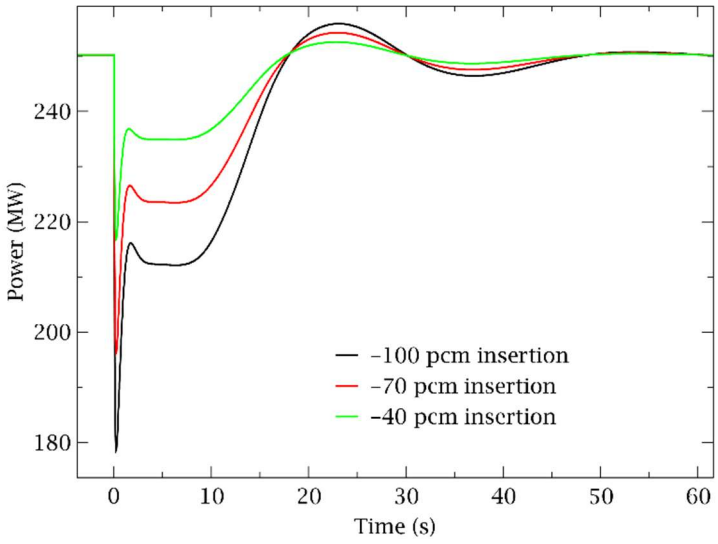

Fig. 68 DFR Power changes after step negative reactivity injection for EOL

In the case of positive reactivity insertion, inserted reactivity is balanced by fuel temperature rise. For negative reactivity insertion, inserted reactivity is balanced by a fuel temperature drop. Both scenarios can be potentially dangerous from the safety point of view due to temperature materials limitations.

In the case of positive reactivity insertion, maximum SiC temperature can be a safety issue. On the other hand, in case of negative reactivity insertion, minimum fuel temperature can be a safety issue.

Fig. 69 presents maximum fuel temperature changes for positive reactivity insertion. It presents two different burnup cases (BOL and EOL) and three different amounts of inserted reactivity. Temperature is a product of heat balance. As was mentioned, power peaks for EOL are stronger than for BOL. Therefore, in the case of temperature peaks situation is similar. It can be seen that the peak temperature is about 55 K (for 100 pcm) from the initial temperature. After about 50-60 seconds, the temperature reached a new stable level.

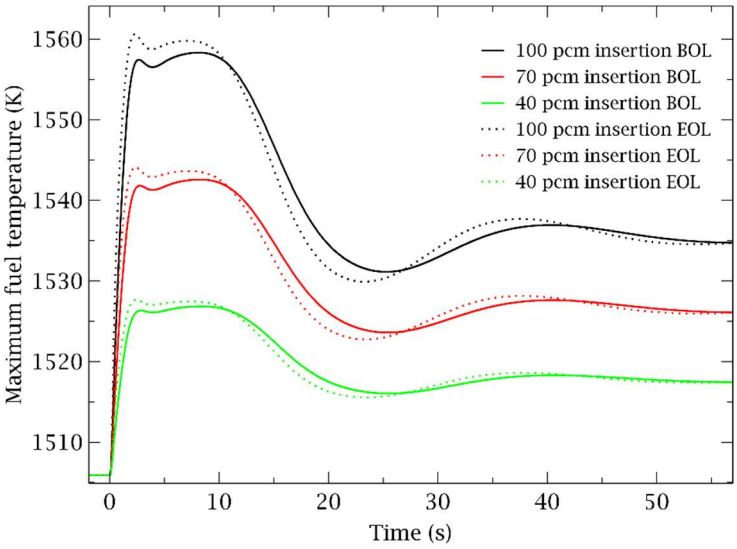

Fig. 69 Maximum fuel temperature after positive step reactivity injection in DFR

Fig. 70 presents minimum fuel temperature changes for negative reactivity insertion. At peak, for -100 pcm insertion, the temperature dropped about 30-35 K.

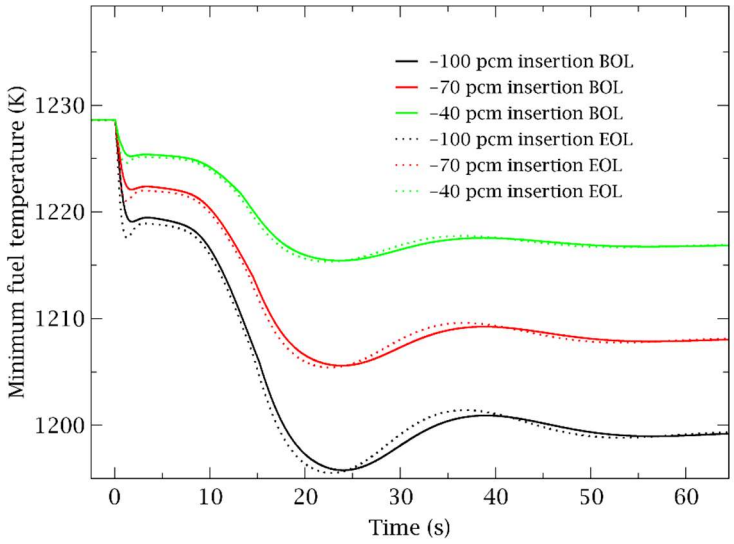

Fig. 70 Minimum fuel temperature after negative step reactivity injection in DFR

For both types of reactivity insertion (positive and negative), reactor power returned to a stable, nominal level after about 50-60 seconds. Temperature rise and drop were far from the temperature limits of the materials for all presented cases.

5.2.2 Ramp reactivity insertion

In this section, results for ramp reactivity insertion have been presented. Three different reactivity rates have been taken into consideration: 10 pcm/s, 7 pcm/s and 4 pcm/s. Time of the ramp in 20 seconds. Taking

account different reactivity rates and time of insertion, the total inserted reactivity is 200 pcm, 140 pcm and 80 pcm for corresponding rates. Inserted reactivity changes are presented in Fig. 71.

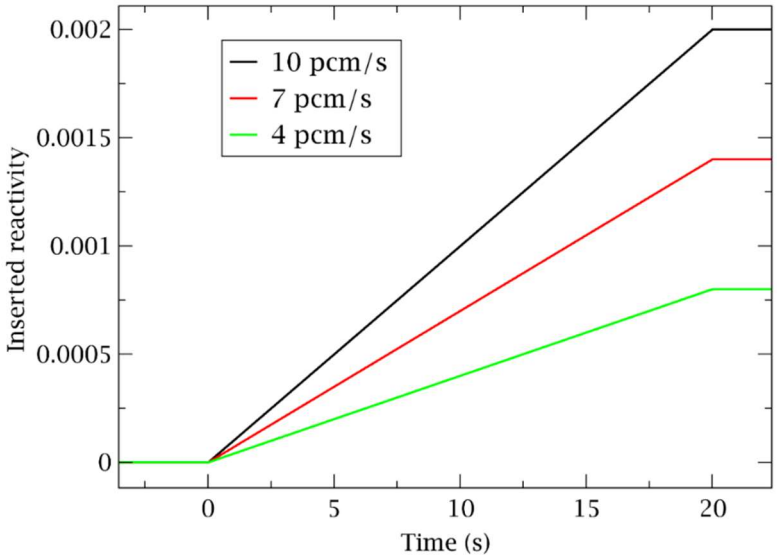

Fig. 71 Ramp reactivity injected into the system

In Fig. 72, power changes after ramp positive reactivity insertion for BOL and EOL have been presented. It can be seen that, as for step insertion, power changes are more dynamic for EOL than BOL. However, the differences are small if compared to the step insertion. Power peaks value due to ramp reactivity insertion in Fig. 72 are much smaller than power peaks for step reactivity insertion from Fig. 65 and Fig. 66. For ramp reactivity, for both cases: BOL and EOL, it is about 305 MW for the most extreme case - 10 pcm/s. For a reactivity step change, power peaks are about 325 MW and 380 for BOL and EOL, respectively. For ramp reactivity cases, after about 70 seconds, the reactor power is stable are reached the value from before reactivity insertion - 250 MW.

In Fig. 73, the maximum fuel temperature is presented. As the power changes are similar, so do the temperature changes. For example, for the most severe ramp reactivity insertion case - 10 pcm/s, reached about 1595 K in the peak. After about 70 seconds, the temperature dropped to about 1565 K for both BOL and EOL.

In Fig. 74, power changes after negative ramp reactivity insertion have been presented. The reactivity rates have the same absolute values, but they are negative: -10 pcm/s, -7 pcm/s, and -4 pcm/s. In Fig. 75, the minimum fuel temperature after reactivity insertion has been presented. Conclusions for negative ramp reactivity insertion are similar to the positive ramp reactivity, but there are some differences.

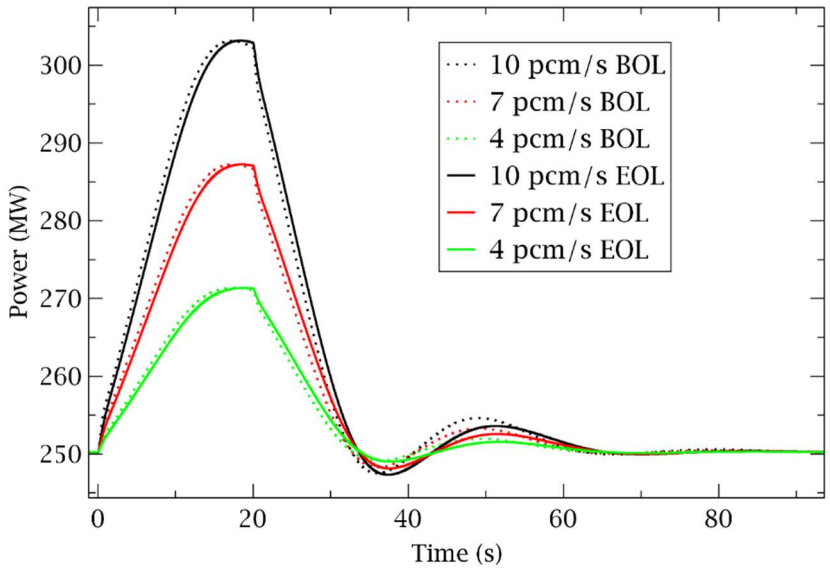

Fig. 72 DFR power changes after ramp positive reactivity injection

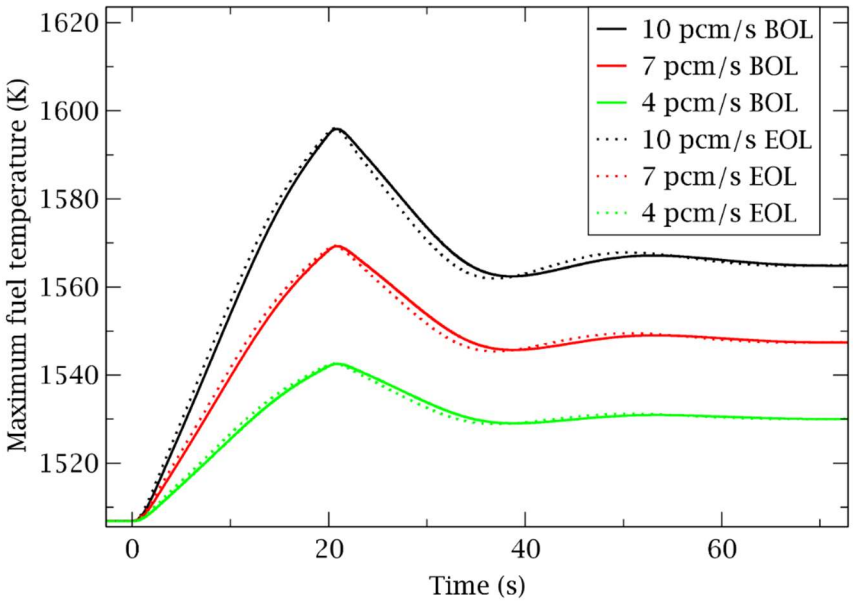

Fig. 73 Maximum fuel temperature after ramp positive reactivity injection in DFR

Power variations for BOL and EOL are very similar. However, the power drop for the ramp case is not as sharp as for the step case. The absolute value of the decline for the ramp case is about 195 MW for the most severe case for both BOL and EOL. For the step case, it is about 200 MW for BOL and about 180 MW for EOL. Therefore, for BOL, the step insertion power drop is smaller than the ramp insertion. However, for the most severe case, the step insertion is 100 pcm, while ramp reactivity is 200 pcm.

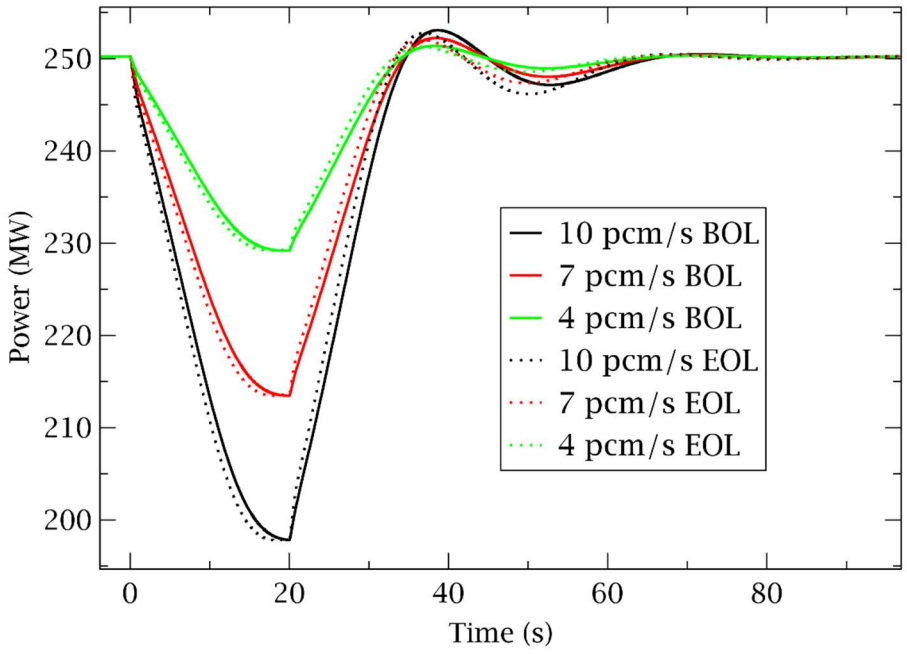

Fig. 74 DFR power changes after ramp negative reactivity injection

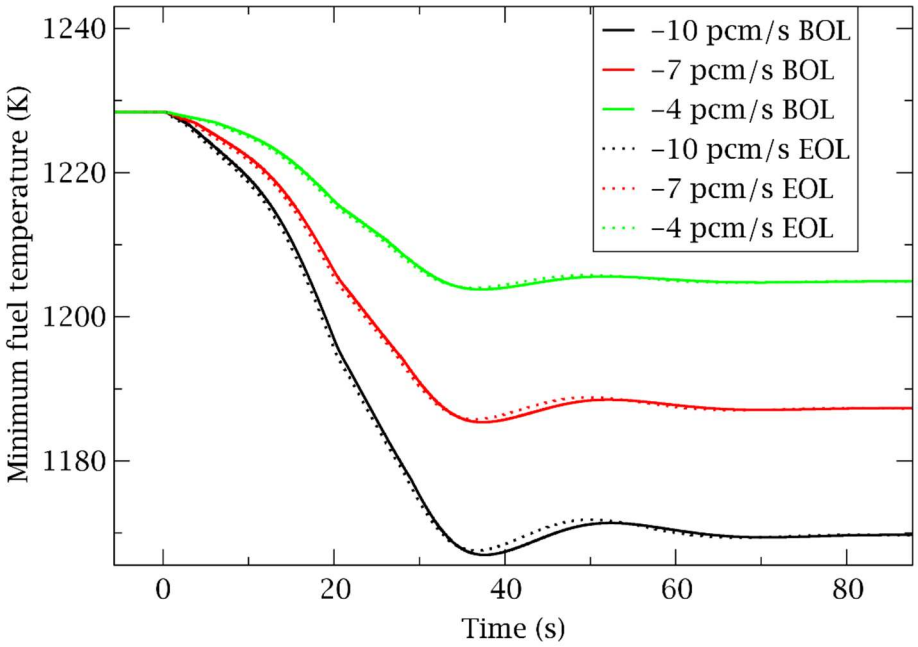

Fig. 75 Minimum fuel temperature after ramp negative reactivity injection in DFR

5.2.3 Heat sink efficiency step change

In this section, results for step heat sink efficiency have been presented. There are two scenarios for increasing heat sink and two for decreasing heat sink efficiency by 20% and 40%. In absolute values, heat sink power is 300 MW and 350 MW for heat sink increase cases and 200 MW and 150 MW for heat sink decrease cases. The presented results are for EOL because it is a more severe scenario than BOL.

In Fig. 76, power variation after the heat sink step efficiency changed has been presented. It can be seen that the system follows the load. After about 70 seconds, a new stable power level is established.

In the first 5 seconds, power changed counter-intuitive. In case when the heat sink is increased by 40%, power drops a little within the first 5 seconds. After increasing the heat sink efficiency, the coolant temperature goes down. Fuel and coolant flow rates are fixed for all the simulations. Due to the negative thermal expansion coefficient of the coolant, when the coolant temperature decreases, coolant velocity drops as well. Due to the lower velocity of the coolant, heat from the fuel loop transfers to the coolant less effectively, which means fuel temperature increases. Then, due to the negative temperature coefficient, reactor power slightly drops.

This situation changed when the cooled coolant started to enter the reactor core. As a result, fuel temperature goes down. Therefore, reactor power starts to increase as expected.

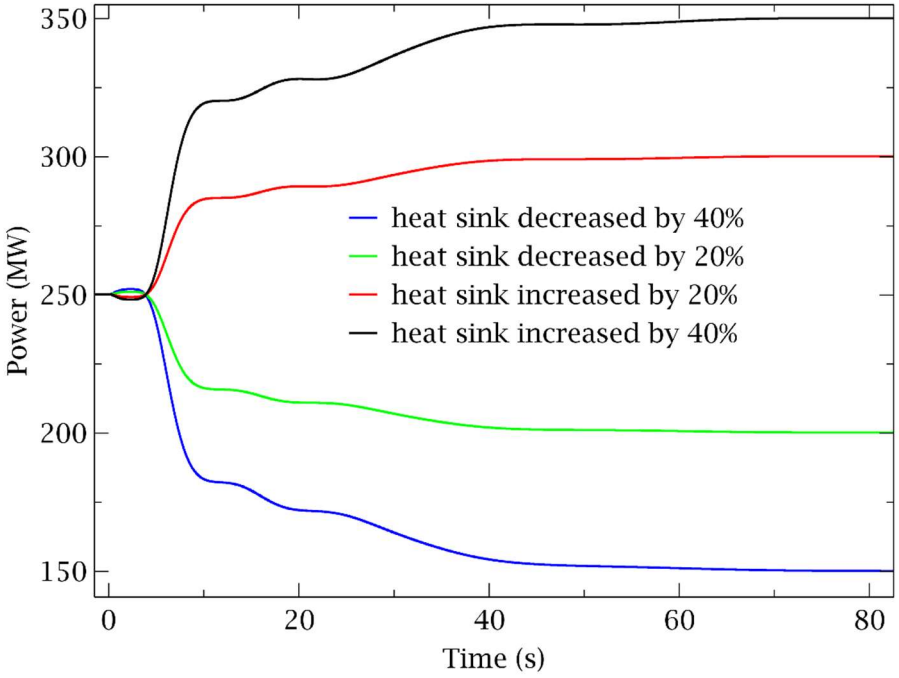

Fig. 76 DFR power changes after a step change in heat sink efficiency

Fig. 77 presents the maximum fuel temperature after the step change in heat sink efficiency. The temperature field is a function of the power field. Thus, temperature changes are similar to power changes. For the most severe scenario (heat sink efficiency increased by 40%) temperature rise to about 1550 K.

In Fig. 78, the minimum fuel temperature has been presented. The most severe scenario (from the point of view of minimum temperature) is also the case, with heat sink efficiency increased by 40%. During heat sink

efficiency changes, flow rates for fuel and coolant are fixed. Therefore, if the higher power is taken from the reactor core, the fuel has a negative temperature coefficient, and the fuel flow rate is not changed, the temperature gradient will be increased. Therefore, the maximum fuel temperature rises by about 45 K, and the minimum temperature drops by about 55 K.

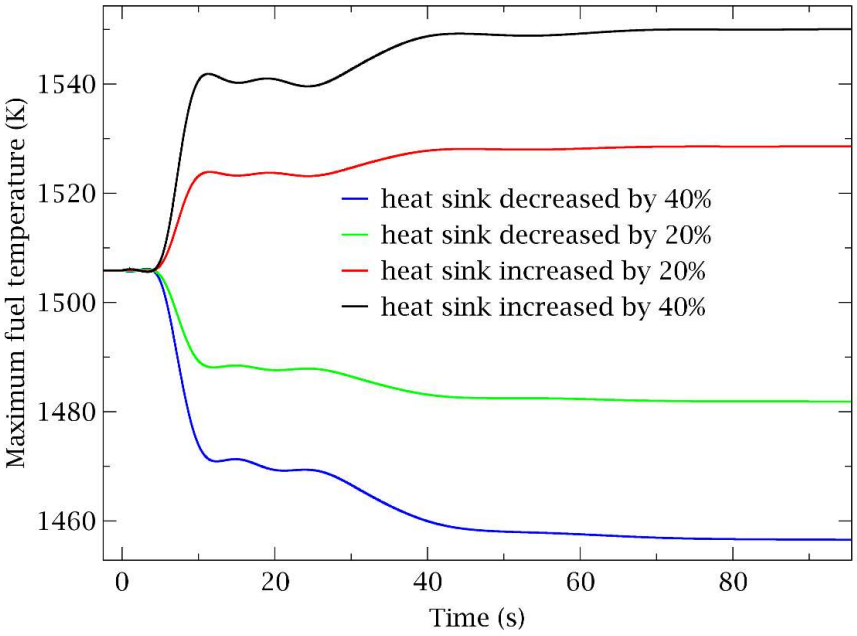

Fig. 77 DFR maximum fuel temperature variation after a step change in heat sink efficiency

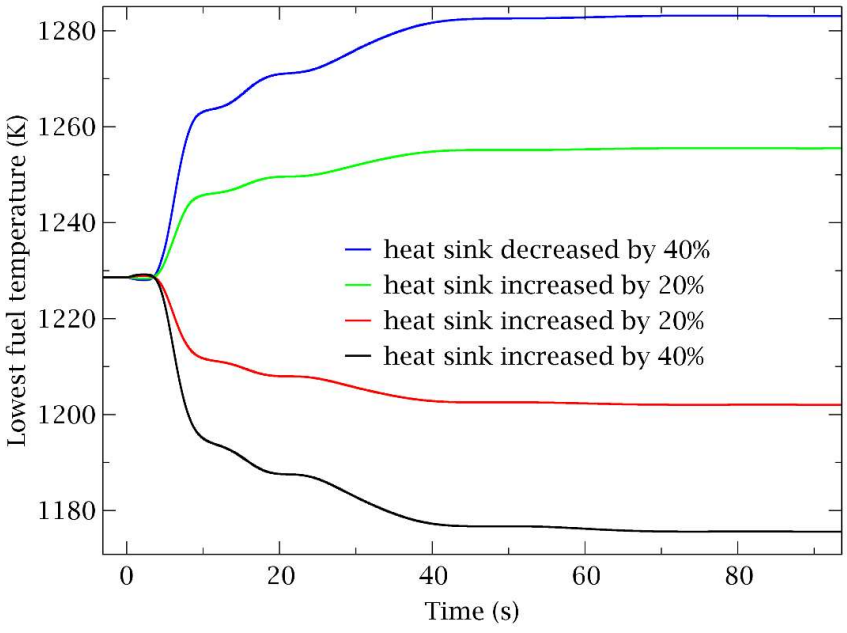

Fig. 78 DFR minimum fuel temperature variation after a step change in heat sink efficiency

Fig. 79 presents the maximum coolant temperature change after a step change in heat sink efficiency. It can be seen that for coolant situation is different than for fuel. In case of higher heat sink efficiency, the coolant will be cooled down to a lower temperature. In the first 7 seconds, a counter-intuitive temperature change was observed. A temperature drop can be expected for a scenario with increased heat sink efficiency. However, the presented temperature changes represent coolant temperature in the reactor core. The flow rate of coolant is fixed. After cooling down the coolant, velocity also drops. Therefore, coolant flows slower through the reactor core. Spending more time in the reactor leads to increased temperature of the coolant. After about 3 seconds, cooled coolant enters the reactor core, and the highest coolant temperature in the reactor starts to decrease.

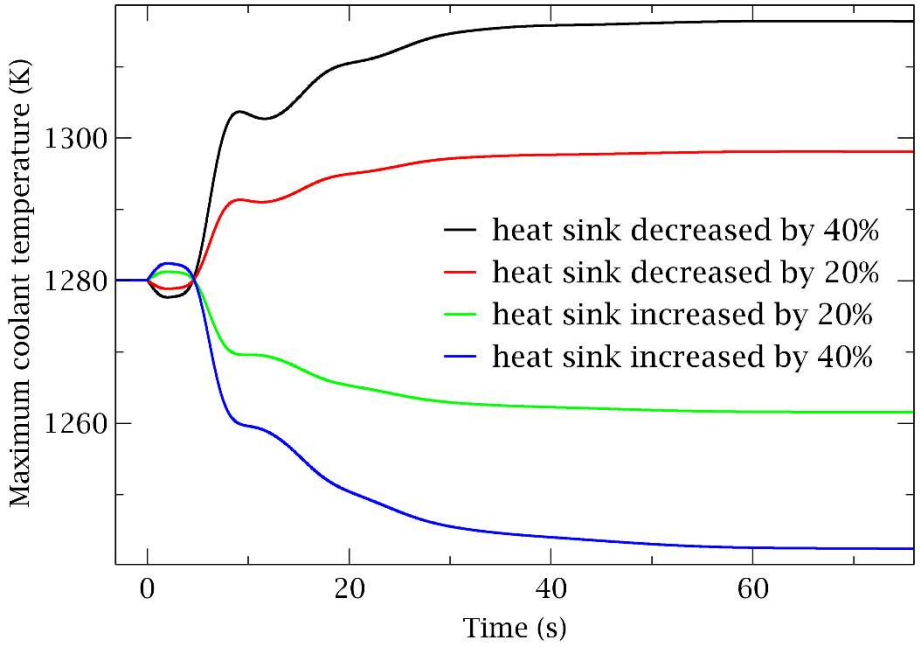

Fig. 79 DFR maximum coolant temperature variation after a step change heat sink efficiency

Fig. 80 presents the minimum coolant temperature change after a step change in the heat sink efficiency. The plot looks very similar to the changes in the maximum coolant temperature shown in Fig. 79. The difference is in the first few seconds. For the lowest coolant temperature, counter-intuitive behaviour did not occur. That is because the lowest coolant temperature in the reactor core is just after entering the inlet region. Thus, it is a coolant which did not interact with the fuel, in contrast to the highest coolant temperature.

It can also be seen that the temperature drop for the lowest coolant temperature is much stronger than for the highest coolant temperature. For the lowest temperature case, it is about 200K, while for the highest temperature case, it is about 40 K.

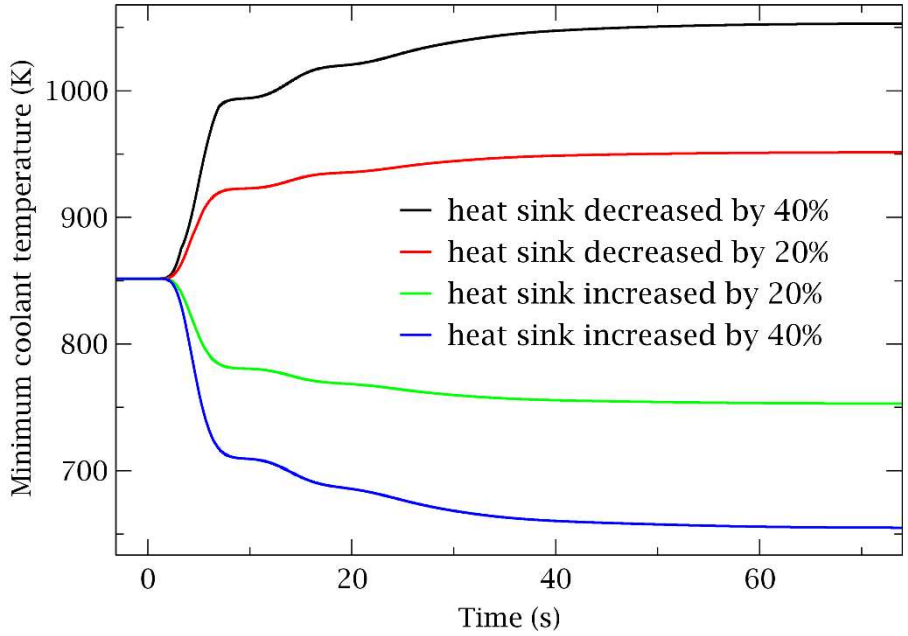

Fig. 80 DFR minimum coolant temperature variation after a step change heat sink efficiency

Summary and Conclusions

MSRE calculations

To validate Serpent and TRACE codes as tools for modelling circulating fuel reactors, the author decided to model MSRE. Obtained results are as follows: criticality calculations, radial and axial power distribution, burnup calculations combined with fuel reprocessing, axial temperature distribution, and transient scenarios with U-233 and U-235. The results of mentioned calculations are in satisfactory agreement with the ORNL models. Therefore, it confirms that used codes can be used for modelling such kinds of nuclear reactors.

Neutronic calculations for the DFR

Based on burnup and branch calculations, temperature reactivity coefficients have been calculated. The total temperature reactivity coefficient is about -4 pcm/K. However, it is too weak to be sufficient to use temperature to control the reactivity during reactor operation. Therefore, geometry modification and initial fuel composition have been proposed. It significantly improves the multiplication factor and makes it flatten during reactor operation. However, even with this improvement, using temperature to control reactivity during the reactor lifetime seems challenging.

Therefore, control rod assemblies in the reflector zone have been proposed. It suppresses reactivity excess during the operation. Thus, it can also be used as a shutdown reactor system. Provided changes (geometry modification and fuel composition) caused keff to drop close to 1 after about 15 years. To avoid subcriticality, feeding the reactor has been started at a rate of about 250 grams per week. It allows maintaining the k-eff slightly above one till the end of the lifetime (about 20 years).

Coupling TRACE and Serpent

To get steady-state conditions for the reactor, Serpent2 and TRACE code have been coupled to exchange temperature field and power field between each other. TRACE needs a power profile to determine temperature, while Serpent2 needs a temperature field to determine the power field. After several iterations, changes between the current iteration and the previous were small enough to assume convergence of the results.

DFR optimisation

In the next step, fuel and coolant loop dimensions have been proposed. Moreover, several criteria related mainly to safety issues have been presented. Based on them, optimal working conditions have been founded for the DFR. Based on mentioned criteria, it has been decided that optimal conditions for the proposed geometry are as follows: fuel flow rate 2500 kg/s, coolant flow rate 5000 kg/s.

For such a prepared system, several transient scenarios have been established. The following transients have been calculated: reactivity step insertion, reactivity ramp insertion and step change in heat sink efficiency.

Reactivity insertion scenarios

In the case of reactivity insertion, the system was able to return to the initial power level after about 50-60 seconds. Because of inserted reactivity and negative reactivity coefficient, fuel temperature has been changed. In case of negative insertion, temperature drops. In the case of positive insertion, the temperature rises. From a safety point of view, the most important parameters are the working fluids' lowest and highest temperature points during such events. High-temperature peaks can be an issue for SiC temperature limits. On the other hand, low-temperature values can be an issue from the point of view of fuel or coolant solidification point.

It can be seen that transients performed at EOL are more severe than corresponding transients at BOL. It is due to a lower fraction of delayed neutrons at the end of reactor operation.

From the point of view of temperature peak, the most severe case is ramp reactivity insertion with a rate of 10 pcm/s for 20 seconds. After about 20 seconds from the beginning of the ramp, the maximum temperature reached about 1600 K. Limits for SiC is about 1923 K.

The most severe case, from the point of view of the temperature lowest point, is ramp reactivity insertion with a rate of -10 pcm/s during 20 seconds. After about 20 seconds from the beginning of the ramp, the minimum temperature reached about 1170 K. Limits for fuel is about 1133 K - eutectic point for the uranium-chromium system. Considering that obtained value 1170 K is the average temperature in the cell with coarse mesh, the lowest local temperature can be noticeably lower. Thus, it can be close to the fuel temperature limit - 1133 K. Therefore, to avoid it, in case of strong negative reactivity insertion, like presented above, some reaction has to be done. It can be: control rod assemblies' movement to the higher position, fuel velocity increase, or coolant velocity increase.

Another idea is to elevate the nominal working temperature further from the lower temperature limit.

A step change in heat sink efficiency scenarios

In case of heat sink changes, the reactor could follow the load. As a result, the reactor changed the power level to a value corresponding to the new heat sink power after about 70 seconds for each presented case.

Maximum fuel temperature was obtained for the heat sink efficiency increased by 40%. However, it was about 1550 K - far from the temperature limit.

Also, the minimum fuel temperature obtained for the heat sink efficiency increased by 40%. It was about 1175 K - similar to the most severe case from the reactivity insertion cases.

The maximum coolant temperature, due to heat sink efficiency change for the most severe scenario, is about 1310 K - far from the limitation.

The minimum coolant temperature, due to heat sink efficiency change for the most severe scenario, is about 655 K. Lead melting point is about 600 K. Therefore, even in case of increasing the output power from the system by 40%, the lowest coolant temperature seems to be far enough from the limitation. However, as in the case of fuel, the given temperature is the average temperature in the cell with coarse mesh. Therefore, the local temperature can be noticeably lower.

Assessment and remarks

The reactor established very good performance from the point of view of stability during different transient scenarios. It also showed a fast response for the heat sink change and could be used as a load-following reactor.

Due to many positive features like a strong negative temperature coefficient, online reprocessing capability, high conductive coolant, and much lower pressure in the fuel and coolant loops, it seems to be a promising technology.

However, it also has many challenging areas; several examples are presented:

- Structural material for fuel pipes in high temperature and high neutron fluence
- Structural materials for the reactor vessel and the rest of the fuel loop in high temperature

- Lack of thermophysical properties regarding uranium-chromium eutectic
- Evaluation of fuel thermophysical properties changes during the reactor operation
- Influence of the fission gases on the stability of the reactor during normal operation and transients
- High-temperature pumps for liquid metals

For most of those challenges, experiments have to be established. Nevertheless, the development of the Dual Fluid Reactor should proceed further.

References

[1] U.S. Energy Information Administration, "https://www.eia.gov/international/data/world," Jul. 12, 2022.

[2] United Nations Development Programme, "https://hdr.undp.org/data-center/documentation-and-downloads," Jul. 12, 2022.

[3] B. K. Sovacool *et al.*, "Balancing safety with sustainability: assessing the risk of accidents for modern low-carbon energy systems," *J Clean Prod*, vol. 112, pp. 3952–3965, 2016, doi: https://doi.org/10.1016/j.jclepro.2015.07.059.

[4] A. Markandya and P. Wilkinson, "Electricity generation and health," *The Lancet*, vol. 370, no. 9591, pp. 979–990, 2007, doi: https://doi.org/10.1016/S0140-6736(07)61253-7.

[5] S. Schloemer *et al.*, "Annex III: Technology-specific cost and performance parameters," in *Climate Change 2014: Mitigation of Climate Change*, O. Edenhofer, R. PichsMadruga, Y. Sokona, J. C. Minx, E. Farahani, S. Kadner, K. Seyboth, A. Adler, I. Baum, S. Brunner, P. Eickemeier, B. Kriemann, J. Savolainen, S. Schlomer, C. VonStechow, T. Zwickel, and J. C. Minx, Eds. United Kingdom: Cambridge University Press, 2014, pp. 1329–1356.

[6] T. Abram and S. Ion, "Generation-IV nuclear power: A review of the state of the science," *Energy Policy*, vol. 36, no. 12, pp. 4323–4330, 2008, doi: https://doi.org/10.1016/j.enpol.2008.09.059.

[7] INTERNATIONAL ATOMIC ENERGY AGENCY, "Status of Molten Salt Reactor Technology", p. 1. Vienna, 2021.

[8] W. B. Cottrell, H. E. Hungerford, J. K. Leslie, and J. L. Meem, "OPERATION OF THE AIRCRAFT REACTOR EXPERIMENT," Office of Scientific and Technical Information (OSTI), Sep. 1955. doi: 10.2172/4237975.

[9] Ferguson W and McQuilkin F, "TERMINATION REPORT FOR CONSTRUCTION OF THE ART FACILITY," Oak Ridge, Nov. 1958.

[10] Murray W. Rosenthal, "An Account of Oak Ridge National Laboratory's Thirteen Nuclear Reactors", pp. 27; 29, 2009.

[11] R. C. Robertson, "MSRE design and operations report. Part I. Description of reactor design," 1965.

[12] J. H. Shaffer, "PREPARATION AND HANDLING OF SALT MIXTURES FOR THE MOLTEN SALT REACTOR EXPERIMENT", p. 4, 1971.

[13] R. H. Guymon, "MSRE Systems and Component Performance", pp. 13;19, 1973.

[14] H. E. McCoy and B. McNabb, "Postirradiation Examination of Materials from the MSRE", p. 7, 1972.

[15] Rosenthal M. W., “DEVELOPMENT STATUS OF MOLTEN-SALT BREEDER REACTORS”, pp. 34; 56, Office of Scientific and Technical Information (OSTI), Jan. 1972. doi: 10.2172/4622532.

[16] L. E. McNeese, “Molten-salt reactor program. Semiannual progress report for period ending February 29, 1976,” Oak Ridge, Aug. 1976.

[17] W. E. S. J. SMITH, “AN ASSESSMENT OF A 2500 MWe MOLTEN CHLORIDE SALT FAST REACTOR,” Winfrith, 1974.

[18] D. LeBlanc and C. Rodenburg, “Integral molten salt reactor,” in *Molten Salt Reactors and Thorium Energy*, Elsevier, 2017, pp. 541–556. doi: 10.1016/b978-0-08-101126-3.00018-x.

[19] M. Brovchenko *et al.*, “Neutronic benchmark of the molten salt fast reactor in the frame of the EVOL and MARS collaborative projects,” *EPJ Nuclear Sciences & Technologies*, vol. 5, p. 2, 2019, doi: 10.1051/epjn/2018052.

[20] T. Schønfeldt and E. Klinkby, “Molten salt thermal wasteburner,” in *Molten Salt Reactors and Thorium Energy*, Elsevier, 2017, pp. 609–618. doi: 10.1016/B978-0-08-101126-3.00024-5.

[21] D. Wilson and T. Intl, “Two 500 MW ThorCon liquid fission power plants ThorCon Molten Salt Reactor (TMSR-500) Technology for Indonesia,” 2019. Accessed: Aug. 21, 2022. [Online]. Available: https://thorconpower.com/slides/TEAC10%20dfw%2020190930.pdf

[22] S. Delpech, V. Ghetta, D. Heuer, D. Holcomb, and J. Serp, “The molten salt reactor (MSR) in Genration IV: overview ans perspectives THE MOLTEN SALT REACTOR (MSR) IN GENERATION IV: OVERVIEW AND PERSPECTIVES,” 2012. [Online]. Available: https://www.researchgate.net/publication/281915971

[23] B. R. Betzler, J. J. Powers, A. Worrall, S. Robertson, L. Dewan, and M. Massie, “Two-Dimensional Neutronic and Fuel Cycle Analysis of the Transatomic Power Molten Salt Reactor,” Oak Ridge, TN (United States), Jan. 2017. doi: 10.2172/1340461.

[24] A. Huke *et al.*, “Dual-fluid reactor,” *Molten Salt Reactors and Thorium Energy*. pp. 619–633, 2017.

[25] A. Huke, G. Ruprecht, D. Weißbach, S. Gottlieb, A. Hussein, and K. Czerski, “The Dual Fluid Reactor – A novel concept for a fast nuclear reactor of high efficiency,” *Ann Nucl Energy*, vol. 80, pp. 225–235, 2015, doi: https://doi.org/10.1016/j.anucene.2015.02.016.

[26] M. Nowak, M. Spirzewski, and K. Czerski, “Optimization of the DC magnetohydrodynamic pump for the Dual Fluid Reactor,” *Ann. Nucl. Energy*, vol. 174, p. 109142, Sep. 2022.

[27] X. Wang and R. Macian-Juan, "Steady-state reactor physics of the dual fluid reactor concept," *Int. J. Energy Res.*, vol. 42, no. 14, pp. 4313–4334, Nov. 2018.

[28] C. Liu, X. Li, R. Luo, and R. Macian-Juan, "Thermal Hydraulics Analysis of the Distribution Zone in Small Modular Dual Fluid Reactor," *Metals (Basel)*, 2020.

[29] J. Sierchuła, "PhD Thesis: Determination of the liquid eutectic metal fuel Dual Fluid Reactor design," Jul. 2021.

[30] X. Wang and R. Macian-Juan, "Comparative Study of Thermal-Hydraulic Behavior of the DFR Using U-Pu and TRU Salt Fuels," in *2017 25th International Conference on Nuclear Engineering*, Oct. 2017.

[31] X. He, "Validation of the TRACE code for the system dynamic simulations of the Molten Salt Reactor Experiment and the preliminary study on the Dual Fluid molten salt reactor," Technische Universität München, 2016.

[32] X. Wang *et al.*, "NEUTRON PHYSICAL FEASIBILITY OF SMALL MODULAR DESIGN OF DUAL FLUID REACTOR," *The Proceedings of the International Conference on Nuclear Engineering (ICONE)*, vol. 2019.27, p. 1229, 2019.

[33] D. Weiβbach, J. Sierchuła, M. P. D abrowski, K. Czerski, and G. Ruprecht, "Dual Fluid Reactor as a long-term burner of actinides in spent nuclear fuel," *International Journal of Energy Research*, vol. 45, no. 8. pp. 11589–11597, 2021.

[34] J. Leppänen and A. Isotalo, "Burnup calculation methodology in the Serpent 2 Monte Carlo code," 2012.

[35] D. Shen, M. Fratoni, M. Aufiero, A. Bidaud, J. Powers, and G. Ilas, "Zero-power criticality benchmark evaluation of the molten salt reactor experiment," in *Proceedings of the International Conference on Physics of Reactors. PHYSOR*, 2018.

[36] P. N. Haubenreich and J. R. Engel, "Experience with the Molten-Salt Reactor Experiment," *Nuclear Applications and Technology*, vol. 8, no. 2, pp. 118–136, 1970, doi: 10.13182/NT8-2-118.

[37] B. E. Prince, S. J. Ball, J. R. Engel, P. N. Haubenreich, and T. W. Kerlin, "ZERO-POWER PHYSICS EXPERIMENTS ON THE MOLTEN-SALT REACTOR EXPERIMENT.," Office of Scientific and Technical Information (OSTI), Jan. 1968. doi: 10.2172/4558029.

[38] P. N. Haubenreich, "Tritium in the MSRE: Calculated Production Rates and Observed Amounts," Office of Scientific and Technical Information (OSTI), Feb. 1970. doi: 10.2172/1411211.

[39] R. B. Briggs, "Molten-salt reactor program semiannual progress report," *Oak Ridge National Laboratory Technical Report*, 1964.

[40] R. B. Gallaher, “Contract no. W-7405-eng-26 reactor division OPERATION OF THE SAMPLER-ENRICHER in the MOLTEN SALT REACTOR EXPERIflENT.” 1971.

[41] R. E. Thoma, “CHEMICAL ASPECTS OF MSRE OPERATIONS.,” Office of Scientific and Technical Information (OSTI), Jan. 1971. doi: 10.2172/4675946.

[42] R. J. Kedl and A. Houtzeel, “DEVELOPMENT OF A MODEL FOR COMPUTING sup 135Xe MIGRATION IN THE MSRE.,” Office of Scientific and Technical Information (OSTI), Jan. 1967. doi: 10.2172/4363507.

[43] G. M. Tolson and A. Taboada, “MSRE CONTROL ELEMENTS: MANUFACTURE, INSPECTION, DRAWINGS, AND SPECIFICATIONS,” osti.gov, 1967.

[44] Nrc, “TRACE V5. 0 Theory Manual, Field Equations, Solution Methods, and Physical Models,” *United States Nucl. Regul. Comm.*

[45] Nuclear Regulatory Commission, “Symbolic Nuclear Analysis Package (SNAP) User’s Manual,” 2012.

[46] S. Cantor, “PHYSICAL PROPERTIES OF MOLTEN-SALT REACTOR FUEL, COOLANT, AND FLUSH SALTS,” 1968.

[47] Ash Milton, *Nuclear Reactor Kinetics*, II. New York: McGraw-Hill, 1979.

[48] T. Hanusek and R. M. Juan, “Analysis of the Power and Temperature distribution in molten salt reactors with TRACE. Application to the MSRE,” *Ann. Nucl. Energy*, 2021.

[49] R. C. Steffy Jr and P. J. Wood, “Theoretical dynamic analysis of the MSRE with 233U fuel,” *Oak Ridge National Laboratory Technical Report*, 1969.

[50] S. J. Ball and T. W. Kerlin, “Stability Analysis of the Molten-Salt Reactor Experiment,” 1965.

[51] J. R. Engel and P. N. Haubenreich, “Temperatures in the MSRE core during steady-state power operation,” 1962.

[52] P. N. Haubenreich, J. R. Engel, B. E. Prince, and H. C. Claiborne, “MSRE DESIGN AND OPERATIONS REPORT. PART III. NUCLEAR ANALYSIS,” Office of Scientific and Technical Information (OSTI), Feb. 1964. doi: 10.2172/4114686.

[53] W. M. Stacey, *Nuclear Reactor Physics.*, pp. 47; 144; 213, John Wiley & Sons, 2007.

[54] B. Spinelli, “Preliminary analysis of the MSRE dynamic behaviour,” 2010.

[55] J. Sierchuła, M. P. Da ̨browski, and K. Czerski, “Negative temperature coefficients of reactivity for metallic fuel Dual Fluid Reactor,” *Progress in Nuclear Energy*, vol. 146. p. 104126, 2022.

[56] J. Sierchuła, D. Weissbach, A. Huke, G. Ruprecht, K. Czerski, and M. P. Da˛browski, "Determination of the liquid eutectic metal fuel dual fluid reactor (DFRm) design – steady state calculations," *International Journal of Energy Research*, vol. 43, no. 8. pp. 3692–3701, 2019.

[57] T. Hanusek and R. Macian-Juan, "Analyses of the shutdown system and transients scenarios for the dual fluid reactor concept with metallic molten fuel," *Int J Energy Res*, vol. 46, no. 12, pp. 17230–17246, Oct. 2022, doi: 10.1002/er.8387.

[58] K. Thurnay, "Thermal properties of transition metals," 1998.

[59] INTERNATIONAL ATOMIC ENERGY AGENCY, *Thermophysical Properties of Materials For Nuclear Engineering: A Tutorial and Collection of Data*. 2008.

[60] O. Nilsson *et al.*, "Determination of the thermal diffusivity and conductivity of monocrystalline silicon carbide (300-2300 K)," *High Temperatures-High Pressures*, vol. 29, no. 1. pp. 73–79, 1997.

[61] OECD Nuclear Energy Agency, Organisation for Economic Co-operation, and Development, *Handbook on Lead-bismuth Eutectic Alloy and Lead Properties: Materials Compatibility, Thermalhydraulics and Technologies*. OECD Publishing, 2015.

[62] X. Wang, M. Seidl, R. Macian-Juan, and R. Macián-Juan, "Preliminary Analysis of Basic Reactor Physics of the Dual Fluid Reactor Concept," 2015. [Online]. Available: http://festkoerper-kernphysik.de

[63] M. Venkatraman, J. P. Neumann, and D. E. Peterson, "The Cr-U (Chromium-Uranium) system," *Bulletin of Alloy Phase Diagrams*, vol. 6, no. 5, pp. 425–429, Oct. 1985.

[64] Colin, Falanga, Maxel, and Monnet, "Behaviors of SiC fibers up to high temperature," in *14th International Conference on Fusion Reactor Materials (ICFRM-14)*.

[65] J. G. Eberhart, "The Surface Tension of Binary Liquid Mixtures1," *J. Phys. Chem.*, vol. 70, no. 4, pp. 1183–1186, Apr. 1966.

[66] G. Latini, "Thermophysical properties of fluids: dynamic viscosity and thermal conductivity," *J. Phys. Conf. Ser.*, 2017.

[67] H. Kopp and T. Graham, "III. Investigations of the specific heat of solid bodies," *Philos Trans R Soc Lond*, vol. 155, pp. 71–202, Jan. 1865.

[68] L. Grunberg and A. H. Nissan, "Mixture Law for Viscosity," *Nature*, vol. 164, no. 4175, pp. 799–800, Nov. 1949.

[69] 孝道飯田, "液体金属の物性(IV)," 溶接学会誌, vol. 63, no. 3, pp. 140–145, 1994.

[70] J. J. M. Mckee, McKee, Jr, and J. M., “THERMAL CONDUCTIVITY OF URANIUM-CHROMIUM AND URANIUM-IRON EUTECTIC ALLOYS.” 1953.

[71] D. Ofte, “The viscosities of liquid uranium, gold and lead,” *J. Nucl. Mater.*, vol. 22, no. 1, pp. 28–32, Apr. 1967.